

ISSN 2587-1943

#15

VOLUME 8, 1  
JUNE 2024

**Editor-in-Chief**  
Niyazi Özdemir  
Hikmet Esen

**Deputy Editor-in-Chief**  
Abdullah Kapıcıoğlu

**Managing Editor**  
Cihangir Kale

A

E

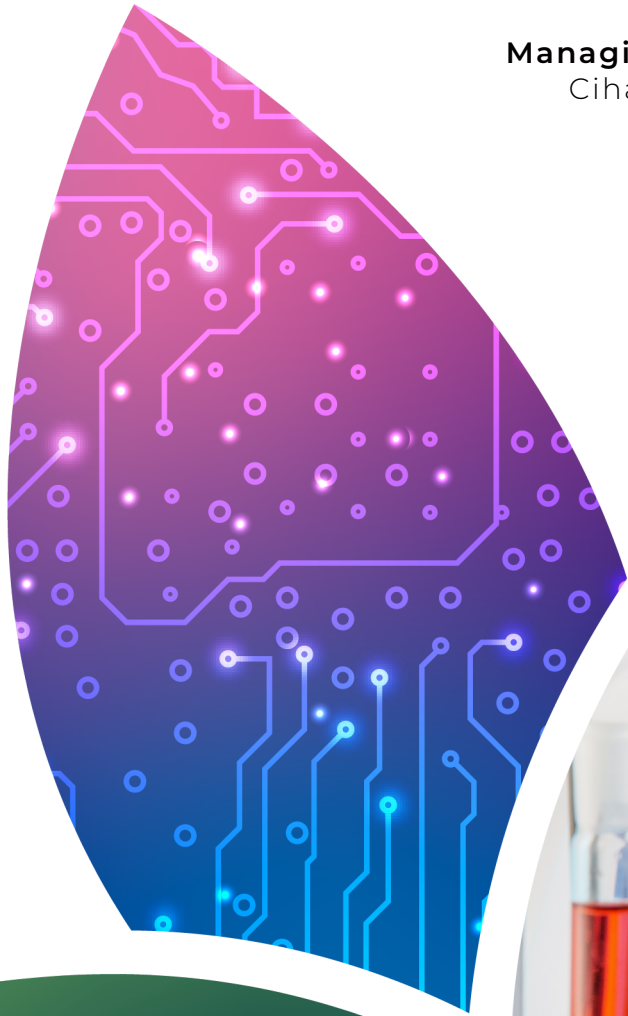
I

J

R

JOURNAL

INTERNATIONAL JOURNAL OF INNOVATIVE ENGINEERING APPLICATIONS



### **Editor-in-Chief**

Prof. Dr. Niyazi ÖZDEMİR

Prof. Dr. Hikmet ESEN

### **Deputy Editor-in-Chief**

Asst. Prof. Dr. Abdullah KAPICIOĞLU

### **Executive Editors**

Prof. Dr. Messaoud SAIDANI

Prof. Dr. Niyazi BULUT

Prof. Dr. Kemal LEBLEBİCİOĞLU

Asst. Prof. Dr. Salwa BOUADILA

### **Managing Editor**

Dr. Cihangir KALE

---

### **Subject Editors**

Prof. Dr. Arif HEPBAŞLI

Prof. Dr. Asaf VAROL

Prof. Dr. Asım BALBAY

Prof. Dr. Elhoussine AZROUL

Prof. Dr. Engin AVCI

Prof. Dr. Fatih POYRAZ

Prof. Dr. Fethi DAĞDELEN

Prof. Dr. Hacı Mehmet BAŞKONUŞ

Prof. Dr. Hasan TOĞRUL

Prof. Dr. İbrahim CAN

Prof. Dr. İnanç ÖZGEN

Prof. Dr. Mehmet EROĞLU

Prof. Dr. Murat KÖKSAL

Prof. Dr. Ömer YILDIRIM

Prof. Dr. Özen ÖZER

Prof. Dr. Resul ÇÖTELİ

Prof. Dr. Şükrü TALAŞ

Prof. Dr. Tahir KHAN

Assoc. Prof. Dr. Alper POLAT

Assoc. Prof. Dr. Erkan BAHÇE

Assoc. Prof. Dr. Faruk KARACA

Assoc. Prof. Dr. Filiz ÖZGEN

Assoc. Prof. Dr. Reza BAKHTIARI

Assoc. Prof. Dr. Serdar MERCAN

Asst. Prof. Dr. Fehmi ASLAN

Asst. Prof. Dr. Nagihan KARAASLAN AYHAN

Asst. Prof. Dr. Üyesi Ferit AK

Asst. Prof. Dr. Vembu ANANTHASWAMY

### **Layout / Language Editor**

M.Sc. Buğra ŞEN

Asst. Prof. Dr. Habip ŞAHİN

---

International Journal of Innovative Engineering Applications is published June and December.

Adress for the manuscripts and correspondence:

International Journal of Innovative Engineering Applications  
Firat Üniversitesi Kampüsü, Teknoloji Fakültesi, Merkez–Elazığ

Tel: +90 424 237 0000/ Ext.7655

e-mail: ijieatr@gmail.com

ISSN: 2587-1943

Elazığ-2024

#15

IJIEA

# IJIEA

## volume 8 issue 1

### CONTENTS / İÇİNDEKİLER

Title / Başlık Author(s) / Yazar(lar)	Page(s) / Sayfa(lar)
<p>PVA/WHEY PROTEIN NANOFIBER-COATED PP MELT BLOWN INTEGRATED WITH PICKERING EMULSION OF CITRAL STABILIZED FOR POTENTIAL MEDICAL APPLICATIONS</p> <p>POTANSİYEL MEDİKAL UYGULAMALAR İÇİN PVA/WHEY PROTEİN NANOLİF KAPLI PP ERİYİK ÜFLEMELİ DOKUSUZ YÜZEYLERE ENTEGRE EDİLMİŞ SİTRAL STABİLİZE PICKERING EMÜLSİYONLAR</p> <p><i>Fatma Nur Parın, Ayşenur Yeşilyurt, Uğur Parın</i></p> <p><i>Research Article [en] Araştırma Makalesi [tr]</i></p>	1-7
<p>REDUCING ROCKFALL HAZARDS IN SABİHA GOKÇEN – TAVSANTEPE METRO PROJECT CONSTRUCTION BY USING ROOT CAUSE ANALYSIS METHODOLOGY</p> <p>SABİHA GÖKÇEN – TAVŞANTEPE METRO PROJESİ İNŞAATINDA KÖK NEDEN ANALİZİ METODOLOJİSİ KULLANILARAK KAYA DÜŞMESİ TEHLİKESİNİN AZALTILMASI</p> <p><i>Okan Özbakır</i></p> <p><i>Research Article [en] Araştırma Makalesi [tr]</i></p>	8-16
<p>ELEMENTAL ANALYSIS AND DETERMINATION OF TOTAL PHENOLIC AND FLAVONOID CONTENT OF RHEUM RIBES L. BARK</p> <p><i>İdris Yolbaş</i></p> <p><i>Research Article [en] Araştırma Makalesi [tr]</i></p>	17-21
<p>EXAMINING ARCHITECTURAL PROJECT APPLICATIONS WITH PHOTOGRAMMETRIC POINT CLOUD: İĞDIR UNIVERSITY MOSQUE</p> <p>MİMARİ PROJE UYGULAMALARININ FOTOGRAMETRİK NOKTA BULUTU İLE İNCELENMESİ: İĞDIR ÜNİVERSİTESİ CAMİİ ÖRNEĞİ</p> <p><i>Selim Kartal, Emirhan Özdemir, Rüştü Çallı</i></p> <p><i>Research Article [en] Araştırma Makalesi [tr]</i></p>	22-27
<p>INVESTIGATION OF THE EFFECTS OF SMAW PARAMETERS AND SEAWATER TEMPERATURE ON PROPERTIES OF AH36 JOINTS AND THE CHEMICAL COMPOSITION OF SEAWATER</p> <p>SMAW PARAMETRELERİNİN AH36 BAĞLANTI ÖZELLİKLERİNE VE DENİZ SUYUNUN KİMYASAL BİLEŞİMİNE ETKİSİNİN ARAŞTIRILMASI</p> <p><i>Emre Görgün</i></p> <p><i>Research Article [en] Araştırma Makalesi [tr]</i></p>	28-36

# IJIEA

## volume 8 issue 1

### CONTENTS / İÇİNDEKİLER

Title / Başlık Author(s) / Yazar(lar)	Page(s) / Sayfa(lar)
<b>OUTPUT POWER ESTIMATION OF A PHOTOVOLTAIC PANEL BY EXTREME LEARNING MACHINE</b> <i>ÇIKIŞ GÜCÜ UÇ ÖĞRENME ALGORİTMASI İLE BİR FOTOVOLTAİK PANELİN ÇIKIŞ GÜCÜ TAHMİNİ</i> <b>Serhat Toprak, Resul Çötel, Mehmet Üstündağ, Hikmet Esen</b> <i>Research Article [en] Araştırma Makalesi [tr]</i>	37-42
<b>NUMERICAL SOLUTIONS TO THE STOCHASTIC SYSTEMS WITH FRACTIONAL OPERATORS</b> <i>KESİRLİ MERTEBELİ DİFERANSİYEL DENKLEMLERİN YENİ SAYISAL ÇÖZÜMLERİ</i> <b>Mehmet Ali Akinlar</b> <i>Research Article [en] Araştırma Makalesi [tr]</i>	43-52
<b>INVESTIGATION OF FLEXURAL BEHAVIOR OF CARBON FIBER BEAMS</b> <b>Mustafa Albayrak</b> <i>Research Article [en] Araştırma Makalesi [tr]</i>	53-57
<b>MOBILE MICRORNAS (MIRNAS) RESPONSIVE TO EXCESS NICKEL IN PUMPKIN (CUCURBITA MAXIMA L.)</b> <i>BALKABAĞINDA (CUCURBITA MAXIMA L.) FAZLA NİKELE YANIT VEREN MOBİL MİKRORNA'LAR (MIRNA'LAR)</i> <b>Guzin Tombuloglu</b> <i>Research Article [en] Araştırma Makalesi [tr]</i>	58-64



## PVA/WHEY PROTEIN NANOFIBER-COATED PP MELT BLOWN INTEGRATED WITH PICKERING EMULSION OF CITRAL STABILIZED FOR POTENTIAL MEDICAL APPLICATIONS

Fatma Nur Parın<sup>\*1</sup> , Ayşenur Yeşilyurt<sup>1</sup> , Uğur Parın<sup>2</sup> 

<sup>1</sup>Department of Polymer Materials Engineering, Faculty of Engineering and Natural Sciences, Bursa Technical University, Bursa, Turkey

<sup>2</sup>Department of Chemical Engineering, Faculty of Engineering and Natural Sciences, Bursa Technical University, Bursa, Turkey

<sup>3</sup>Department of Microbiology, Faculty of Veterinary Medicine, Aydın Adnan Menderes University, Aydın, Turkey

### Abstract

Original scientific paper

As an antibacterial agent with pleasant fragrance, citral (CIT) indicates hydrophobic character, and therefore has low water solubility. In this study, Pickering emulsions were formed and polyvinyl alcohol (PVA)/whey protein hydrophilic nanofibers were coated on PP melt blown non-woven surfaces by electrospinning method. In this context, hydrophobic citral essential oil is stabilized with  $\beta$ -cyclodextrin ( $\beta$ -CD) in the electrospinning process. PVA and whey protein polymer blend were used as nanofiber matrices. The morphological, physical, and thermal properties of the  $\beta$ -CD/citral complexes were investigated in PVA/whey protein nanofiber-coated PP non-wovens at various  $\beta$ -CD levels (1:2, 1:4 and 1:6). Furthermore, zone inhibition procedure was performed to evaluate antibacterial activity of the samples against Gram (+) (*Staphylococcus aureus* ATCC® 25923) and Gram (-) (*Escherichia coli* ATCC® 25922, and *Pseudomonas aeruginosa* ATCC® 27853) bacteria. The morphology of fibers showed that all obtained nanofiber-coated PP surfaces were in the range with 216 - 330 nm average fiber diameter. Fourier Transform Infrared (FT-IR) and thermal gravimetric analysis (TGA) thermograms revealed that citrals were successfully integrated into the bio-based nanofibers. As the amount of citral increased (i.e., the  $\beta$ -CD/citral increased), the thermal resistance of bio-based nanofiber coated PP surfaces increased. Antibacterial activity indicated the citral-loaded nanofiber-coated PP surfaces were most effective against *Escherichia coli*, while none of the samples have antibacterial activity against *Pseudomonas aeruginosa*. Overall, the results displayed that the fabricated PVA/whey protein nanofiber-coated PP samples integrated with Pickering emulsion of citral stabilized have promising wound dressing applications.

**Keywords:** Antibacterial property, Pickering emulsion, PP melt blown, PVA/whey protein nanofiber,  $\beta$ -CD/citral comple.

## POTANSİYEL MEDİKAL UYGULAMALAR İÇİN PVA/WHEY PROTEİN NANOLİF KAPLI PP ERİYİK ÜFLEMELİ DOKUSUZ YÜZEYLERE ENTEGRE EDİLMİŞ SİTRAL STABİLİZE PICKERING EMÜLSİYONLAR

### Özet

Orijinal bilimsel makale

Hoş kokulu bir antibakteriyel madde olarak sitral (SIT) hidrofobik karakter sergiler ve bu sebeple suda çözünürlüğü düşüktür. Bu çalışmada Pickering emülsiyonları oluşturulmuş ve elektroçekim yöntemi ile polipropilen (PP) eriyik üflemeli dokusuz yüzeylere polivinil alkol (PVA)/whey proteini hidrofilik nanofiberler kaplanmıştır. Bu bağlamda, elektroçekim yönteminde hidrofobik sitral uçucu yağı  $\beta$ -siklodekstrin ( $\beta$ -CD) ile stabilize edilmiştir. Nanofiber matris olarak PVA ve whey proteini polimer karışımı kullanılmıştır.  $\beta$ -CD/sitral komplekslerinin morfolojik, fiziksel ve termal özellikleri PVA/whey proteini nanofiber kaplı PP dokusuz dokumalarda çeşitli  $\beta$ -CD seviyelerinde (1: 2, 1: 4 ve 1:6) araştırılmıştır. Ayrıca, numunelerin Gram (+) (*Staphylococcus aureus* ATCC ® 25923) ve Gram (-) (*Escherichia coli* ATCC ® 25922 ve *Pseudomonas aeruginosa* ATCC ® 27853) bakterilerine karşı antibakteriyel aktivitesini değerlendirmek için zon inhibisyon prosedürü uygulanmıştır. Liflerin morfolojisi, elde edilen tüm nanofiber kaplı PP yüzeylerin 216 - 330 nm ortalama lif çapı aralığında olduğunu göstermiştir. Fourier Dönüşümü Kızılötesi (FT-IR) spektroskopisi ve termal gravimetrik analiz (TGA) termogramları, sitralin biyo bazlı nanofiberlere başarıyla entegre edildiğini ortaya koymuştur. Sitral miktarı arttıkça (yani  $\beta$ -CD/sitral arttıkça), biyobazlı nanofiber kaplı PP yüzeylerin ısı direnci artmıştır. Antibakteriyel aktivite, sitral yüklü nanofiber kaplı PP yüzeylerinin *Escherichia coli* bakterisine karşı en etkili olduğunu gösterirken, örneklerin hiçbirinin *Pseudomonas aeruginosa* bakterisine karşı antibakteriyel aktivitesi olmadığını göstermiştir. Genel olarak, sonuçlar, sitral stabilize Pickering emülsiyonu ile entegre edilmiş PVA/whey proteini nanofiber kaplı PP örneklerinin umut verici yara pansuman uygulamalarına sahip olduğunu göstermiştir.

**Anahtar Kelimeler:** Antibakteriyel özellik, Pickering emülsiyon, PP melt blown, PVA/whey protein nanolif,  $\beta$ -CD/sitral kompleks.

\*Corresponding author.

E-mail address: nur.parin@btu.edu.tr (F. N. Parın)

Received 21 November 2022; Received in revised form 16 November 2023; Accepted 26 April 2024

2587-1943 | © 2024 IJIEA. All rights reserved.

Doi: <https://doi.org/10.46460/ijiea.1206901>

## 1 Introduction

Essential oils (EOs) have been the focus of considerable investigation as natural products, and they play a crucial role in food and human health [1]. Due to their bioactivity to prevent the development of microorganisms such as bacteria, yeasts, and fungus, the components of essential oils are a promising substitute to chemical preservatives. Citral (3,7-dimethyl-2,6-octadienal) is a combination of two monoterpene aldehydes found naturally in plants, herbs, and citrus fruits: geranial (trans-citral, citral A) and neral (cis-citral, citral B) [2-4]. It has been reported to have anti-inflammatory and anti-corrosive characteristics in a variety of experimental and clinical studies, and there is substantial proof that it functions as a fungicidal and bactericidal agent [5,6]. However, one of the key challenges in the application of citral essential oils and their principal components is the requirement for greater amounts than those utilized in vitro. One alternative option is to combine oils and/or components to reduce the amount required [7]. Other factors restricting the use of citral in many applications are its low water solubility and sensitivity to environmental influences such as thermal and oxidation. In this regard, it has been found that making emulsions of citral oil increases the availability and shelf life of different forms such as nanofibers, microcapsules, films, as well as its antibacterial activity. According to Lu et al. (2018) essential oil nanoemulsions containing citral had a substantial effect on Gram (+) bacteria, the bacteria with the highest zone of inhibition test [3]. Mokarizadeh et al. (2017) have investigated the antimicrobial activity of citral loaded nanocarriers [8]. They assigned activity of citral with good values against many microorganisms. In addition, there are quite a lot of studies in the literature on the production of electrospun fibers after emulsifying essential oils in water-based polymer solutions.

Nanofibers, one of several polymeric forms, are complex fibrous structures with sizes ranging from micrometers to nanometers [9-14]. Because of their high porosity, wide specific surface area, and relatively small size, nanofibers have become a promising choice for medical applications over the last few decades.

Pickering emulsions are a unique approach of stabilizing emulsions, i.e., oil/water mixtures, that utilize solid particles instead of surfactants [15]. In this approach, in this approach, by using inorganic particles such as modified clay, silica, the emulsion is stabilized and a barrier is formed that prevents the formation of cohesiveness. Thus, stable emulsion solutions are obtained.

$\beta$ -cyclodextrin is a kind of carbohydrate and it has hollow conical shape with hydrophilic outer part and hydrophobic inner part which makes it an excellent Pickering emulsifier [16]. Therefore, stable emulsions have better evaporation resistance to essential oils than

surfactant-stabilized systems, giving better antibacterial performance thanks to the  $\beta$ -cyclodextrin.

The current study concerned with fabrication of PVA/whey protein/citral nanofiber-coated PP melt blown surfaces by using 3 various ratio of  $\beta$ -CD/citral complexes (1:2, 1:4 and 1:6) via electrospinning. For this aim, due to the low solubility of citral in water, o/w Pickering emulsion solutions were obtained by adding the antibacterial citral agent to  $\beta$ -CD-stabilized biobased PVA hydrophilic solutions. Afterward, the bio-based o/w polymer solutions were coated on the PP melt blown surfaces by electrospinning. The findings showed that nanofiber solutions up to certain  $\beta$ -CD/citral (1:4) ratio show good fiber morphology, while the nanofiber solution with the highest  $\beta$ -CD/citral (1:6) ratio show the highest antibacterial activity against *Escherichia coli* (*E.coli*). Finally, it is suggested that PVA/whey protein/citral nanofiber-coated PP melt blown surfaces can be good candidates for medical usages especially wound dressing applications.

## 2 Materials and Method

### 2.1 Materials

PP meltblown (MB) non-woven fabrics were kindly donated by Mogul Textile Company (Gaziantep, Turkey) were used. The polyvinyl alcohol (PVA) (purity 87.8%, Mw~30.000 g/mol) was purchased from Zag Industrial Chemical Company (Turkey). Whey protein powders were used which purchased from Naturebyme (İstanbul, Turkey).  $\beta$ -cyclodextrin ( $\beta$ -CD) cyclodextrin ( $\beta$ -CD) (Cavamax W7 HP Pharma) was donated by Wacker Chemie (Germany). Citral (C<sub>10</sub>H<sub>16</sub>O) (technical grade) was kindly donated by Elso Kimya Chemical Company (Turkey). All of the chemicals were used without being purified in the experiments.

### 2.2 Fabrication of Citral-Loaded Hybride Non-Woven Surfaces

PVA powders dissolved in distilled water to obtain a 10% (w/v) PVA solution by stirring at 90 °C. Whey protein powders were also dissolved in water to obtain 20% (w/v) whey protein solutions. Then, these two polymer solutions were mixed to make blend solutions (7/3, v/v).  $\beta$ -cyclodextrin /citral complexes were added to the polymer mixtures as ratio of 1:2, 1:4 and 1:6 (w/v) and then high-speed mixing was performed. The nanofibers were successfully fabricated onto PP meltblown surfaces via electrospinning (Nanospinner24, INOVENSO). The electrospinning process parameters were given in Table 1. The neat PVA/whey protein nanofiber coated-melt blown hybrid surfaces used as a control sample. All samples was kept in the desicator. The samples were named PPWPC1, PPWPC2, and PPWPC3, where C1, C2, and C3, respectively stand for the changing  $\beta$ -CD/citral ratios (1:2, 1:4, and 1:6). The neat sample was named PPWPC0.

**Table 1.** The electrospinning process parameters.

	Voltage (kV)	Distance (mm)	Flow rate (mL/h)	Collector rate (rpm)	$\beta$ - CD/citral (w/v)
PPWPC0	28	89	0.75	250	-
PPWPC1	28	89	0.75	250	1:2
PPWPC2	28	89	0.75	250	1:4
PPWPC3	28	89	0.75	250	1:6

\*\*The temperature and humidity conditions are approximately 26°C and 50 %, respectively.

### 2.3 Characterization

The nanofibers' microstructural properties was evaluated using a Scanning Electron Microscope (SEM). All samples were gold-coated prior to analysis. Image J (version 1.520 software) was performed to measured fiber diameter for each sample.

Thermogravimetric analysis (TGA) was performed in a nitrogen atmosphere (N<sub>2</sub>)<sub>(g)</sub> with a heating rate of 10°C min<sup>-1</sup> over a temperature range of 30 – 600 °C, followed by an oxygen atmosphere (O<sub>2</sub>)<sub>(g)</sub> with the same heating rate.

The chemical structures of the non-woven surfaces were confirmed using Fourier transform infrared (FT-IR) spectroscopy. The data were obtained using a ThermoNicolet iS50 FT-IR (USA) spectrometer with an ATR adaptor (Smart Orbit Diamond, USA) in the wavelength range 4000 - 500 cm<sup>-1</sup>, with 16 scans at 4 cm<sup>-1</sup> resolution.

### 2.4 Antibacterial Activity

The antibacterial sensitivities of hybride non-wovens were determined by the standard strains of *Escherichia coli* ATCC® 25922, *Staphylococcus aureus* ATCC® 25923 and *Pseudomonas aeruginosa* ATCC® 27853. The lyophilized bacterial strains were grown on Trypton Soy Agar (Merck Millipore™ 105458). The culture media were incubated for 24 hours at 37°C under aerobic environment. Bacterial colonies were suspended in saline isotonic solution and adjusted to 0.5 McFarland (1 × 10<sup>8</sup> CFU/mL) turbidity standard.

The disk diffusion technique was used to assess antimicrobial effectiveness qualitatively. Mueller Hinton Agar (Merck Millipore™ 103872) was inoculated with 100  $\mu$ L of bacterial suspensions. The polymer ingredients were placed on the agar plate's surface. The plates were incubated in an aerobic atmosphere for 24 hours. At the end of the incubation time, the zone diameter of the inhibition region around the material injected for each non-woven based-polymer was measured using a calliper.

## 3 Results and Discussion

### 3.1 Morphological Analysis

SEM analysis was carried out to describe the interior morphology of all nanofiber coatings and the resultant micrographs are shown in Figure 1. The neat samples (PVA/whey protein) are continuous, with average fiber diameters of 330.5  $\pm$  87 nm. Moreover, uniform and beaded fiber morphology was seen which coincides with the other PVA/whey protein nanofiber morphology in the literature [17]. Fiber diameter distribution of PWPC1 is more homogeneous than the PVA/whey protein/citral fiber

coatings (PWPC2 and PWPC3). However, increasing the amount of citral damaged the fiber morphology, resulting in the formation of beaded structures. This is due to the decreasing of spinning solution viscosity. The viscosity of the spinning solutions was a significant parameter influencing the fiber diameter. Kim et al. (2016) also showed that the viscosity of the spinning solution may modify the diameter of PVA-based nanofibers, demonstrating that the viscosity of the solution has a relationship between its concentration and nanofiber diameter [18]. A study on characterization of D-limonene loaded-PVA/psyllium husk showed that the more essential oil there is in the spinning solution, the thinner fibers can be obtained [19]. Furthermore, the existence of citral in the fiber indicated that it can be blended effectively with the polymer matrix thanks to the  $\beta$ -CD (Figure 1B1). When the cross-sectional SEM micrographs of the fibers were examined, it was determined that the best coating was in the PP sample, as well (Supplementary S1).

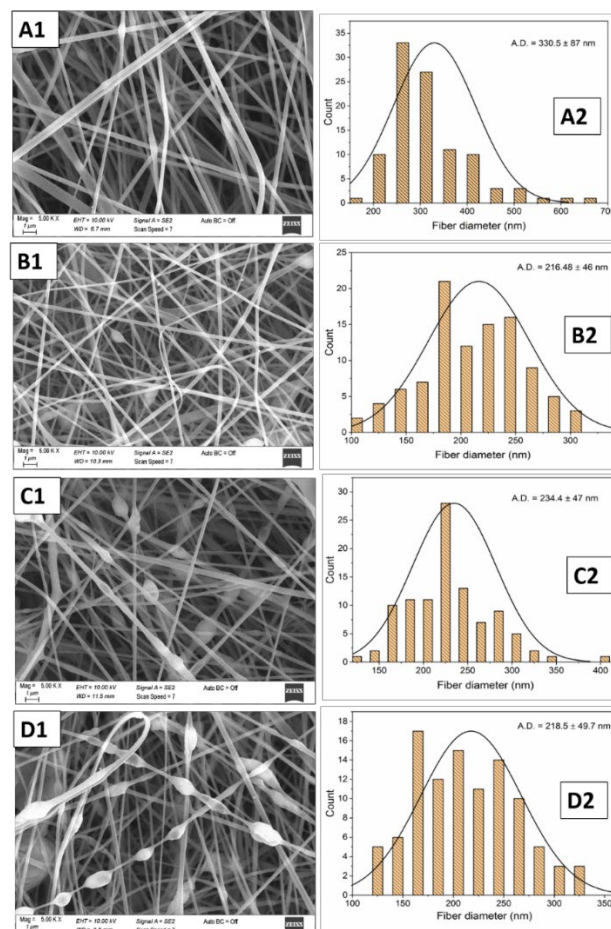


**Figure 1.** SEM micrographs and average fiber distributions of (A1-A2) neat PVA/whey protein nanofibers (PPWPC0), (B1-B2) PPWPC1 and (C1-C2) PPWPC2, and (D1-D2) PPWPC3.

### 3.2 FT-IR Spectroscopy

The chemical groups of the neat hybrid non-woven and also  $\beta$ -CD/citral loaded non-wovens were investigated by FT-IR (Figure 2). PP melt blown non-woven surfaces' FT-IR spectra showed typical asymmetric and symmetric stretching peaks at  $2948\text{ cm}^{-1}$  and  $2916\text{ cm}^{-1}$  (-CH) and  $2836\text{ cm}^{-1}$ , respectively. The other peaks appear at  $1455\text{ cm}^{-1}$ ,  $1376\text{ cm}^{-1}$ , and  $840\text{ cm}^{-1}$  belong to (-CH<sub>2</sub>) bending [10].

The characteristic absorption bands of PVA are as follows:  $3299\text{ cm}^{-1}$  (-OH stretching),  $2955\text{ cm}^{-1}$  and  $2861\text{ cm}^{-1}$  asymmetric and symmetric (-CH stretching),  $1418\text{ cm}^{-1}$  (-OH or -CH bending),  $1087\text{ cm}^{-1}$  (C-C stretching and -OH bending), and  $840\text{ cm}^{-1}$  (CH<sub>2</sub> rocking) [20,21]. Moreover, based on the literature the FT-IR bands of whey protein appears at ranging from  $3100$  to  $3500\text{ cm}^{-1}$  on protein strings associated with -NH stretching and free -OH group, respectively. The peaks from  $2850\text{ cm}^{-1}$  to  $2980\text{ cm}^{-1}$  are linked with a C-H stretching, the band between  $1600 - 1700\text{ cm}^{-1}$  are related with amide-I (C=O stretching and C-N stretching), the band formed in  $1400$  to  $1550\text{ cm}^{-1}$  related to amide-II (-NH bending), the peaks at  $1200 - 1350\text{ cm}^{-1}$  are related to amide-III (-CN stretching and -NH in plane bending vibration) [22-24]. The presence of these bands indicated that whey protein had been absorbed into the PVA blended nanofibers, as did whey protein's triple helix structure. In this context, PPWPC0 sample has typical absorption peaks at  $3283\text{ cm}^{-1}$  which is related to PVA and whey protein (-OH stretching and -NH stretching), at  $2917\text{ cm}^{-1}$  is -CH stretching, the peaks at  $1733\text{ cm}^{-1}$  and  $1644\text{ cm}^{-1}$  attributed with a -C=O stretching vibration band from carbonyl functional groups remaining after PVA synthesis from polyvinyl acetate hydrolysis or oxidation during preparation and amide-I, respectively. Amide-II is from whey protein and (-OH) bending from PVA are observed in  $1537\text{ cm}^{-1}$  and  $1424\text{ cm}^{-1}$ , respectively. The peaks at  $1374\text{ cm}^{-1}$ ,  $1324\text{ cm}^{-1}$ ,  $1243\text{ cm}^{-1}$  are belongs to amide-III (-CN stretching and -NH bending) and the peaks appears from PVA  $1080\text{ cm}^{-1}$  and  $1030\text{ cm}^{-1}$  (C-C stretching and -OH bending),  $840\text{ cm}^{-1}$  (CH<sub>2</sub> rocking), respectively. The peak value decrease in the peaks of  $1080\text{ cm}^{-1}$  and  $1030\text{ cm}^{-1}$  assigned with C-C stretching and -OH bending, is also indicated in the PPWPC1, PPWPC2 and PPWPC3 nanofibers by the addition of citral. The FT-IR spectra peaks of citral between  $2915\text{ cm}^{-1}$  and  $2856\text{ cm}^{-1}$  were assigned to CH<sub>3</sub> and CH<sub>2</sub> stretching vibrations, respectively, as shown in Figure 3. The -C=O stretching vibration peak was at  $1671\text{ cm}^{-1}$ , the C=C vibration peak was at  $1441\text{ cm}^{-1}$ , and the CH<sub>3</sub> bending vibration absorption peak was at about  $1376\text{ cm}^{-1}$  [25,26]. The characteristic peaks of citral overlaid with PVA/whey protein matrix, the matrix spectrum covered the presence of citral. This finding is parallel with the literature. In a study performed on the composite hydrogels, the characteristic peaks of citral are hidden in the polymer matrix [27]. Further, it is assumed that a small amount of citral use also causes this condition. In another study, it was reported that a new peak was formed by adding citral to hydrogels consisting of chitosan and carboxymethyl cellulose [28].

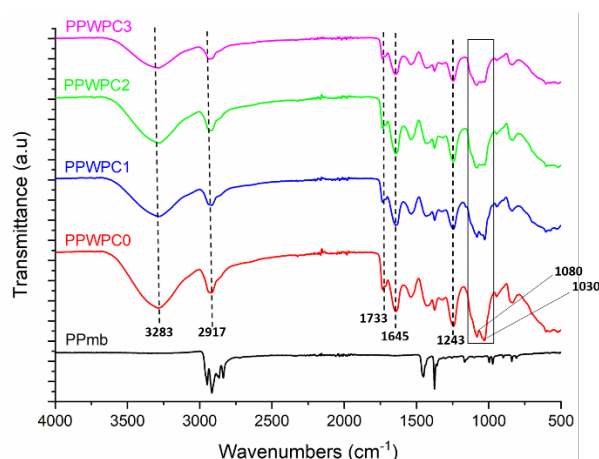


Figure 2. FT-IR spectrum of the all samples.

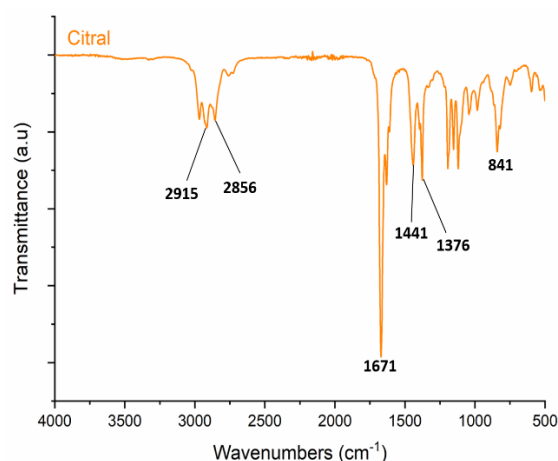


Figure 3. FT-IR spectrum of the citral.

### 3.3 Thermal Properties

Figure 4 indicates the thermal characteristic of the hybrid fibers. The weight loss of all samples has a slight initial weight loss between  $30-100^\circ\text{C}$  due to vaporization of free water. Single-step degradation has been observed for PP melt blown NWs at and  $350-470^\circ\text{C}$  (except for moisture loss). The TGA curve of neat PVA/whey protein nanofiber-coated PP non-woven (PPWPC0) and all citral-loaded PVA/whey protein-coated PP non-wovens (PPWPC1, PPWPC2, PPWPC3) samples have the same degradation profile and show 3-step breakdown (except for moisture loss). The initial degradation of neat sample PPWPC0 occurred between  $250^\circ\text{C}$  and  $400^\circ\text{C}$ , which may be related to both PVA and whey protein degradation. As previously reported, the side chain breakage of PVA started at  $200^\circ\text{C}$  and for whey protein degradation temperature at approximately  $270^\circ\text{C}$ , as well [20]. The second degradation step was found between  $400 - 500^\circ\text{C}$ . This is due to PVA's backbone breakdown, chain scission of PVA molecules dominated, and also the degradation of side groups that are separated from the whey protein's backbone [21]. After the last step ( $600 - 625^\circ\text{C}$ ) was the of the pyrolysis product produced throughout the analysis in the N<sub>2</sub>(g) environment. Interestingly, the degradation profiles of the neat sample (PPWPC0) and sample with max  $\beta$ -CD/citral ratio (PPWPC3) are very similar to each other. However, in the second stage, PPWP0 sample has more weight-loss than PPWP3 sample one. With the addition of citral essential oil to the structure, the heat

resistance reduces. It is predicted there is a strong interaction between the polymer matrix (PVA/whey protein) and  $\beta$ -CD/citral complex. It is known that essential oils are sensitive to heat and oxidation, and an increase in the amount of essential oil reduces the thermal resistance of the material in many studies [29].

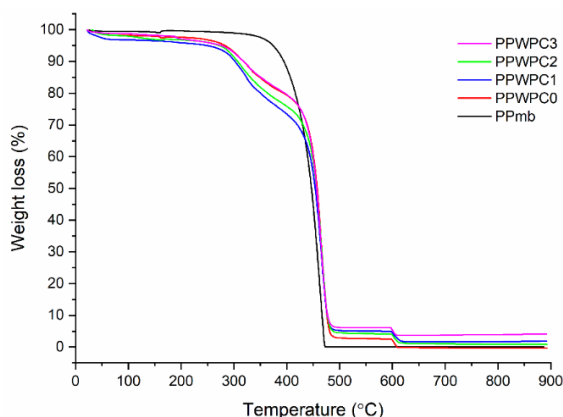


Figure 4. TGA thermograms of all samples.

### 3.4 Antibacterial Efficiency

The disk diffusion procedure was performed to investigate the antibacterial activity of neat (PPWPC0) and citral-loaded (PPWPC1, PPWPC2, and PPWPC3) samples against three species of bacteria (*E. coli*, *S. aureus*, and *P. aeruginosa*) (Table 2 and Figure 5).

Bacterial infections seem to be a serious healthcare concern as a result of the proliferation and distribution of multi-drug bacterial resistance, which has attracted the attention of researchers in developing novel antimicrobial therapies [30]. Citral has been shown to be a bacteriostatic agent against *Staphylococcus aureus* [31], *Listeria* [32],

and *Escherichia coli* [33], although the antibacterial mechanism has not been investigated further [34]. Citral's antimicrobial activity can damage cell walls of bacteria [3]. A study about the antibacterial mechanism of citral was performed by Tao et al. (2014) [35]. In this study, it is appointed that citral with *Penicillium italicum* provides for a decrease in lipid content in the bacteria, which inhibits membrane stability and enhances permeability of water-soluble compounds.

Despite its effectiveness against harmful microorganisms in many applications such as food,

pharmaceutical, medical, and cosmetic, citral still encounters significant obstacles in terms of use and application. In this regard, fabrication of citral loaded-PVA/whey protein nanofiber-coated PP non-wovens good approach for medical uses. As per Fig. 5, control sample (PWPC0) indicated no zone of inhibition for all bacteria. PPWPC3 sample indicates antibacterial activity against all type of bacteria due to the max  $\beta$ -CD/citral ratio (1:6). Further, all citral-containing samples (PPWPC1, PPWPC2, and PPWPC3) displayed antibacterial activity against *E. coli* bacteria. It is reported Gram (-) bacteria are often more resistant to plant extracts, oils, and their components than Gram (+) bacteria (*S. aureus*), owing to their more complex cell walls [36]. However, in this study samples with citral showed higher antibacterial efficiency against Gram (+) bacteria. Many studies suggest that some biological agents are more effective against Gram-positive bacteria [37,38]. Ma et al. (2020) reported that the synthesized citral-loaded chitosan/carboxymethyl cellulose hydrogels has good antibacterial effect against *E. coli* and *S. aureus*. [28]. As the  $\beta$ -CD/citral rate increased, the antibacterial activity of the samples increased, in this study. PWPC3 samples have the best antibacterial efficiencies against *Escherichia coli* with 14 mm and zone inhibition.

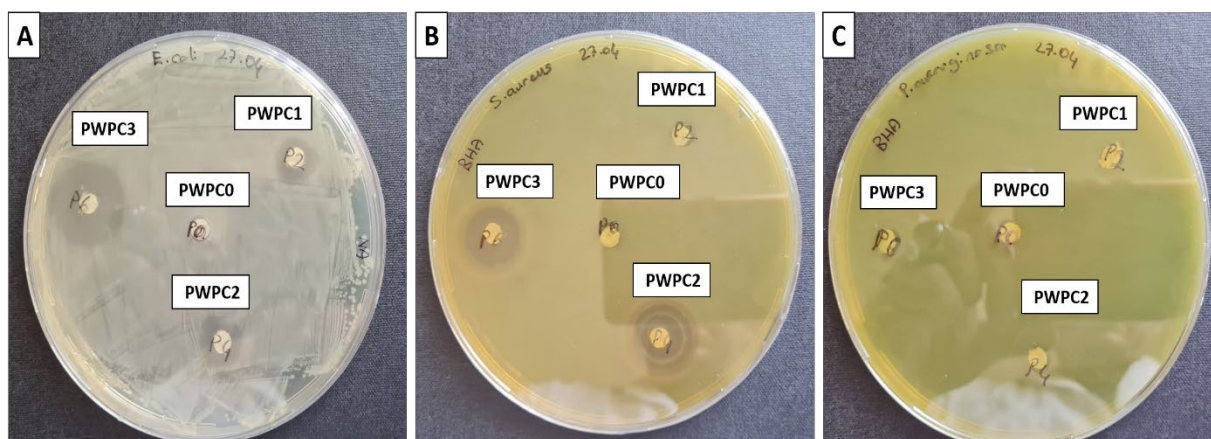


Figure 5. Antibacterial activities of the samples against A) *E. coli* B) *S. aureus* bacteria and C) *P. aeruginosa*

Table 2. Zone inhibition values of the hybride surfaces.

Sample ID	Inhibition Zone (mm)		
	<i>Escherichia coli</i>	<i>Staphylococcus aureus</i>	<i>Pseudomonas aeruginosa</i>
PPmb	-	-	-
PPWPC0	-	-	-
PPWPC1	8	-	-
PPWPC2	10	10	-
PPWPC3	14	12	-

## 4 Conclusion

In this study, PP melt blown non-woven surfaces successfully coated with PVA/whey protein/citral nanofibers via electrospinning. Citral was stabilized with  $\beta$ -CD, as a Pickering emulsifier. Therefore, Pickering emulsion solutions were formed to obtain bio-based nanofiber coatings in the electrospinning process. In general, the morphological results of the nanofiber coatings showed that the diameter of the fibers decreases due to the fact that the citral concentration reduces the viscosity of the solution. In addition, it was observed that the fiber morphology of the sample (PPWPC3) with the highest  $\beta$ -CD/citral ratio was disrupted. Nevertheless, it was concluded that the increase in concentration with the results of TGA provides resistance to the degradation of the material due to the interaction between matrix and  $\beta$ -CD/citral complex in the Pickering emulsions. According to FT-IR analysis, the obvious interaction between PVA/whey protein polymer matrices and  $\beta$ -CD/citral complexes has not been detected. The slight changes were appointed in the ranges of 1000 - 1200  $\text{cm}^{-1}$  band based on the increase of  $\beta$ -CD/citral complexes. The resulting materials have good antibacterial efficiencies between 8 – 14 mm against *E.coli*. Therefore, these new nanofiber-coated PP melt blowns developed with antibacterial activity might be used to bacterial infections. Nonetheless, more research on the materials' in vitro and in vivo cytotoxicity and wound scratch testing will be required. In summary, our findings provide insight on the role of good antibacterial efficiency as well as production process of new material for medical applications.

## Declaration

The authors declare that the ethics committee approval is not required for this study.

## References

- [1] Zhang, Y., Wei, J., Chen, H., Song, Z., Guo, H., Yuan, Y., & Yue, T. (2020). Antibacterial activity of essential oils against *Stenotrophomonas maltophilia* and the effect of citral on cell membrane. *LWT*, 117:108667.
- [2] Souza, V. V. M. A., Almeida, J. M., Barbosa, L. N., & Silva, N. C. C. (2022). Citral, carvacrol, eugenol and thymol: antimicrobial activity and its application in food. *Journal of Essential Oil Research*, 1-14.
- [3] Saddiq, A. A., & Khayat, S. A. (2010). Chemical and antimicrobial studies of monoterpene: Citral. *Pesticide Biochemistry and Physiology*, 98(1), 89-93.
- [4] Lu, W. C., Huang, D. W., Wang, C. C., Yeh, C. H., Tsai, J. C., Huang, Y. T., & Li, P. H. (2018). Preparation, characterization, and antimicrobial activity of nanoemulsions incorporating citral essential oil. *Journal of food and drug analysis*, 26(1), 82-89.
- [5] Shi, C., Song, K., Zhang, X., Sun, Y., Sui, Y., Chen, Y., Xia, X. (2016). Antimicrobial activity and possible mechanism of action of citral against *Cronobacter sakazakii*. *Plos one*, 11(7):e0159006.
- [6] Silva, C. D. B. D., Guterres, S. S., Weisheimer, V., & Schapoval, E. E. (2008). Antifungal activity of the lemongrass oil and citral against *Candida* spp. *Brazilian Journal of Infectious Diseases*, 12(1), 63-66.
- [7] Chao, S. C., Young, D. G., & Oberg, C. J. (2000). Screening for inhibitory activity of essential oils on selected bacteria, fungi and viruses. *Journal of essential oil research*, 12(5), 639-649.
- [8] Mokerizadeh, M., Kafil, H. S., Ghanbarzadeh, S., Alizadeh, A., & Hamishehkar, H. (2017). Improvement of citral antimicrobial activity by incorporation into nanostructured lipid carriers: a potential application in food stuffs as a natural preservative. *Research in Pharmaceutical Sciences*, 12(5), 409.
- [9] Parin, F. N., Terzioğlu, P., Sicak, Y., Yildirim, K., & Öztürk, M. (2021). Pine honey-loaded electrospun poly (vinyl alcohol)/gelatin nanofibers with antioxidant properties. *The Journal of The Textile Institute*, 112(4), 628-635.
- [10] Parin, F. N., & Yıldırım, K. (2021). Preparation and characterisation of vitamin-loaded electrospun nanofibres as promising transdermal patches. *Fibres & Textiles in Eastern Europe*.
- [11] Parin, F. N., Aydemir, Ç. İ., Taner, G., & Yıldırım, K. (2021). Co-electrospun-electrosprayed PVA/folic acid nanofibers for transdermal drug delivery: Preparation, characterization, and in vitro cytocompatibility. *Journal of Industrial Textiles*, 1528083721997185.
- [12] Parin, F. N., & Parin, U. (2022). Spirulina Biomass-Loaded Thermoplastic Polyurethane/Polycaprolactone (TPU/PCL) Nanofibrous Mats: Fabrication, Characterization, and Antibacterial Activity as Potential Wound Healing. *ChemistrySelect*, 7(8):e202104148.
- [13] Parin, F. N., & Terzioğlu, P. (2022). Electrospun Porous Biobased Polymer Mats for Biomedical Applications, In *Advanced Functional Porous Materials*. Springer, Cham., 539-586.
- [14] Çobanoğlu, B., Parin, F. N., & Yildirim, K. (2021). Production and characterization of n-halamine based polyvinyl chloride (pvc) nanowebs. *Textile and Apparel*, 31(3), 147-155.
- [15] Hu, J. W., Yen, M. W., Wang, A. J., & Chu, I. M. (2018). Effect of oil structure on cyclodextrin-based Pickering emulsions for bupivacaine topical application. *Colloids and Surfaces B: Biointerfaces*, 161, 51-58.
- [16] Li, C., Luo, X., Li, L., Cai, Y., Kang, X., & Li, P. (2022). Carboxymethyl chitosan-based electrospun nanofibers with high citral-loading for potential anti-infection wound dressings. *International Journal of Biological Macromolecules*, 209, 344-355.
- [17] Tatlisu, N. B., Yilmaz, M. T., & Arici, M. (2019). Fabrication and characterization of thymol-loaded nanofiber mats as a novel antimould surface material for coating cheese surface. *Food Packaging and Shelf Life*, 21:100347.
- [18] Kim, J. H., Lee, H., Jatoi, A. W., Im, S. S., Lee, J. S., & Kim, I. S. (2016). Juniperus chinensis extracts loaded PVA nanofiber: Enhanced antibacterial activity. *Materials Letters*, 181, 367-370.
- [19] Parin, F. N., Ullah, A., Yeşilyurt, A., Parin, U., Haider, M. K., & Kharaghani, D. (2022). Development of PVA-psyllium husk meshes via emulsion electrospinning: Preparation, characterization, and antibacterial activity. *Polymers*, 14(7), 1490.
- [20] Iqbal, B., Muhammad, N., Rahim, A., Iqbal, F., Sharif, F., Safi, S. Z., ... & Rehman, I. U. (2019). Development of collagen/PVA composites patches for osteochondral defects using a green processing of ionic liquid. *International Journal of Polymeric Materials and Polymeric Biomaterials*, 68(10), 590-596.

- [21] El Moujahed, S., Errachidi, F., Abou Oualid, H., Botezatu-Dediu, A. V., Chahdi, F. O., Rodi, Y. K., & Dinica, R. M. (2022). Extraction of insoluble fibrous collagen for characterization and crosslinking with phenolic compounds from pomegranate byproducts for leather tanning applications. *RSC advances*, 12(7), 4175–4186.
- [22] Agudelo-Cuartas, C., Granda-Restrepo, D., Sobral, P. J., & Castro, W. (2021). Determination of mechanical properties of whey protein films during accelerated aging: application of FTIR profiles and chemometric tools. *Journal of Food Process Engineering*, 44(5):e13477.
- [23] Agudelo-Cuartas, C., Granda-Restrepo, D., Sobral, P. J., Hernandez, H., & Castro, W. (2020). Characterization of whey protein-based films incorporated with natamycin and nanoemulsion of  $\alpha$ -tocopherol. *Heliyon*, 6(4):e03809.
- [24] Ghadetaj, A., Almasi, H., & Mehryar, L. (2018). Development and characterization of whey protein isolate active films containing nanoemulsions of *Grammosciadium ptrocarpum* Bioss. essential oil. *Food packaging and shelf life*, 16, 31-40.
- [25] Tian, H., Lu, Z., Li, D., & Hu, J. (2018). Preparation and characterization of citral-loaded solid lipid nanoparticles. *Food Chemistry*, 248, 78-85.
- [26] Zhou, W., Lin, J., Wu, R., Lin, W., Ge, F., & Huang, H. (2005). Direct synthesis of lemonile from *litsea cubeba* oil. *Fine Chem*, 22, 515-517.
- [27] Peng, R., Zhang, J., Du, C., Li, Q., Hu, A., Liu, C., ... & Yin, W. (2021). Investigation of the Release Mechanism and Mould Resistance of Citral-Loaded Bamboo Strips. *Polymers*, 13(19), 3314.
- [28] Ma, H., Zhao, Y., Lu, Z., Xing, R., Yao, X., Jin, Z., ... & Yu, F. (2020). Citral-loaded chitosan/carboxymethyl cellulose copolymer hydrogel microspheres with improved antimicrobial effects for plant protection. *International Journal of Biological Macromolecules*, 164, 986-993.
- [29] Turek, C., & Stintzing, F. C. (2013). Stability of essential oils: a review. *Comprehensive reviews in food science and food safety*, 12(1), 40-53.
- [30] Vasconcelos, N. G., Croda, J., & Simionatto, S. (2018). Antibacterial mechanisms of cinnamon and its constituents: A review. *Microbial pathogenesis*, 120, 198-203.
- [31] Porfirio, E. M., Melo, H. M., Pereira, A. M. G., Cavalcante, T., Gomes, G. A., Carvalho, M., & Costa, R. (2017). In vitro antibacterial and antibiofilm activity of lippia alba essential oil, citral, and carvone against *Staphylococcus aureus*. *The Scientific World Journal*, 124(2), 379–388.
- [32] Silva-Angulo, A. B., Zanini, S. F., Rodrigo, D., Klein, G., & Martine, A. (2015). Comparative study of the effects of citral on the growth and injury of *Listeria innocua* and *Listeria monocytogenes* cells. *Plos One*, 10(2).
- [33] Belda-Galbis, C. M., Pina-Perez, M. C., Leufven, A., Martinez, A., & Rodrigo, D. (2013). Impact assessment of carvacrol and citral effect on *Escherichia coli* K12 and *Listeria innocua* growth. *Food Control*, 33(2), 536–544.
- [34] Kang, S., Li, X., Xing, Z., Liu, X., Bai, X., Yang, Y., & Shi, C. (2022). Antibacterial effect of citral on *Yersinia enterocolitica* and its mechanism. *Food Control*, 135, 108775.
- [35] Tao, N., OuYang, Q., & Jia, L. (2014). Citral inhibits mycelial growth of *Penicillium italicum* by a membrane damage mechanism. *Food Control*, 41, 116-121.
- [36] Trombetta, D., Castelli, F., Sarpietro, M. G., Venuti, V., Cristani, M., Daniele, C., ... & Bisignano, G. (2005). Mechanisms of antibacterial action of three monoterpenes. *Antimicrobial agents and chemotherapy*, 49(6), 2474-2478.
- [37] Nimmagadda, A., Liu, X., Teng, P., Su, M., Li, Y., Qiao, Q., ... & Cai, J. (2017). Polycarbonates with potent and selective antimicrobial activity toward gram-positive bacteria. *Biomacromolecules*, 18(1), 87-95.
- [38] Tavares, T. D., Antunes, J. C., Padrão, J., Ribeiro, A. I., Zille, A., Amorim, M. T. P., ... & Felgueiras, H. P. (2020). Activity of specialized biomolecules against gram-positive and gram-negative bacteria. *Antibiotics*, 9(6), 314.



## REDUCING ROCKFALL HAZARDS IN SABIHA GOKÇEN – TAVSANTEPE METRO PROJECT CONSTRUCTION BY USING ROOT CAUSE ANALYSIS METHODOLOGY

Okan Özbakır\*<sup>1</sup> 

<sup>1</sup>Mine Technology Pro., VSHRTS, Igdir University, Igdir, Turkey

### Abstract

Original scientific paper

A realistic goal in efforts to reduce worker injuries related to rockfall incidents is to assess the conditions that create a rockfall hazard. If employers can properly assess the risks of rockfall and implement appropriate technical and administrative controls, they can better mitigate the risks. In order to achieve this goal, the methodology of Root Cause Analysis (RCA) can be considered as a method of risk assessment. An effective risk assessment method should include the ability to observe variable ceiling conditions and assess how much potential they represent for injuring workers. RCA's ability to prioritize the risks associated with changing conditions provides significant benefits to anyone responsible for designing, approving, or installing controls that are reasonably repeatable and stabilize the ceiling or reduce the risk of material falling from the roof. Herein, this study is based on a case analysis of the risks and causes of rock fall incidents in a metro construction project using the RCA methodology. This study explains the use of an RCA methodology that can help improve system-level failures and weaknesses, such as rocks falling from the ceiling of a tunnel. Furthermore, the present report examined the causes that led to the accidents and the predictors/variables were assessed using fishbone approach. Accordingly, inadequate training, lack of experience and the use of inappropriate equipment were identified as the causes of accidents. Careless behavior is also a major source of danger, in addition to failure to follow safety procedures.

**Keywords:** Rockfall, occupational health and safety, hazard, root cause analysis.

## SABIHA GÖKÇEN – TAVŞANTEPE METRO PROJESİ İNŞAATINDA KÖK NEDEN ANALİZİ METODOLOJİSİ KULLANILARAK KAYA DÜŞMESİ TEHLİKESİNİN AZALTILMASI

### Özet

Orijinal bilimsel makale

Bir metro inşaat projesindeki kaya düşmesi olaylarıyla ilişkili işçi yaralanmalarını azaltma çabalarında gerçekçi bir hedef, kaya düşmesi tehlikesi yaratan koşulları değerlendirmektir. İşverenler bu riskleri doğru bir şekilde değerlendirebilmesi ve uygun teknik ve idari kontrolleri uygulayabilmesi durumunda, riskleri daha iyi hafifletebilirler. Bu hedefi başarmak için Kök Neden Analizi (RCA) metodolojisi, risk değerlendirmesi yöntemi olarak düşünülebilir. Etkili bir risk değerlendirme yöntemi, değişken tavan koşullarını gözlemleme ve bunların işçileri ne kadar potansiyel olarak yaralayabileceğini değerlendirme yeteneğini içermelidir. RCA'nın değişen koşullarla ilişkili riskleri önceliklendirme yeteneği, tavanı istikrarlı hale getiren veya malzemenin tavanından düşme riskini azaltan kontrolleri tasarlama, onaylama veya kurma sorumluluğu olan herkes için önemli faydalar sağlar. Bu çalışma, bir metro inşaat projesindeki kaya düşmesi olaylarının risklerini ve nedenlerini RCA metodolojisi kullanarak bir vak'a analizi üzerinden incelemektedir. Bu çalışma, tavanın düşmesi gibi sistem düzeyindeki başarısızlıkları ve zayıflıkları geliştirmeye yardımcı olabilecek bir RCA metodolojisinin kullanımını açıklamaktadır. Ayrıca, mevcut raporlar, kazalara yol açan nedenler inceledi ve balık kılıcı yaklaşımını kullanarak bütün faktörler değerlendirildi. Buna göre, yetersiz eğitim, deneyimsizlik ve uygun olmayan ekipman kullanımı kazaların nedenleri olarak belirlendi. İhmalci davranışlar, güvenlik prosedürlerini izlemede başarısızlıkla birlikte, tehlike kaynaklarından biri olarak belirlendi.

**Anahtar Kelimeler:** Kaya düşmesi, iş sağlığı ve güvenliği, tehlike, kök neden analizi.

### 1 Introduction

Risks and hazards in the global competitive markets can have a devastating impact on an organization, resulting in costly consequences. Therefore, preventing risks and hazards within their own operations or products is a major

concern for any organization. Risk assessment studies, workplace accidents, maintenance programs and strategies are designed and implemented with the negative consequences of machine or equipment failure in mind, minimizing unplanned downtime caused by such failures. [1]. It is clear that for organizations, particularly those

\*Corresponding author.

E-mail address: okan.ozbakir@igdir.edu.tr (O. Özbakır)

Received 13 October 2023; Received in revised form 12 February 2024; Accepted 15 April 2024

2587-1943 | © 2024 IJIEA. All rights reserved.

Doi: <https://doi.org/10.46460/ijiea.1375469>

operating in an expanding global economy, the cost of error can be very high and it is easy to see how failures affect the organization's ability to compete [2]. As a result, organizations often develop and implement innovative strategies, both technical and managerial, which are critical to achieving sustainable success.

As organizations incur significant costs due to unexpected downtime, it is important to learn from mistakes by identifying their causes and preventing their recurrence. However, resources for research and analysis must be made available to achieve this goal [3]. This leads to the question: "How can we reduce the cost of investment in identifying the causes of failure?"

Root cause analysis (RCA), an effective method for achieving this goal, focuses on identifying the root cause of a failure through systematic causal analysis [4]. To achieve this goal, RCA uses a variety of methods and tools. The choice of these should be in accordance with their location and purpose. These include Pareto charts, Failure Mode and Effect Analysis (FMEA), 5 Whys, Ishikawa Fishbone Diagram, Fault Tree Analysis, 8D Report Template Checklist. However, there are three main barriers to using RCA. The first is that the methods and tools used to carry out RCA can be quite complex and difficult to use. This can result in RCA being used less frequently, taking more time and making it more difficult to maximize the learning potential within the organization. Secondly, some RCA methods or tools may require specialized software applications. These may have limited access and may require an initial capital investment. Thirdly, some methods or tools must be rigidly applied, which limits creativity and increases the likelihood of missing or abbreviating the real root cause(s) [5]. This is a method that focuses on identifying the root causes of a current event and subsequent events [6]. This method aims to solve the problem in its entirety by identifying the underlying causes, rather than focusing on a specific cause or effect of the problem. Therefore, in order to make it more effective, it needs to be made simpler, faster, and more reliable. To achieve this goal, RCA methods should be made more user-friendly within the company, accessible open source software should be used, and processes should be tailored to the organization's characteristics. As a result, there will be a reduction in costs and organizations will be able to make their risk analysis processes faster and more effective.

Instead of a culture of responsibility, there is a culture of blame in organizations. For RCA to be used effectively, it is important that the organization adopts a learning culture and encourages responsibility rather than blame in the problem-solving process. In this context, organizations must train their employees, encourage their identification of problems and offer solutions [7]. The lack of training and risk awareness among employees is another major obstacle to achieving this goal. In order to use RCA effectively, it is necessary to have a trained team that is familiar with the methodology. Especially, it is important to have the knowledge and skills necessary to understand the basic principles and tools of RCA, to ask the right questions, and to analyze the right data. Organizations need to invest in staff training programs, methods and tools.

They may also need to hire experts or set up a dedicated team. The fact that the studies require detailed

analysis and data collection processes can create difficulties for organizations in terms of time and resources. The implementation of RCA needs to be prioritized and supported by all relevant stakeholders. It is also important that the budget planning process includes the allocation of an appropriate budget to provide the necessary resources.

In this study, a qualitative root cause analysis was applied to the rockfall event that occurred during tunnel excavation and support works, the subsequent events, and the effects of possible mitigation measures. In this RCA model, the fishbone method has been used for the consideration of each parameter in the chain of events leading to the accident. In assessing the rockfall initiating events, factors resulting from formation characteristics, support methods and material properties were investigated. A detailed study of the near misses or minor injuries that can occur in tunnelling, which is considered one of the most dangerous workplaces in terms of occupational health and safety, will help to develop strategies to prevent accidents from reaching a potentially serious level.

The metro tunnel connecting Sabiha Gökçen Airport and Tavşantepe station, the construction of which started in March 2015, has a length of 15 kilometers and there are a total of 4 stations on the line. Upon completion, the project will connect the airport to Istanbul's existing metro system. It is expected to reach a capacity of one million passengers per month.

According to the data of the Social Security Institute of 2022, 4491 work accidents occurred in tunnel and railway construction in our country, 11 of them resulted in death, 1090 of them in the form of injuries requiring more than five days of treatment. Similar accidents cannot be prevented, although all such accidents are analyzed and recommendations are made. Such a high rate of accidents can be explained with the not learned from the past experiences. The rock fall accident, in which many workers were injured during excavation and support activities in the study area, was the subject of analysis. Along with the present study, we hypothesized that, based on the former reports, the major reasons of the accident occurred in metro project could be associated with the environment and communication and education status of the personnel involved in the project. In order to test the hypothesis, we used a fishbone approach including "communication", "education", "and environment", "personnel factors".

## 2 Literature Review

Today, accident investigation and risk reduction, with a particular focus on occupational health and safety, are commonly used to analyze system and equipment failures by examining the reliability and maintenance practices of technological systems, identifying the causes of equipment malfunctions, and making improvements to prevent recurring problems [8-10]. Due to its widespread use in industry, it has also attracted interest in fields such as quality management, manufacturing, and services [11].

It performs detailed analysis to identify the root causes of errors or defects that occur at any stage of production, and then takes appropriate preventive action to ensure that these problems do not recur, thereby eliminating the causes of errors in the production process and improving quality

[12]. It also focuses on RCA business processes and investigates the reasons for errors in the structure of these processes [13], helping to construct a more efficient and effective workflow by identifying sources of errors in processes. Companies can reduce costs and increase customer satisfaction through the identification of errors in their processes [14].

Systems-based RCA is designed to combine change management, risk management and systems analysis applications [15]. It is also designed to deal with complex systems and use a systematic approach to understand problems and allocate resources effectively in large projects. It aims to identify potential errors in a system, determine their causes, and then produce appropriate solutions. System-based RCA considers errors and inconsistencies in subsystems by addressing the entire system. This provides a holistic view. If one of the components in the system fails, other components in the system may be affected [16]. Change management is the analysis of the impact of changes to a system and the implementation of appropriate measures. Risk management identifies potential risks and assesses their potential impact. Preventive measures are taken to mitigate risks.

In the area of occupational health and safety, RCA examines the reliability and maintenance practices of technological systems, as well as accident investigation and risk mitigation based on comprehensive data. Its aim is to identify the causes of equipment failures on the basis of all available evidence. In addition, data from similar incidents and experiences in other organizations can be used in RCA analysis. This data can help to understand the causes of past incidents and provide information on how to take preventative measures against possible future incidents [17].

In general, the RCA process begins with the formation of the team and continues with the definition of content and purpose and the collection of data. Identifying and structuring an appropriate method for analyzing the data collected is the most important step. As a result, corrective actions are taken and recommendations are made. To ensure that any additional risks or malfunctions are eliminated, the system is controlled in a closed loop (Fig. 1.).

RCA is performed using special analysis techniques such as "5 Whys" technique, Failure Mode and Effect Analysis, Fault Tree Analysis, Fishbone or Ishikawa diagrams, Pareto Analysis, and Root Cause Mapping [18].

The root causes of a problem can be identified using these structured analysis techniques. For example, the "5 Whys" technique involves repeatedly asking the question "why?" to determine the causes of the problem and get to the root causes (Fig. 1.). In this way, we can get to the most fundamental causes of the problem. To identify the sources of faults in a system and assess their impact, Failure Mode and Effect Analysis is used [7]. A fault tree analysis is a diagram that shows the causes of a failure in a system and the consequences of that failure. Fishbone diagrams, or Ishikawa diagrams, are graphical organisational tools that are used to identify the root causes of problems (Fig. 2.). To identify the most common causes of a problem, Pareto analysis is effective. Root Cause Mapping is a technique used to visualize all the factors involved in a problem and

understand how they relate to one another [19]. The use of these analytical techniques is therefore one of the critical elements in the success of RCA. Choosing appropriate techniques leads to precise identification of problem causes and development of appropriate solutions. Identifying the root causes of problems is made easier by this structured approach to RCA. This allows continuous system improvement.

Cioca and Moraru [20] used root cause analysis, a combined and systematic approach to risk, to assess the risk of fire and explosion in gas mines. Even a small fire can cause major disasters, resulting in a potential explosion or fire, if a flammable atmosphere is created. Budiyanto and Fernanda [21] reported that traffic accidents at the container terminal are the most likely to occur and are caused by negligence, resulting in damage to both people and equipment.

In addition, Shahhossein et al. [22] reported that the root causes of the possibility of failure in the implementation of large-scale construction projects are that most of the problems in the projects arise from financial concerns and deficiencies in the bidding process.

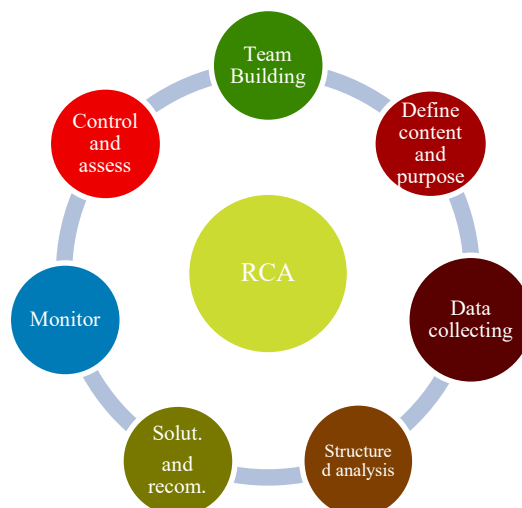


Figure 1. The steps of root cause analysis (RCA).

RCA is a process that starts with physical causes, progresses to human causes and finally to management or root causes, identifying the reasons for problems in order to develop solutions. In this way, the causes of any problems can be identified and appropriate corrective action can be in place. One of the outputs of RCA is the documentation of the data and evidence collected during the analysis process. These results will include findings in relation to the hypotheses that have been considered and the most likely root causes of the failure or loss. Hypotheses help to test different approaches to determine the cause of the problem. The results are presented based on the information obtained at the end of the analysis and provide a clear understanding of the causes of the problem. Recommendations for corrective action are one of the key outputs of RCA.

In order to prevent the recurrence of problems and to ensure continuous improvement of the system, these recommendations include warnings and suggestions. Based on the results of the analysis, recommendations for corrective action are determined and an appropriate plan

for implementing solutions is provided. All of these outputs are part of the RCA analysis process and are used to take appropriate corrective actions and provide the necessary information to prevent similar problems in the future.

A commonly used tool in root cause analysis is the Ishikawa diagram shown in Figure 2. This diagram covers efforts to prevent defects in production, marketing, and service processes and includes the identification of all factors that affect the outcome. The causes of each defect are considered as a variation and are grouped in the diagram. The diagram has a fish-like shape; the defect or problem is written on the right-hand side, while the causes are shown as spiky thorns. Subgroups may be expanded depending on the range of causes.

This approach aims to uncover underlying relationships between variables and provide additional information on possible causes. Causes are usually identified through brainstorming sessions and grouped into categories within major industries. In the context of occupational health and safety, accidents are generally considered to be caused by training, personal characteristics, the work environment, or communication (Fig. 2.). For example, situations such as inadequate lighting or a lack of training for staff can have a negative impact. Picking the right fishbone among the causes is important. This methodology contributes to quality control and process improvement by providing a systematic approach to root cause identification.

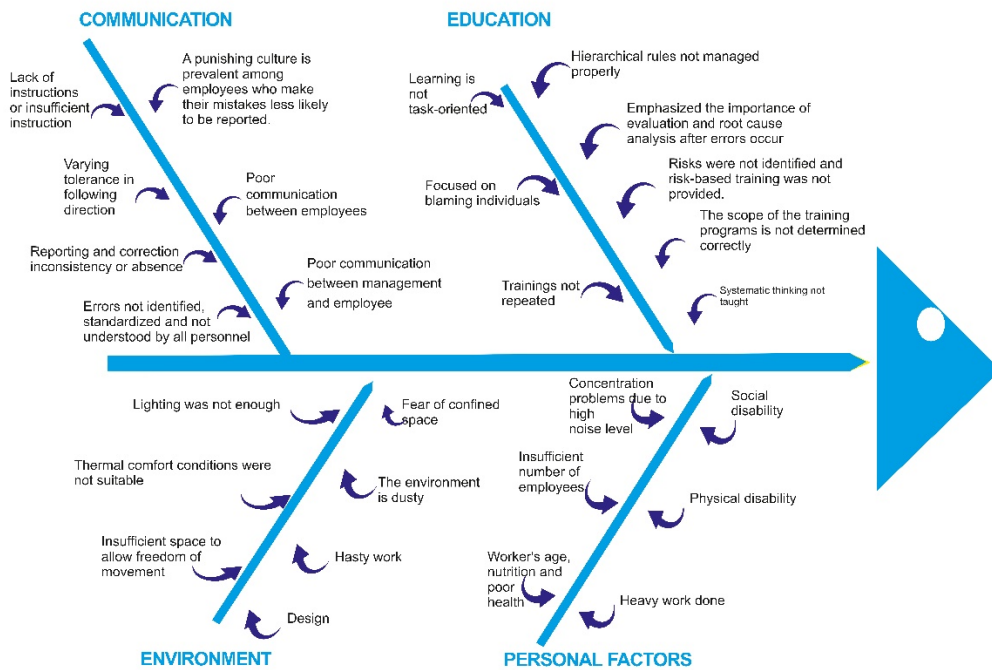


Figure 2. Fishbone or Ishikawa diagrams for root cause analysis (RCA).

### 3 Material and Method

There are two main purposes for the identification of the causes of accidents in the work place. The first is to identify the causes of failures through failure investigations and to provide information on the risk situation in the workplace. This information includes determining the cause of the failures, identifying working conditions, raising awareness of risks, and identifying possible precautions. Secondly, the data is used to understand and prevent similar failures. Data from individual accident investigations are used to analyze similar accidents that occur in similar workplaces and to develop preventive measures. The first step in separating the factors that contributed to the accident is to identify the visible causes that led to the accident.

A team of experts with the necessary expertise to analyse the problem is required to perform RCA correctly. The opinions of supervisors, engineers, technicians, quality control experts and experienced tunnel workers were taken into account at this stage. The ideas of these experts approach the problem from different perspectives

to understand the problem, identify the root causes, and support collaborative decision making. An investigation has been launched to gather information about the problem, including details of the time and place of the incident. The root cause of the problem or incident was determined and corrective actions developed by analyzing the data obtained. Using a results-oriented approach, the process continues with the evaluation of alternative solutions based on hypotheses. Were risks/hazards identified before the work was carried out? Were safety violations overlooked? Are there any design-related security flaws? Are the security systems in the environment working correctly? Was the work done in compliance with instructions? The identification of subfactors also includes the training that led to the accident, the way the work is performed and whether the work instructions are sufficient, as well as whether there are environmental factors that contribute to the accident (such as weather conditions, noise) and other factors that affect the worker's attention (such as overtime, stress, etc.). (Fig. 3.).

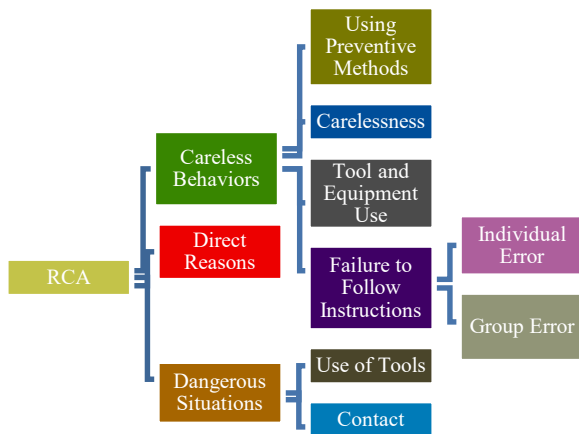


Figure 3. The search strategy of root cause analysis (RCA).

Through a systematic approach, this study identifies corrective actions to prevent the recurrence of the problem. Developing different solutions to the problem and implementing the most effective corrective action is the main purpose. Monitoring the implementation of corrective actions to ensure they are carried out correctly is the most critical step at this stage. The results of the implementation of the solutions should be evaluated and the necessary steps for further improvement should be in place. Analyzing data for accurate analysis, developing solutions, and continuously improving systems by identifying corrective actions prevents problems from recurring and continuously improves systems.

In this study, the causes of situations such as collapses and rock falls in tunnel excavation were examined in detail and a case study was presented using root cause analysis. In addition, the potential risks of these accidents were examined, emphasizing the need for engineering and administrative controls to prevent accidents and hazards. The aim was to identify the measures needed to prevent such accidents. This was done by analysing the causes of rockfalls in the Istanbul metro tunnel. A risk assessment was therefore carried out. The aim was to identify sources of risk and propose protective measures. The results of the study will provide guidance on how to prevent accidents during tunnel excavation.

#### 4 Rockfall Hazards and Moment of Accident

Tunnel support structures are structural systems installed during or after tunnel excavation to provide ground support, maintain the opening, limit groundwater ingress, support fixtures and provide a sub-base for the final surface. These structures can be used to provide initial stabilization, to provide permanent support to the ground, or both [23].

Although the lining of a tunnel is a structural system, it has different behavior and stability characteristics to other structural systems. Their interaction with their environment is the main reason for these differences. Loss or inadequate support from the surrounding ground can cause tunnel lining failure. The ability of the tunnel lining to deform under load is determined by the relative hardness of the tunnel lining and the surrounding soil.

Tunnel linings are generally more flexible than the surrounding soil, and this flexibility allows the lining to deform in response to soil deformations during and after

tunnel excavation. This deformation contributes to the development of strength and stability in the surrounding soil [24]. Due to the deformation of the tunnel lining, the moments redistribute the axial and eccentric loads within the lining. This shows that flexible and ductile tunnel liners are the most efficient [25].

Once excavation of the required tunnel opening has begun, the initial stress state is no longer valid and the excavated area is now subject to a new stress state. Soil is usually inhomogeneous and has been subject to large natural forces since excavation [26]. Once excavation is complete, appropriate support measures shall be taken to protect workers from falling materials, collapse hazards and other deterioration of the tunnel roof or crown. Figure 4 shows the material piled up in the working environment as a result of rocks falling from the excavation surface and roof following tunnel excavation.



Figure 4. Excavation surface and lining of surrounding rock.

In some formations, rockfalls can also occur if the face is not properly supported within a reasonable period of time after excavation. For these reasons, detailed field and laboratory studies should be carried out prior to excavation of underground structures to ensure proper and accurate reinforcement. This helps to prevent accidents and ensure safety at work [27].

As roof collapses and rock falls are among the most common causes of accidents in underground structures, it is necessary to understand the conditions that lead to them in order to prevent such incidents and take protective measures. The geological conditions, the stresses, the design of the tunnel and the impact on the environment can be noted as examples of these conditions [28]. In order to strengthen or balance the underground rocks, ground control is carried out. There are two stages for this purpose. In the first stage, measurements such as how excavation work will be done and which reinforcement will be used where are made during the design phase. The second stage consists of operational measurements. Depending on the design of the tunnel, measurements and precautions will be taken to adapt to changing conditions as the tunnel progresses [29].

Reinforcement systems should be designed in accordance with the geology, stress conditions and tunnel opening geometry. For a good reinforcement system, the dimensions and geometry of the tunnel should be well understood, and all factors such as blast damage, geological discontinuities and stress conditions should be taken into account. It is therefore necessary to investigate in detail all the factors that may have an influence on the

formation of roof collapses and rock falls. The scientific, impartial and targeted assessment and management of potential risks during tunnel construction is of the utmost importance. This ensures the safety of tunnel construction. It also minimizes the risk of loss of life and property. Therefore, risk assessment and management should be carried out with great care in the design and implementation of tunnel projects.

The "Underground Space Use: Analysis of the past and lessons for the future" report published by the International Tunneling and Underground Space Association (ITA) provides detailed statistics on accidents that occur during tunnel construction [30]. According to the report:

- Since 1950, there have been at least 340 accidents in tunnel construction around the world.
- At least 660 people died and thousands were injured in these accidents.
- The most common cause of accidents is roof or floor collapse. About 50% of these accidents are fatal.
- Fire, explosion, collision with work equipment and industrial accidents are other common causes of accidents.

An investigation has been carried out into the accident that took place on 04.03.2021. The accident occurred as part of the Sabiha Gökçen-Tavşantepe metro project. RCA analysis was used in the investigation. Similar accidents in all tunnels can be predicted from the findings and results of the accident investigation. The progress of the tunnel excavation started at 07:00 and was completed on schedule at 08:30 with the completion of the 0.8 metre excavation step. Immediately after the tunnelling machine emerged from the tunnel face, a loader was brought in to remove the excavated soil, which was completed at 09:30.

The excavated area was then covered with sprayed concrete, with a thickness of 5-10 cm, and reinforcement work began. However, the ground collapsed during the reinforcement work. A 1.5 to 2 cubic meter section of the ground fell on four workers. The workers were trapped under 30 kg of steel mesh, and the steel mesh they were holding also hung down to the ground due to its weight. Three of the workers suffered serious injuries such as fractures and crush injuries due to the falling materials, while the other worker survived the accident due to being positioned near the edge of the loader bucket. Between 2018 and 2021, there were nine accidents at different construction sites on the project, all as a result of material fall incidents. The investigations revealed that the common cause of all these accidents was falling material. Three of the accidents resulted in serious injuries, including broken feet and hips, while the rest of the accidents resulted in minor injuries. These data show that tunnelling is a high-risk activity.

The route on which the accident occurred is the Sultanbeyli Formation, a structure consisting of unconsolidated sand, gravel, clay and sometimes block-sized fragments with horizontal and vertical transitions. The layers of this formation are named Orhanlı Member, Dudullu Member, Tuğlacıbaşı Member, Altıntepe Member, and İkiz Tepeler Member, each having different lithological characteristics. Specifically related to the

examined accident, the left rear face of the Kuyruk Tunnel is located in the Orhanlı Member, which mainly consists of clay, silt, and fine sand-sized materials. These materials are bluish-gray when fresh and turn light brown as they weather. Fine-grained clay-silt materials dominate the rock type and occur as lenses and interbeds containing sand-gravel and block-sized unconsolidated materials in some areas. This formation also contains basal conglomerates of coarse material derived from the shoreline. Calcareous concretions are also present. Fine-grained clay-silt materials, which may contain varying amounts of limestone, predominate in all layers of the reservoir environment in the outlying parts of this formation.

## 5 Discussion

During the excavation, which was carried out entirely in the direction of tunnel advance, a 5cm layer of shotcrete was applied to the area opened up by the removal of the excavated material. The concrete was allowed to set for 15-30 minutes before reinforcing work began. During this process, however, particles of soil were falling on the workers when they broke off (Fig. 5). The soil excavated in the tunnel is generally composed of a clayey soil that contains sandy-clayey layers belonging to the Sultanbeyli Formation. Clay is a very cohesive material. However, it loses its cohesiveness when sand gets into it, and the sandy parts usually break and fall out [31]. Predicting fragmentation in such soils is extremely difficult [32]. In cases where we cannot prevent the main material from separating from the ground, it may not be possible to control or eliminate the hazard at source from an occupational safety perspective [33]. Therefore, control and prevention of this hazard must be achieved through the use of engineering methods. Techniques such as shotcrete, which is applied prior to excavation, are often used to prevent soil fragmentation. However, it was found that the shotcrete applied to the front of the fragment after an accident was not durable enough to hold the piece in place. There are two possibilities regarding the durability of the shotcrete used after the accident. The first possibility arises from the fact that the sprayed concrete may not have hardened sufficiently, which could result in inadequate strength.

However, there are a number of factors that can influence the setting process of the concrete [34], this requires an in-depth analysis by the quality department. According to the findings of the quality unit, the temperature values of the concrete produced at the time of the accident were approximately 12 degrees Celsius, and no evidence was found that the setting problem was caused by cold weather conditions. The concrete plant must therefore deal with any defects that may affect the concrete setting process. The second possibility is that the durability of the shotcrete that was applied was not sufficient to hold the separated piece in place. In the examination conducted by the Quality Unit, it was determined that the design and control studies of the shotcrete included cement and additive compliance tests, and the initial setting time of the concrete was approximately 1 minute. According to penetration measurements of 2.5 and 10 minutes in field tests, the

values range from 0.6 to 2.1 MPa, and according to laboratory compressive strength tests, the value ranges between 27.5 to 31.6 MPa one day later. Although the laboratory results are positive, the field tests do not confirm this.

For the concrete to hold the separated piece in place, high tensile strength is required [35]. This can be achieved by increasing the thickness of the concrete. However, there is a limit to the maximum thickness of shotcrete that can be applied without reinforcement [34]. Unreinforced shotcrete can be applied up to a maximum thickness of 7cm, and can be applied at greater thicknesses and the tensile strength of unreinforced concrete remains low (approximately 2 MPa) [36]. As an alternative, reinforced concrete can also be used to solve the problem. This can be achieved by installing a mesh on the excavated surface. However, this approach can lead to workers being exposed to more hazards. To increase the tensile strength of the shotcrete, steel wire can be incorporated into the shotcrete [37]. In this way, not only can the strength of the concrete be increased, but also the falling of material from the ground can be reduced, and any fallen pieces can fall over time. In this way, the falling of material can be largely prevented, or workers can be given time to escape from the danger zone because the separated material will not suddenly fall.

The main causes were the workers' desire to work quickly, which resulted in more people than normal being in the loader bucket (the maximum should have been three), and insufficient escape space in the event of an accident. The use of a suitable basket platform for the reinforcement work could have remedied this situation.

Compared to loaders, however, such basket machines are less manoeuvrable. In the event of a cave-in at height, the confined nature of the working area of these machines does not allow for rapid escape. Loaders are faster in this regard. In addition, to prevent workers from falling, the loader operator must be more careful when reversing. This was also a point of reference for the workers in their statements on the incident. Despite its shortcomings in this regard, the loader will always be faster and more advantageous than the basket machine in escaping from the danger zone (Figure 6.). The risk of overturning due to parts falling from the floor hitting the machine is another disadvantage of basket machines [38]. This can further worsen the possible outcome of the accident. However, it is important to remember that when using loaders, there is a risk of workers falling from the bucket during sudden reverse manoeuvres. Using different machines for each task in narrow areas such as tunnels is not very effective in terms of space.



Figure 5. Working environment in the tunnel.

CAUSES LEADING TO THE ACCIDENT

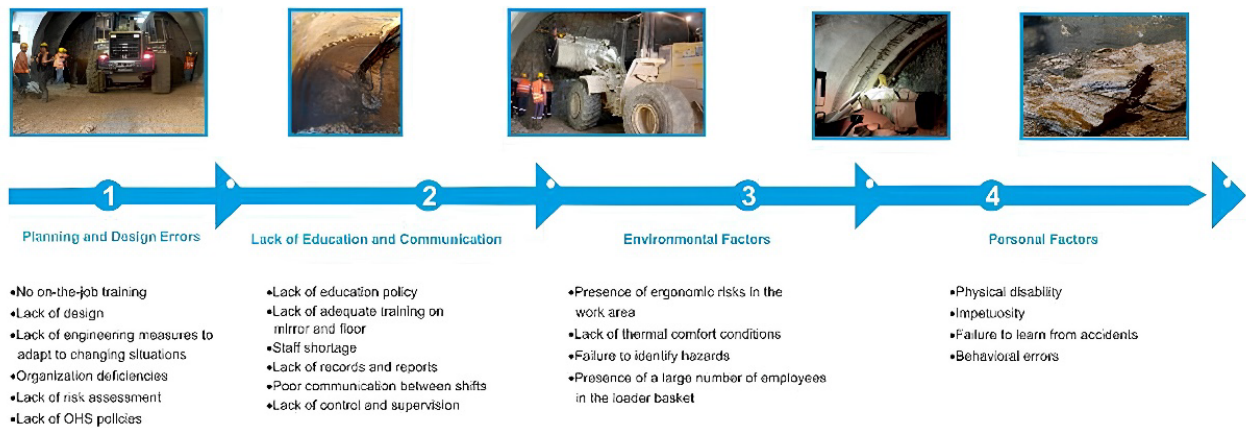


Figure 6. Causes leading to the accident.

Workplace-based training has been reviewed and its outcomes evaluated. The question "Why were these rules not followed?" was asked. Were these rules and procedures explained to those responsible, and was the importance of compliance understood? Do the control personnel have the necessary knowledge and experience? Negative answers to these questions are an indication that a safe environment has not been in place due to a lack of training. This can also be interpreted as a failure of management. The fact that the majority of workers answer 'yes' does not absolve employers of their responsibilities.

Providing training does not absolve employers of their responsibilities; monitoring the use of authority and responsibility is the responsibility of the employer [39].

6 Conclusion

According to the findings of the study, it can be concluded that personnel, management and communication problems are often identified as the causes of accidents. Such problems have been then manifested as critical risks, which in turn have caused accidents.

Personnel problems can result from inadequate training and experience of workers, inadequate knowledge of how to use appropriate equipment, failure to follow safety procedures and careless behavior. Management deficiencies include physical deficiencies such as inadequate infrastructure, non-compliance with legal requirements, unclear roles and inadequate risk management strategies. Communication problems can arise from interactional breakdowns between workers and managers, inadequate or incorrect transmission of instructions, lack of accurate information during emergencies, or misunderstandings among other factors. A key role in preventing accidents will therefore be played by improving the way people work, manage and communicate in the workplace.

As also underscored above, root Cause Analysis (RCA) is the systematic investigation of the underlying, hidden causes of a system failing or causing an adverse event. RCA is a structured and process-oriented framework. It aims to address systems and organizational issues. It avoids negative individual blame. However, there are also significant methodological limitations to the RCA. RCAs are typically uncontrolled case studies and it is impossible to know whether the root cause identified by the analysis was actually the cause of the accident due to the incomplete predictability of accidents. Furthermore, these analyses are retrospective and may be affected by hindsight bias. Other biases may be the result of the depth of the investigation into the causes, or the prevailing concerns of the day. It is therefore important to plan the RCA process well beforehand and to conduct the analysis objectively and unbiasedly.

## Declaration

Ethics committee approval is not required. The photos used in the manuscript were taken by the author of the study. For that reason, no any permission is required and no need to make any citations.

## References

- [1] Shagluf, A., Longstaff, A. P., & Fletcher, S. (2014). Maintenance strategies to reduce downtime due to machine positional errors.
- [2] Amit, R., & Schoemaker, P. J. (1993). Strategic assets and organizational rent. *Strategic management journal*, 14(1), 33-46.
- [3] Al-Najjar, B. (2007). The lack of maintenance and not maintenance which costs: A model to describe and quantify the impact of vibration-based maintenance on company's business. *International Journal of Production Economics*, 107(1), 260-273.
- [4] Shaqdan, K., Aran, S., Besheli, L. D., & Abujudeh, H. (2014). Root-cause analysis and health failure mode and effect analysis: two leading techniques in health care quality assessment. *Journal of the American College of Radiology*, 11(6), 572-579.
- [5] Wald, H., & Shojania, K. G. (2001). Root cause analysis. *Making health care safer: a critical analysis of patient safety practices*, 51.
- [6] Leszak, M., Perry, D. E., & Stoll, D. (2000, June). A case study in root cause defect analysis. In *Proceedings of the 22nd international conference on Software engineering* (pp. 428-437).
- [7] Dolansky, M. A., Druschel, K., Helba, M., & Courtney, K. (2013). Nursing student medication errors: a case study using root cause analysis. *Journal of professional nursing*, 29(2), 102-108.
- [8] Apostolakis, G. E. (2004). How useful is quantitative risk assessment? *Risk Analysis: An International Journal*, 24(3), 515-520.
- [9] Dash, A. K. (2019). Analysis of accidents due to slope failure in Indian opencast coal mines. *Current Science*, 117(2), 304-308.
- [10] Abrahamsen, E. B., Røed, W., & Jongejan, R. (2013). A practical approach for the evaluation of acceptable risk in road tunnels. *Journal of Risk Research*, 16(5), 625-633.
- [11] Borkovskaya, V., & Passmore, D. (2020, June). Risk reduction strategy and risk management on the basis of quality assessments. In *IOP Conference Series: Materials Science and Engineering*, 869(6), 1-11.
- [12] Jayswal, A., Li, X., Zanwar, A., Lou, H. H., & Huang, Y. (2011). A sustainability root cause analysis methodology and its application. *Computers & chemical engineering*, 35(12), 2786-2798.
- [13] Sulistiyowati, W. I. W. I. K., & Sari, I. K. A. S. (2018). A new redesign idea for dust filter tool used in gerandong crackers manufacturing process based on root cause analysis (RCA) and design for assembly (DFA) approach. *J. Eng. Sci. Technol*, 13(5), 1384-1395.
- [14] Zsidisin, G. A., Ellram, L. M., Carter, J. R., & Cavinato, J. L. (2004). An analysis of supply risk assessment techniques. *International Journal of Physical Distribution & Logistics Management*, 34(5), 397-413.
- [15] Sharma, R. K., & Sharma, P. (2010). System failure behavior and maintenance decision making using, RCA, FMEA and FM. *Journal of Quality in Maintenance Engineering*, 16(1), 64-88.
- [16] Abdelgawad, M., & Fayek, A. R. (2010). Risk management in the construction industry using combined fuzzy FMEA and fuzzy AHP. *Journal of Construction Engineering and management*, 136(9), 1028-1036.
- [17] Percarpio, K. B., Watts, B. V., & Weeks, W. B. (2008). The effectiveness of root cause analysis: what does the literature tell us?. *The Joint Commission Journal on Quality and Patient Safety*, 34(7), 391-398.
- [18] Benjamin, S. J., Marathamuthu, M. S., & Murugaiah, U. (2015). The use of 5-WHYs technique to eliminate OEE's speed loss in a manufacturing firm. *Journal of Quality in Maintenance Engineering*, 21(4), 419-435.
- [19] York, D., Jin, K., Song, Q., & Li, H. (2014, March). Practical root cause analysis using cause mapping. In *Proceedings of the International Multi Conference of Engineers and Computer Scientists* (Vol. 2).
- [20] Cioca, I. L., & Moraru, R. I. (2012). Explosion and/or fire risk assessment methodology: a common approach, structured for underground coalmine environments. *Archives of Mining Sciences*, 57(1), 53-60.
- [21] Budiyanto, M. A., & Fernanda, H. (2020). Risk assessment of work accident in container terminals using the fault tree analysis method. *Journal of Marine Science and Engineering*, 8(6), 466.
- [22] Shahhossein, V., Afshar, M. R., & Amiri, O. (2018). The root causes of construction project failure. *Scientia Iranica*, 25(1), 93-108.
- [23] Hoek, E., & Bray, J. D. (1981). *Rock slope engineering*. CRC press.
- [24] Bieniawski, Z. T. (1984). *Rock mechanics design in mining and tunneling*.
- [25] Lunardi, G., Cassani, G., Gatti, M., Cullacciati, A., Pini, G. K., & Zenti, C. L. (2017). The application of Semi-Automatic Tubular Arch inside Boscaccio Tunnel: a new concept of primary lining. In *Proceedings of ITA-AITES World Tunnel Congress WTC*.

- [26] Esmailzadeh, A., Shirzad, P. J., & Haghshenas, S. S. (2017). Technical analysis of collapse in tunnel excavation and suggestion of preventing appropriate applicable methods (case study: sardasht dam second diversion tunnel). *Civ Eng J*, 3(9), 682-689.
- [27] Wang, X. (2020). *Safety Problems During Tunnel Excavation in China* (Doctoral dissertation, Politecnico di Torino).
- [28] Aneziris, O. N., Papazoglou, I. A., & Kallianiotis, D. (2010). Occupational risk of tunneling construction. *Safety science*, 48(8), 964-972.
- [29] Høien, A. H., & Nilsen, B. (2019). Analysis of the stabilising effect of ribs of reinforced sprayed concrete (RRS) in the Løren road tunnel. *Bulletin of Engineering Geology and the Environment*, 78, 1777-1793.
- [30] Erdem, Y., & Solak, T. (Eds.). (2005). *Underground Space Use: Analysis of the Past and Lessons for the Future: Proceedings of the 31st ITA-AITES World Tunnel Congress, 7-12 May 2005, Istanbul, Turkey*. AA Balkema Publishers.
- [31] Hage, S., Hubert-Ferrari, A., Lamair, L., Avcı, U., El Ouahabi, M., Van Daele, M., ... & Plenevaux, A. (2017). Flow dynamics at the origin of thin clayey sand lacustrine turbidites: Examples from Lake Hazar, Turkey. *Sedimentology*, 64(7), 1929-1956.
- [32] Mulder, T. (2011). Gravity processes and deposits on continental slope, rise and abyssal plains. In *Developments in Sedimentology* (Vol. 63, pp. 25-148).
- [33] Pamukcu, C. (2015). Analysis and management of risks experienced in tunnel construction. *Acta Montanistica Slovaca*, 20(4).
- [34] Bernard, E. S., & Thomas, A. H. (2020). Fibre reinforced sprayed concrete for ground support. *TAI Journal (A Half Yearly Technical Journal Of Indian Chapter Of TAI)*, 9(1), 13-33.
- [35] Mander, J. B., Priestley, M. J., & Park, R. (1988). Theoretical stress-strain model for confined concrete. *Journal of structural engineering*, 114(8), 1804-1826.
- [36] Kasper, T., Edvardsen, C., Wittneben, G., & Neumann, D. (2008). Lining design for the district heating tunnel in Copenhagen with steel fibre reinforced concrete segments. *Tunnelling and Underground Space Technology*, 23(5), 574-587.
- [37] Vandewalle, M. (1998). Use of steel fibre reinforced shotcrete for the support of mine openings. *Journal of The South African Institute of Mining and Metallurgy*, 98(3), 113-120.
- [38] King, R. A. (2012). *Analysis of crane and lifting accidents in North America from 2004 to 2010* (Doctoral dissertation, Massachusetts Institute of Technology).
- [39] Niu, S. (2010). Ergonomics and occupational safety and health: An ILO perspective. *Applied ergonomics*, 41(6), 744-753.



## ELEMENTAL ANALYSIS AND DETERMINATION OF TOTAL PHENOLIC AND FLAVONOID CONTENT OF *RHEUM RIBES* L. BARK

İdris Yolbaş<sup>\*1</sup> 

<sup>1</sup>Türk Telekom Science High School, Siirt, Türkiye

### Abstract

Original scientific paper

Increasing evidence shows that *Rheum ribes* bark exhibits therapeutic and pharmacological effects. Therefore, we determined the total phenolic and flavonoid content and performed elemental analysis of *R. ribes* bark using inductively coupled plasma mass spectrometry. The results indicated a phenolic content of  $0,61 \pm 0,001$  mg gallic acid-equivalent/g sample and a flavonoid content of  $0,327 \pm 0,026$  mg catechin-equivalent/100 g sample. Elemental analysis of *R. ribes* bark revealed the presence of numerous essential elements, including Fe, K, Ca, Na, Al, and Mg. Our results show that *R. ribes* bark contains high levels of phenolic and flavonoid compounds and is a source of various important elements. Consequently, it may offer health benefits and might prove to be a valuable resource for the pharmaceutical and food industries.

**Keywords:** Antioxidant; flavonoid; phenolic; trace element; *Rheum ribes*.

### 1 Introduction

Plant oils and extracts possess several therapeutic properties and are extensively used in pharmaceuticals and alternative medicine. Antioxidants present in plants protect cells against harmful substances, prevent oxidation caused by free radicals, and can reduce the deleterious effects of disease such as chronic inflammation, obesity, diabetes, cardiovascular diseases, and cancer [1], [2]. Naturally produced antioxidants include vitamins A, C, and E, polyphenols, carotenoids, and flavonoids [3], [4]. Antioxidants often contain phenolic compounds [5], which are important bioactive compounds, and play key roles in defense responses, such as anti-aging, anti-inflammatory, antioxidant, and anti-proliferative activities [6]. Flavonoids are secondary plant metabolites that play important roles in regulating plant growth and inhibiting low-density lipoprotein oxidation [7], [8]. Additionally, plants contain various biologically important macro-elements, such as K, Ca, Mg, and Na, and trace elements, such as Fe, Zn, Cu, Mn, Mo, Cr, and Co, which are necessary for enzyme activity, growth, metabolism, and tissue health. Deficiencies in these elements lead to health problems, whereas excessive intake may result in toxic effects [9]. Although medicinal plants have not exhibited detrimental effects at concentrations evaluated to date, excessive intake of heavy metals negatively impacts human health [2], [10], [11]. Therefore, an accurate evaluation of the elemental composition of plants is pertinent [2], [12].

*R. ribes*, which belongs to the *Polygonaceae* family, has been an important food source and medicinal plant in

Turkey and other parts of the world since ancient times [13]. Annually, tons of *R. ribes* plant bark are discarded. Given its medicinal applications, we aimed to investigate its total phenolic and flavonoid contents, as well as the elemental composition of the bark.

### 2 Materials and Methods

#### 2.1 Collection of Plant Materials

Wild-growing *R. ribes* was collected from the Pervari district of Siirt province, Turkey, in early May 2023 (Figure 1). The bark of the collected plant samples was dried at 24 °C in a dark room for 1 month. Subsequently, the dried *R. ribes* bark was ground into powder under identical conditions and preserved for further analysis.



Figure 1. Photograph of *Rheum ribes* bark.

\*Corresponding author.

E-mail address: idrisyolbas@gmail.com (İ. Yolbaş)

Received 13 November 2023; Received in revised form 10 May 2024; Accepted 21 May 2024

2587-1943 | © 2024 IJIEA. All rights reserved.

Doi: <https://doi.org/10.46460/ijiea.1390339>

## 2.2 Extract Preparation

Five milliliters of 75% methanol containing 0.1% phosphoric acid were added to a 0,2 g powdered plant sample, mixed well, and homogenized using an ULTRA-TURRAX homogenizer (MS3-MaxiHomo35, Osaka, Japan) at 600 rpm for 30 s. The sample was centrifuged at 2500 rpm (Archer LC-05A, Istanbul, Türkiye) for 10 min at 24°C to obtain the supernatant, which was then incubated for 15 min in an ultrasonic water bath at 25°C. The extraction process was repeated twice, and the extracts were pooled. The final extract volume was adjusted to 10 mL with methanol, and the extract was transferred to 100 µL tubes.

## 2.3 Total Phenolic Content Determination

Folin–Ciocalteu reagent (FCR) is used to measure the total phenolic content of a substance. Phenolic compounds are antioxidants and can react with free radicals, reducing cellular damage. The FCR reacts with phenolic compounds, causing a color change that is proportional to the amount of phenolic compounds present. This test is commonly used in the food, beverage, and natural product industries to assess antioxidant capacity and is usually reported in terms of gallic acid equivalents. Briefly, 900 µL pure water (18,2 MΩ, Arium Pro Ultrapure Water System, Sartorius, Göttingen, Germany) and 5 mL 0,2 M FCR were added to 100 µL *R. ribes* extract. The mixture was shaken vigorously and allowed to rest for 8 min. Next, 5 mL 7.5% sodium carbonate was added to the mixture and vortexed for 20 s. The mixture was then incubated in the dark at 22–24°C for 2 h, after which the absorbance was measured at 765 nm using a spectrophotometer (Biochrom Libra S70 Double Beam Spectrophotometer, Cambridge, England).

## 2.4 Total Flavonoid Content Determination

The *R. ribes* extract (0,4 mL) or catechin standard was transferred to a 10-mL measuring cup, and 4 mL pure water was added. Then, 0,3 mL 5% NaNO<sub>2</sub> was added to the mixture and allowed to rest for 5 min. Next, 0,3 mL 10% AlCl<sub>3</sub> was added to the mixture and allowed to rest for 6 min. Finally, 2 mL 1 M NaOH and 3 mL distilled water were added to the mixture, shaken, and the absorbance measured at 510 nm using a spectrophotometer (Biochrom Libra S70 Double Beam Spectrophotometer, Cambridge, England). Pure water was used as a blank.

## 2.5 Inductively Coupled Plasma Mass Spectrometry Elemental Analysis

For inductively coupled plasma mass spectrometry (ICP–MS), a 1 g powdered *R. ribes* bark sample was transferred to a Teflon container. Next, 10 mL concentrated 65% nitric acid (Merck, Darmstadt, Germany) was added to each sample; 10 mL 65% nitric acid was added to an empty Teflon container and used as a blank. The Teflon containers were placed in a MARS 6 One Touch microwave digestion system (CEM, Matthews, NC, USA). The maximum temperature was increased to 210°C over 25 min and maintained for 15 min. Dissolution was performed in a closed system for 40 min. After the microwave temperature returned to 22–24°C, the solutions and Teflon container lids were thoroughly washed with ultrapure water and transferred to 50-mL volumetric flasks.

Calibration solutions for ICP–MS (Table 1) were prepared by diluting commercially available multi-element standards with 1% Suprapur nitric acid (Millipore Sigma, Burlington, MA, USA) in ultra-pure water and used to construct a calibration curve.

**Table 1.** Calibration standards.

Analytes	Std1 (ppb)	Std2 (ppb)	Std3 (ppb)	Std4 (ppb)	Std5 (ppb)	Std6 (ppb)	Internal standard
Li, B, Al, Ti, V, Cr, Mn, Co, Ni, Cu, Zn, Ga, As, Se, Rb, Sr, Nb, Mo, Ru, Pd, Ag, Cd, Sn, Ba, Hf, Ta, W, Au, Pb, U	0,5	1	5	25	50	100	<sup>89</sup> Y
Na, Mg, K, Ca, Fe	25	50	2,50	1250	2500	5000	

Appropriate sample dilutions were prepared, and ICP–MS analyses were performed on a NexION 2000B ICP mass spectrometer (PerkinElmer, Waltham, MA, USA) fitted with a quartz nebulizer, cyclonic spray chamber, and integrated auto-sampler under the operating conditions summarized in Table 2.

A washing solution containing 1% Suprapur nitric acid–ultrapure water was prepared at the concentrations

specified in Table 1, and 25 ppb <sup>89</sup>Y (Yttrium) was used as the internal standard. Samples were injected into the cyclonic spray chamber with argon gas flow via a peristaltic pump. In addition to argon, a high helium percentage was used to prevent interference. Syngistix for ICP–MS software version 2.2 (PerkinElmer) was used for instrument setup, data acquisition, and data analysis.

**Table 2.** Inductively coupled plasma mass spectrometry operating conditions.

Parameter	Description/Value
Nebulizer	MEINHARD plus Classic Type C
Spray chamber	Glass cyclonic (baffled), 4°C
One piece torch	w/2,5 mm Quartz Injector
Injector	2,0 mm i.d.
Nebulizer flow	Optimized for <2% oxides
Radio frequency power	1600 W
Cones	Ni
Replicates	3
Dwell time	50 ms
Aerosol dilution	Set to 2,5×
Sample delivery rate	350 µL/min
Rinse time	45 s
Nebulizer gas flow rate	0,93 L/min
Deflector voltage	Approximately 12 V
Analog stage voltage	Approximately 1750 V
Pulse stage voltage	1100 V
Discriminator threshold	26
Sample tubing (orange-yellow)	Flared PVC pump tubes 0,51 mm/0,89 mm
Internal standard tubing (orange-red)	Flared PVC pump tubes 0,19 mm/0,91 mm
Peristaltic pump speed	35 rpm
Alternating current rod offset	Approximately 4

### 3 Results and Discussion

#### 3.1 Total Phenolic Content

The *R. ribes* bark had a high phenolic content of  $0,61 \pm 0,001$  mg gallic acid-equivalent/g sample, as determined using the Folin–Ciocalteu method. A previously reported phenolic content for water, ethanol, and methanol extracts of *R. ribes* was 118,76, 125,07, and 136,82 mg, respectively [14]. Another study reported a total phenolic content of 35,71 mg pyrocatechol-equivalent/mg extract [15]. Although the bark of *R. ribes* may have a lower total phenolic content than other plant parts, these discarded portions still hold potential as valuable source material for health and dietary

supplements because of their phenolic components. Phenolic compounds are widely present in plants and have numerous health benefits, such as antioxidant, anticancer, and anti-inflammatory effects [16]. Their anticancer effects, including growth inhibition and cytotoxic effects, are under active investigation. *R. ribes* may therefore exert beneficial health effects, including antioxidant and anticancer activities.

#### 3.2 Total Flavonoids

In addition to the total phenolic content, the presence and amount of other bioactive compounds, such as flavonoids, tannins, and phytosterols [17], can affect the biological activity of *R. ribes* bark extract. We found that the total flavonoid content of the *R. ribes* bark extract was  $0,327 \pm 0,026$  mg catechin-equivalent/100 g sample. *R. ribes* plant extracts obtained using different methods are reportedly rich in flavonoids; water, ethanol, and

methanol extracts were previously shown to have a total flavonoid content of 2681,49, 2345,85, and 1239,74 mg catechin-equivalent/g extract, respectively [14]. Another study reported that the chloroform extract of *R. ribes* roots had the highest flavonoid content at  $145,59 \pm 0,22$  mg, whereas the methanol extract of the stems had the lowest content at  $13,66 \pm 0,75$  mg [15].

Flavonoids are plant-derived compounds with antioxidant, anti-inflammatory, anti-tumor, and antimicrobial properties and are therefore of pharmacological and biochemical interest. The current study indicates that *R. ribes* bark is a rich source of flavonoids, and further studies are required to investigate the health benefits of the bark and the bioavailability of the flavonoids.

#### 3.3 Elemental Analysis

The elemental analysis of *R. ribes* bark using ICP–MS revealed the presence of numerous elements (Table 3), with Fe, K, Ca, Na, Al, and Mg present at the highest concentrations. Therefore, *R. ribes* bark contains potentially valuable elements that can be used in various health and food applications.

Minerals and trace elements play important roles in various metabolic processes, and their deficiency or excess can lead to disease. For instance, Cu plays an important role in tissue regeneration, strengthening of bones, protein synthesis, energy production, and red blood cell formation [18]. However, excessive Cu intake can cause health problems. Similarly, Cd is a toxic element that can persist in the body, and high Cd levels in food can cause serious health problems [19]. K regulates water balance and facilitates the conversion of carbohydrates to glycogen [18], and Mg is important for regulating energy

metabolism, the muscle and nervous systems, bone formation, and blood pressure [20]. Se is a crucial element for human health, involved in reproduction, thyroid hormone metabolism, and protection against oxidative damage and infection through its role in the synthesis of enzymes such as selenoproteins [21]. Mn is an essential co-factor of metalloenzymes, especially superoxide dismutase [22]. Co contributes to the composition of

vitamin B12, which is essential for the production of red blood cells and the regulation of nervous system functions [23].

In summary, *R. ribes* can be used for food products and promoting health. It contains numerous essential minerals and trace elements, which makes it a valuable material for the food industry.

**Table 3.** Inductively coupled plasma mass spectrometry elemental analysis results.

<sup>7</sup> Li Helium KED High (ppb)	<sup>11</sup> B Helium KED High (ppb)	<sup>23</sup> Na Helium KED High (ppb)	<sup>24</sup> Mg Helium KED High (ppb)	<sup>27</sup> Al Helium KED High (ppb)
6756.584	144831.442	5942042.688	3023013.745	851856.794
<sup>39</sup> K Helium KED High (ppb)	<sup>43</sup> Ca Helium KED High (ppb)	<sup>48</sup> Ti Helium KED High (ppb)	<sup>51</sup> V Helium KED High (ppb)	<sup>52</sup> Cr Helium KED High (ppb)
37184914.979	8737640.163	17538.989	1587.996	5151.725
<sup>55</sup> Mn Helium KED High (ppb)	<sup>57</sup> Fe Helium KED High (ppb)	<sup>59</sup> Co Helium KED High (ppb)	<sup>60</sup> Ni Helium KED High (ppb)	<sup>63</sup> Cu Helium KED High (ppb)
20520.414	369547.785	1156.817	18777.943	11192.606
<sup>66</sup> Zn Helium KED High (ppb)	<sup>69</sup> Ga Helium KED High (ppb)	<sup>75</sup> As Helium KED High (ppb)	<sup>82</sup> Se Helium KED High (ppb)	<sup>85</sup> Rb Helium KED High (ppb)
463869.839	3701.328	1331.671	16891.835	43326.721
<sup>88</sup> Sr Helium KED High (ppb)	<sup>93</sup> Nb Helium KED High (ppb)	<sup>98</sup> Mo Helium KED High (ppb)	<sup>102</sup> Ru Helium KED High (ppb)	<sup>106</sup> Pd Helium KED High (ppb)
29873.875	1208.499	1570.078	544.923	1384.669
<sup>107</sup> Ag Helium KED High (ppb)	<sup>111</sup> Cd Helium KED High (ppb)	<sup>118</sup> Sn Helium KED High (ppb)	<sup>138</sup> Ba Helium KED High (ppb)	<sup>180</sup> Hf Helium KED High (ppb)
1491.508	1261.400	1800.098	15476.094	1315.541
<sup>181</sup> Ta Helium KED High (ppb)	<sup>184</sup> W Helium KED High (ppb)	<sup>197</sup> Au Helium KED High (ppb)	<sup>208</sup> Pb Helium KED High (ppb)	<sup>238</sup> U Helium KED High (ppb)
1788.306	2045.404	2297.684	20774.610	5548.620

\*KED; kinetic energy discrimination, ppb; parts per billion

#### 4 Conclusion

This study explored the potential use of abundant discarded *R. ribes* bark as a resource for the health and food industries. We analyzed the total phenolic and flavonoid content and determined the elemental composition of *R. ribes* bark and found that it contains a significant amount of phenolic and flavonoid compounds, suggesting that it may be a rich source of antioxidants and anticancer agents. Elemental analysis revealed elevated concentrations of essential minerals, including Fe, Ca, K, and Mg. Our results therefore imply that *R. ribes* bark contains bioactive compounds with potential health benefits.

This study has some limitations. First, the results of this study are limited to specific *R. ribes* bark samples from a particular region, which impacts genetic diversity and growth conditions. Further research involving larger

sample sizes is therefore necessary to validate our findings. Second, we used only microwave dissolution and ICP-MS in this study, and different analytical techniques may yield different results. Therefore, our findings should be corroborated by additional, comprehensive studies using diverse analytical methods. Assessing the overall impact of these variables on the results in greater detail will be crucial in future research endeavors. Additionally, in-depth studies are required to investigate the interactions between various bioactive components to elucidate the functional mechanisms involved in the positive impact of *R. ribes* bark on human health.

#### Declaration

Ethics committee approval is not required.

## References

- [1] Lindley, M. G. (1998). The impact of food processing on antioxidants in vegetable oils, fruits and vegetables. *Trends in Food Science & Technology*, 9(8–9), 336–340.
- [2] Yolbaş, İ. (2024). Phenolic Compound Content and Antioxidant Activity of *Rheum ribes* Shells. *Journal of Chemistry*, e9151180.
- [3] Güçlü, K., Apak, M. R., & Özyürek, M. (2009). Hidroksil ve Süperoksit Radikallerinin Süpürülmesine Dayalı Yeni Antioksidan Aktivite Tayin Yöntemlerinin Geliştirilmesi, *Tübitak Projesi*, 1–114.
- [4] Kähkönen, M. P., Hopia, A. I., Vuorela, H. J., Rauha, J. P., Pihlaja, K., Kujala, T. S., & Heinonen, M. (1999). Antioxidant activity of plant extracts containing phenolic compounds. *Journal of Agricultural and Food Chemistry*, 47(10), 3954–3962.
- [5] Croom, E. M., & Walker, L. (1995). Botanicals in the pharmacy: new life for old remedies, *Medical Economics Company*.
- [6] Uyar, B. B., Gezmen-karadağ, M., Şanlıer, N., & Günyel, S. (2013). Toplumumuzda Sıklıkla Kullanılan Bazı Bitkilerin Toplam Fenolik Madde Miktarlarının Saptanması *Gıda*, 38 (1): 23-29
- [7] Ali, F., Rahul, F. N., Jyoti, S., & Siddique, Y. H. (2017). Health functionality of apigenin: A review. *International Journal of Food Properties*, 20(6), 1197–1238.
- [8] Kolaç, T., Gürbüz, P., & Yetiş, G. (2017). Phenolic content and antioxidant characteristics of natural products. *İÜ Sağlık Hizmetleri Meslek Yüksekokulu Dergisi*, 5(1), 1-17.
- [9] Tchounwou, P. B., Yedjou, C. G., Patlolla, A. K., & Sutton, D. J. (2012). Heavy metal toxicity and the environment. *Molecular, clinical and environmental toxicology: volume 3: environmental toxicology*, 133-164.
- [10] Bal, S. Ş., Kurşat, M., Kuluöztürk, M. F., Karatepe, Ş., & Yılmaz, E. (2019). Determination of the radio-isotope activity concentration in some medicinal and aromatic plants in Bitlis. *ALKÜ Fen Bilimleri Dergisi*, 183–187.
- [11] Kerdiğe, K. (2019). *Karanfil bitkisinde (Syzygium aromaticum) uçucu bileşenlerin ve eser elementlerin analizi* (Master's dissertation, Inonu University).
- [12] Kılıç, O. (2020). *Trakya bölgesinde yetişen Allium rumelicum, Jurinea kilaea, Peucedanum obtusifolium bitkilerinin toplam fenolik, flavonoid madde, antioksidan ve antimikrobiyal özelliklerinin belirlenmesi* (Master's dissertation, Tekirdağ Namık Kemal University).
- [13] Bati, B., Celik, I., Turan, A., Eray, N., Alkan, E. E., & Zirek, A. K. (2023). Effect of isgin (*Rheum ribes* L.) on biochemical parameters, antioxidant activity and DNA damage in rats with obesity induced with high-calorie diet. *Archives of Physiology and Biochemistry*, 129(2), 298–306.
- [14] Keser, S., Keser, F., Karatepe, M., Kaygılı, O., Tekin, S., Turkoglu, I., Demir, E., Yılmaz, O., Kirbag, S., & Sandal, S. (2020). Bioactive contents, *in vitro* antiradical, antimicrobial, and cytotoxic properties of rhubarb (*Rheum ribes* L.) extracts. *Natural Product Research*, 34(23), 3353–3357.
- [15] Öztürk, M., Aydoğmuş-Öztürk, F., Duru, M. E., & Topçu, G. (2007). Antioxidant activity of stem and root extracts of Rhubarb (*Rheum ribes*): An edible medicinal plant. *Food chemistry*, 103(2), 623-630.
- [16] Njume, C., Afolayan, A. J., & Ndip, R. N. (2009). An overview of antimicrobial resistance and the future of medicinal plants in the treatment of Helicobacter pylori infections. *Afr. J. Pharm. Pharmacol*, 3(13), 685-699.
- [17] Veliöğlu, S. Gıda Kimyası-II, Retrieved 12 September, 2023 from [https://acikders.ankara.edu.tr/pluginfile.php/57141/mod\\_resource/content/0/1.A%C3%87IKDERS-GIDA%20K%C4%B0MYASI-II.pdf](https://acikders.ankara.edu.tr/pluginfile.php/57141/mod_resource/content/0/1.A%C3%87IKDERS-GIDA%20K%C4%B0MYASI-II.pdf)
- [18] Tosun, E. (2009). Hastalık tedavisinde kullanılan bazı meyve ve sebzelerin dokularında eser element ve mineral tayini (Master's dissertation, Inonu University).
- [19] Gadd, G. M., Griffiths, A. J. Microorganisms and heavy metal toxicity. *Microbial Ecology*, 4(4), 303–317.
- [20] Eroğlu Samur, G. (2012). Vitaminler Mineraller ve Sağlığımız. Retrieved 12 September 2023 from <https://hsgm.saglik.gov.tr/depo/birimler/saglikli-beslenme-ve-hareketli-hayat-db/Dokumanlar/Kitaplar/Vitamin-Mineral-Sagligimiz.pdf>
- [21] N. Lajçi, M. Sadiku, X. Lajçi, B. Baruti, ve S. Nikshiq, “Assessment of major and trace elements of fresh water springs in village Pepaj, Rugova region, Kosova”, *Journal of International Environmental Application and Science*, c. 12, sy 2, ss. 112-120, 2017.
- [22] I. Knerr, H. Blessing, S. Seyferth, R. J. Watling, ve M. A. Chaudhri, “Evaluation of plasma trace element and mineral status in children and adolescents with phenylketonuria using data from inductively-coupled-plasma atomic emission and mass spectrometric analysis”, *Annals of Nutrition and Metabolism*, c. 63, sy 1-2, ss. 168-173, 2013.
- [23] R. V. Derrell, (1991). “Trace Elements in Human Nutrition *Micronutrients in Agriculture, SSSA Book Series 4*”. USA, 1991.



## EXAMINING ARCHITECTURAL PROJECT APPLICATIONS WITH PHOTOGRAMMETRIC POINT CLOUD: İĞDIR UNIVERSITY MOSQUE

Selim Kartal<sup>\*1</sup>, Emirhan Özdemir<sup>2</sup>, Rüştü Çallı<sup>2</sup>

<sup>1</sup>İğdir Üniversitesi, Teknik Bilimler MYO, Tasarım Bölümü, İğdir, Türkiye

<sup>2</sup>İğdir Üniversitesi, Teknik Bilimler MYO, Mimarlık ve Şehir Planlama, İğdir, Türkiye

### Abstract

Original scientific paper

In accordance with the developments in today's technology, the use of unmanned aerial vehicles in architectural documentation and 3D modeling studies is becoming increasingly widespread. When the studies in the literature are examined, it is seen that they focus on the documentation and 3D modeling of historical buildings. In this study, unlike the research in the literature, the usability of UAV photogrammetry in architectural project implementation and monitoring is investigated. In line with this aim, 3D point clouds and 3D models were generated using UAV photos in the study. For the identified reference points, measurements obtained from architectural project drawings, measurements taken on-site using the measurement technique with a laser meter, and finally the comparison of the measurements corresponding to these reference points on the 3D model produced from UAV photos were conducted. Based on the obtained data, when the detailed measurements taken with a laser meter are compared with the detailed measurements taken from the 3D model obtained with UAV, the consistency level is observed to be an average of 98% and above. Thus, the accuracy of the measurements obtained using UAV photogrammetry has been proven. Additionally, it was observed that measurements taken with a laser meter from the same reference points on the architectural project were different. The reason for this is the modification of the forms of details in the implementation phase of the architectural project. In this regard, it is thought that obtaining precise measurements on photos taken with UAV photogrammetry will provide an important groundwork for future studies on architectural project implementation and monitoring.

**Keywords:** Photogrammetry, UAV, point cloud, 3D model, building survey.

## MİMARİ PROJE UYGULAMALARININ FOTOGRAMETRİK NOKTA BULUTU İLE İNCELENMESİ: İĞDIR ÜNİVERSİTESİ CAMİİ ÖRNEĞİ

### Özet

Orijinal bilimsel makale

Günümüz teknolojisindeki yaşanan gelişmelere bağlı olarak mimari belgeleme ve 3B modelleme çalışmalarında insansız hava araçlarının kullanımı gün geçtikçe yaygınlaşmaktadır. Literatürdeki çalışmalar incelendiğinde tarihi yapıların belgelenmesi ve 3B modellenmesi konuları üzerine yoğunlaşdığı görülmektedir. Bu çalışmada literatürdeki araştırmalardan farklı olarak İHA fotogrametrisinin mimari proje uygulama ve takibinde kullanılabilirliği araştırılmıştır. Çalışmada bu amaç doğrultusunda İHA fotoğrafları kullanılarak 3B nokta bulutu ve 3B model üretilmiştir. Belirlenen referans noktalar için; Mimari proje çizimlerinden elde edilen veriler ile lazer metre kullanılarak yerinde ölçüm tekniği ile alınan ölçüler ve son olarak da İHA fotoğraflarından üretilen 3B model üzerindeki bu referans noktalarına karşılık gelen ölçülerin karşılaştırılması yapılmıştır. Elde edilen veriler doğrultusunda lazer metre ile alınan detay ölçümlerinin, İHA ile elde edilen 3B model üzerinden alınan detay ölçüleri ile kıyaslandığında tutarlılık derecesinin ortalama %98 ve üzerinde olduğu gözlemlenmiştir. Bu sayede İHA fotogrametrisi kullanılarak elde edilen ölçülerin hassasiyeti kanıtlanmıştır. Ayrıca lazer metre ile mimari proje üzerindeki aynı referans noktalarından alınan ölçülerin farklı olduğu tespit edilmiştir. Bunun nedeni ise mimari projedeki detayların uygulama aşamasında formlarının değiştirilmesidir. Bu doğrultuda İHA Fotogrametrisi ile çekilen fotoğraflar üzerinde yapılabilecek hassas ölçümlerin elde edilmesi gelecekte yapılacak mimari proje uygulama ve takibine yönelik çalışmalara önemli bir altlık oluşturulacağı düşünülmektedir.

**Anahtar Kelimeler:** Fotogrametri, İHA, nokta bulutu, 3B model, röleve.

### 1 Introduction

The efforts to achieve accurate and precise data in documentation and 3D modeling studies in architecture

have led to the emergence of new methods and techniques. Due to advancements in today's technology, these methods and techniques continue to evolve, and their

\*Corresponding author.

E-mail address: selim.kartal@igdir.edu.tr (S. Kartal)

Received 14 December 2023; Received in revised form 11 March 2024; Accepted 22 April 2024

2587-1943 | © 2024 IJIEA. All rights reserved.

Doi: <https://doi.org/10.46460/ijiea.1404705>

applications are becoming increasingly widespread. One of these modern techniques is Photogrammetry.

Photogrammetry, generally, refers to the scientific discipline of making precise measurements of the relative positions of points by utilizing data obtained from images and other information sources. This allows for accurate determination of properties such as distances, angles, areas, volumes, elevations, dimensions, and shapes of objects [1]. Furthermore, it is possible to create a three-dimensional (3D) model from detailed two-dimensional (2D) photographs of objects.

The photogrammetry method makes a significant contribution by providing texture data, which includes surface features, in addition to the fundamental three-dimensional data of objects. These texture data are combined with the geometric properties of three-dimensional objects to align with metric features. Since these textures are obtained from the objects' own photographs, more realistic models are produced. This ensures that objects appear in a detailed and realistic manner, similar to their appearance in the real World [2]. Additionally, the photogrammetric method;

- Obtaining the desired format of the product depending on the use of technological equipment,
- Significantly reducing processing time compared to conventional methods,
- Providing superiority in accuracy of evaluation compared to other approaches,
- Having data in digital format,
- Gaining advantages over traditional methods, such as the ability to be linked to the country coordinate system, for various reasons [3].

The advantages of photogrammetric technique over classical methods highlight it among other methods and contribute to its widespread use. This technique, whose usage is increasingly expanding, is divided into terrestrial and aerial photogrammetry based on the location of the photographing point

Terrestrial Photogrammetry refers to a technique carried out with photographs taken from fixed points on the Earth's surface, while Aerial Photogrammetry is defined as a technique where photographs are taken from the air to cover extensive areas that cannot be reached by terrestrial shooting techniques. [4]. Initially based on images taken from the ground, photogrammetry later expanded its field of view by moving the capture point to the air, becoming a significant method for creating plans and maps [5].

Aerial photogrammetry, despite undergoing different stages of development over time, is currently most commonly performed using Unmanned Aerial Vehicles (UAV). UAV photogrammetry is a method carried out using UAV or drones. Cameras on the UAV platform enable unmanned aerial vehicles to autonomously or manually perform the task of capturing photographs from a specific altitude. This has significantly reduced time and workload without the need for a large working team, allowing for the rapid attainment of the most accurate results. UAV photogrammetry is extensively used in architectural studies, as in many engineering fields.

In the field of architecture, UAV photogrammetry is a technology used for detailed measurement and digital 3D modeling of architectural structures. Photogrammetry is commonly employed in architecture, not only for modeling historical buildings but also effectively for post-construction measurement and analysis of modern structures. This method allows for the documentation and analysis of architectural projects to be carried out more quickly compared to traditional methods.

Both terrestrial photogrammetry and aerial photogrammetry have been widely used in recent years in the field of architecture for the preparation of survey projects and documentation of historical structures. In the literature, there are numerous studies documenting cultural heritage and creating 3D models using photogrammetric techniques (Erdoğan [6]; Asri and Çorumluoğlu [7]; Asri and Çorumluoğlu [8]; Maraş et al. [9]; Marangoz and Özen [10]; Şasi [11]; Polat et al. [12]; Zeybek and Kaya [13]; Erdoğan et al. [14]; Şenol and Orman [15]; Döş and Yiğit [16]; Kabadayı and Erdoğan [17]; Karataş [18]; Yıldırım Demir and Yaman [19]; Susam [20]). In these studies, applications have been carried out for ruins, mosques, small mosques, museums, churches, tombs, fountains, bridges, city walls, pulpits, mansions, and historical settlements. In addition to these, archaeological artifacts such as historical sculptures and tombstones have also been 3D modeled and documented.

In the literature, research generally focuses on documenting and 3D modeling historical heritage. In contrast, this study investigates the usability of UAV photogrammetry in the implementation and monitoring of architectural projects. In pursuit of this goal, 3D point clouds and models were generated using UAV photos. For the identified reference points, measurements obtained from architectural project drawings, measurements taken on-site using a laser meter, and finally, a comparison of the measurements of these reference points on the 3D model produced from UAV photos were conducted. This allowed for an analysis of the accuracy and precision of the measurements obtained through UAV photogrammetry. In this regard, achieving precise measurements on UAV photogrammetry images is believed to provide a significant foundation for future studies focusing on the implementation and monitoring of architectural projects.

## 2 Material and Method

### 2.1 The Case Study

The study involved the application on a mosque located at Iğdır University Şehit Bülent Yurtseven Campus (Figure 1). The mosque, with a capacity of 3000 people and a construction area of 1600 m<sup>2</sup>, includes 2 minarets with a height of 50 m each, one large dome with a height of 26 m, and 5 small domes. The construction of this mosque, characterized by a highly modern and aesthetic architectural concept, began in 2014 and was completed in 2017.

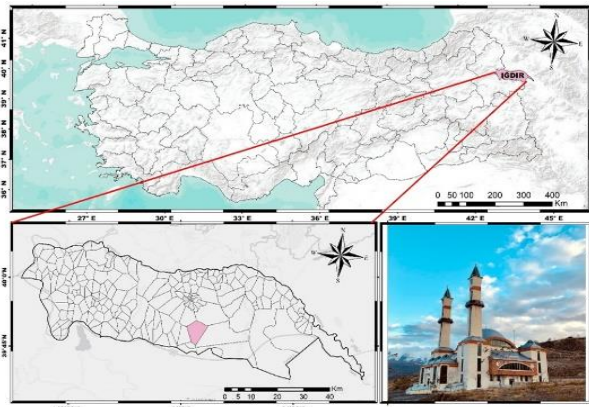


Figure 1. Working area (39.0811423,44.0080929).

## 2.2 Obtaining Data (Field Study)

The data acquisition process in the study consists of three stages. First, the length measurements of the sections to be compared were taken from the architectural implementation project shown in Figure 2. In the second stage, corresponding to the lengths obtained in the first stage, measurements of the existing state of the structure were taken using a laser meter, as depicted in Figure 3. In the final stage, photos of the mosque were captured using the DJI Phantom 4 RTK Unmanned Aerial Vehicle (UAV) (Figure 4), through a versatile (multi-oriented) flight performed at a height of 60 m. The technical specifications of the UAV used in the photo shoot are provided in Table 1.

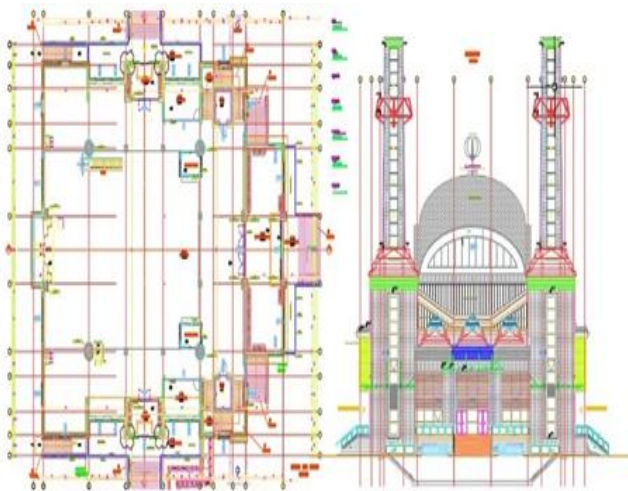


Figure 2. Architectural application project.



Figure 3. Kl pro laser meter.



Figure 4. Dji phantom 4 rtk drone.

Table 1. Technical specifications of the unmanned aerial vehicle.

DRONE BODY	
Takeoff Weight	1391 gr
Cross Length	350 mm
Maximum Altitude	Operating 19685 ft
Maximum Ascension Speed	6 m / s (automatic flight); 5 m / s (manual control)
Maximum Descent Speed	3 m/s
Maximum Speed	31 mph (50 kph) (P-mode)
Maximum Flight Time	Approximately 30 min
Operating temperature range	32 °C
Operating frequency	2.400 GHz- 2.483 GHz (Europe, Japan, Korea) 5.725 GHz- 5.850 GHz (United States, China)
Accuracy Range	RTK is active and working properly: Vertical: ±0.1 horizontal: ±0.1 m RTK off Vertical: ±0.1 m (vision positioning); ±0.5m (GNSS positioning) Horizontal: ±0.3m (Vision positioning); ±1.5 m (GNSS positioning)
CAMERA	
Sensor	FOV 84°; 8.8mm / 24mm (35mm format equivalent: 24mm);
Lens	FOV 84°; 8.8mm / 24mm (35mm format equivalent: 24mm); f/2.8- f/11, autofocus, 1 m
Image Size Maximum	4864×3648(4:3);
photo format	JPEG
BATTERY	
Capacity	5870 mAh
Voltage	15.2 V
Weight	468

## 2.3 Processing of Data (Office Work)

After the fieldwork was completed, 496 photos taken with the UAV were input into the demo version of the DJI Terra software (Figure 5), and point cloud, Digital Surface Model (DSM), and 3D model results for the mosque were obtained. Subsequently, reference measurements from the architectural implementation project were displayed on the model. Later, measurements taken with a laser meter from the same reference points were processed onto the model.

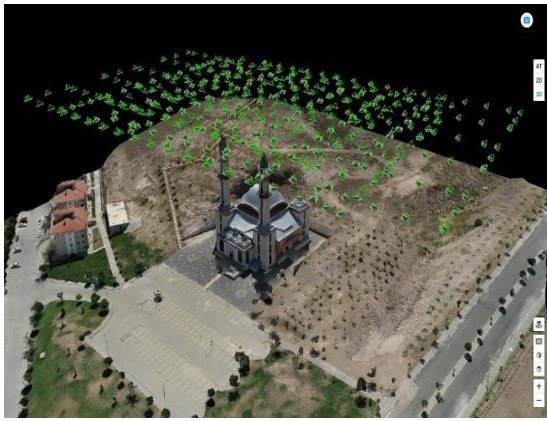


Figure 5. Photography shooting points.



Figure 8. 3D model view.

### 3 Findings

The photos taken with the UAV were processed in DJI Terra software, resulting in a point cloud (Figure 6), DSM (Figure 7), and 3D model (Figure 8). Measurements taken from the reference points on the generated 3D model were compared with measurements taken with a laser meter and the length measurements from the architectural implementation project (Figures 9-11). All three measurement values are presented in Table 2. In this table, values measured with the laser meter are considered as the exact measurement values. Additionally, in Table 2, L1 represents the difference between the exact measurement and the length in the architectural project, while L2 represents the difference between the exact measurement and the length of the same detail on the 3D model.

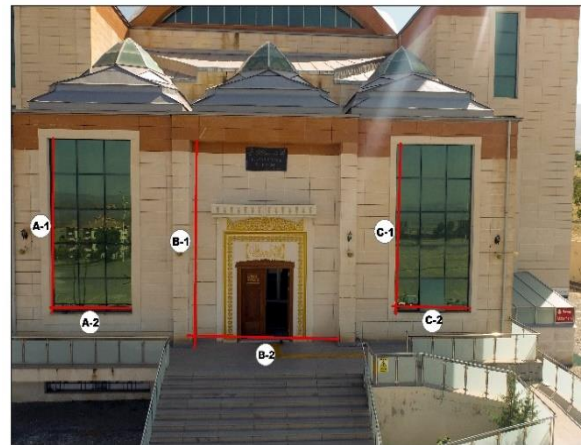


Figure 9. North front reference points.

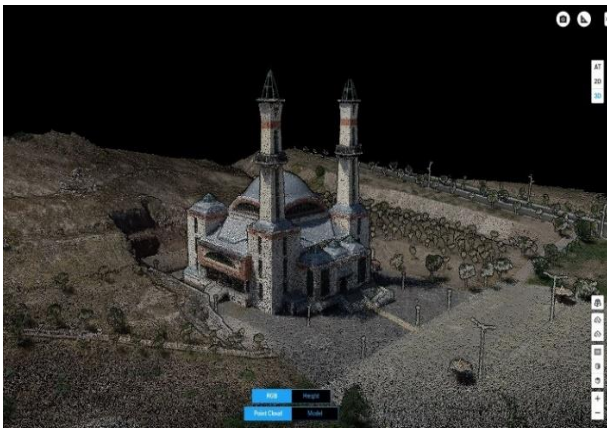


Figure 6. Point cloud view.



Figure 10. South front reference points.

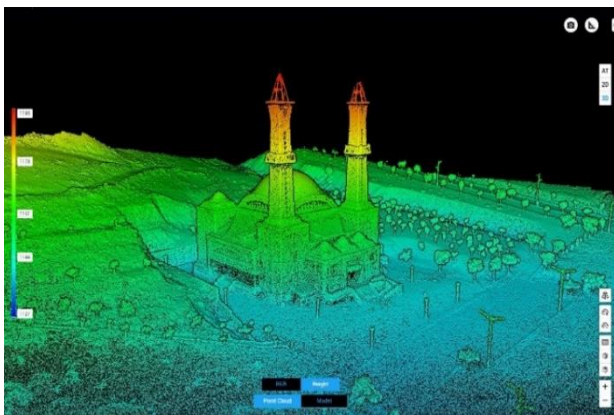


Figure 7. Dsm view.

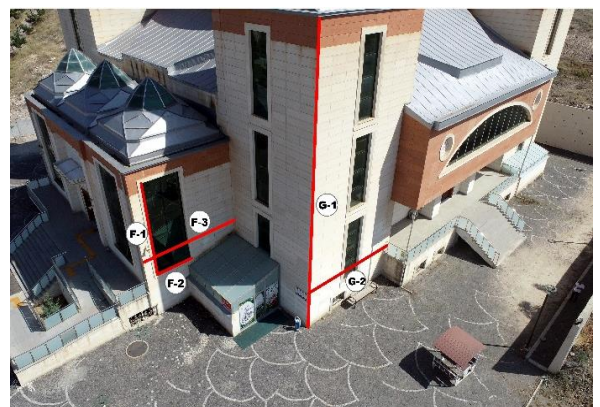


Figure 11. West front reference points.

**Table 2.** Comparison of reference point measurements.

Facade/Detail		MEASUREMENT VALUES			GAP	
		Lazer Metre (m)	Architectural Project (m)	3D Model (m)	L <sub>1</sub> (m)	L <sub>2</sub> (m)
Front Facade	A-1	5.83	5.88	5.86	0.05	0.03
	A-2	3.06	4.63	3.03	<b>1.57</b>	0.03
	B-1	6.90	5.89	6.80	1.01	<b>0.10</b>
	B-2	5.72	5.45	5.78	0.27	0.06
	C-1	5.82	5.96	5.82	0.14	0.00
	C-2	3.08	4.63	3.09	1.55	0.01
Back Elavation	D-1	3.96	***	3.92	-	0.04
	D-2	1.31	1.45	1.27	0.14	0.04
	E-1	10.10	9.97	10.05	0.13	0.05
	E-2	6.93	7.09	6.92	0.16	0.01
	E-3	1.84	1.56	1.87	0.28	0.03
Side (Right) Elavation	F-1	5.87	5.89	5.89	0.02	0.02
	F-2	2.39	3.20	2.40	0.81	0.01
	F-3	6.70	6.61	6.67	0.09	0.03
	G-1	16.72	16.72	16.74	0.00	0.02
	G-2	7.65	7.71	7.64	0.06	0.01

\*Due to the differences in form between the architectural project and the implementation, measurement values could not be taken.

In Table 2, detailed measurements for 16 points on three different facades of the mosque located at Iğdır University Suveren Campus are provided. When examining the differences in detailed measurements taken with a laser meter on the 3D model, it is observed that the maximum difference is  $\pm 10$  cm. In detail C-1, the measurements taken with a laser meter on the 3D model were found to match exactly. Based on the obtained data, the consistency degree of detailed measurements taken with a laser meter compared to detailed measurements taken from the 3D model obtained with UAV is observed to be an average of 98% and above. Additionally, it was found that measurements taken with a laser meter from the same reference points on the architectural project were sometimes different. Especially when detail A-2 is examined, a length difference of 1.57 m is observed. The reason for such significant differences is the construction of details in the architectural project at different dimensions during the implementation phase. Furthermore, the measurement value for detail D-1 could not be obtained as it was not consistent with the architectural Project.

#### 4 Results

The regularly captured images with UAV photogrammetry during the construction stages of architectural projects can be used to monitor and supervise the construction progress, assess potential issues early, and ensure compliance with the project. Photogrammetry has become a significant tool in the field of architecture, offering advantages such as providing precise measurements, supporting detailed modeling, and aiding conservation efforts.

This technique provides the opportunity to obtain faster, more effective, and more detailed information compared to traditional measurement and documentation

methods. In this study, various detail measurements were taken on three different facades of the mosque located at Iğdır University Suveren Campus. Evaluation of these measurements indicates that UAV photogrammetry provides information about the adherence of the construction process and post-construction to the architectural projects, as well as the accuracy of the constructed forms. Particularly, the precise detection of differences between architectural projects and the actual construction during the construction process demonstrates the effective use of UAV in such scenarios.

#### Declaration

Ethics committee approval is not required.

#### References

- [1] DeWitt, B.A., & Wolf, P.R. (2000). Elements of Photogrammetry (with Applications in GIS), 3rd ed.; McGraw-Hill Higher Education: New York, NY, USA.
- [2] Ulvi, A., & Yiğit, A. (2019). Kültürel Mirasın Dijital Dokümantasyonu: Taşkent Sultan Çeşmesinin Fotogrametrik Teknikler Kullanarak 3B Modelinin Yapılması. *Türkiye Fotogrametri Dergisi*, 1(1), 1-6.
- [3] Yakar, M., Yıldız, F., & Yılmaz, H. (2005 Mart-Nisan). Tarihi ve Kültürel Mirasların Belgelenmesinde Jeodezi Fotogrametri Mühendislerinin Rolü. *TMMOB Harita ve Kadastro Mühendisleri Odası 10. Türkiye Harita Bilimsel ve Teknik Kurultayı*, Ankara.
- [4] Gençerk, E.Y. (2016). *İnsansız hava aracı fotogrametrisi uygulaması ile inşaat projesi imalat durumunun araştırılması* (Master's Dissertation, Bilkent University).
- [5] Atay, H. (2002). *İnsan Vücudunun Fotogrametrik Yöntemle Modellenmesi* (Doctoral dissertation, İstanbul Technical University Institute of Science).
- [6] Erdoğan, C. (2005 Kasım). Tarihi Çeşmelerin Dijital Fotogrametrik Yöntemle Rölövelerinin Hazırlanması. *Harita ve Kadastro Mühendisleri Odası, Mühendislik Ölçmeleri STB Komisyonu 2. Mühendislik Ölçmeleri Sempozyumu 23-25 Kasım 2005, İTÜ – İstanbul*.
- [7] Asri, İ., & Çorumluoğlu, Ö. (2007). Büyük Objelerde Tarihi Dokümantasyon ve Tanıtım Amaçlı GPS Destekli Dijital Fotogrametrik 3B Modelleme. *TUFUAB IV. Teknik Sempozyumu, İstanbul*.
- [8] Asri, İ., & Çorumluoğlu, Ö. (2014). Tarihi Yerleşim Alanlarının Yersel Fotogrametri Yöntemi ile 3B Modellenmesi: Santa-Harabeleri Örneği. *Uzaktan Algılama-CBS Sempozyumu, İstanbul*.
- [9] Maraş, E., Hacıfendioğlu, K., Birinci, F., & Uslu, G. (2016). Tarihi Köprülerin Dokümantasyonu İçin Dijital Fotogrametri ile 3B Modellerinin Oluşturulması ve Dinamik Analizlerinin Yapılması (Tarihi Kurt Köprüsü Örneği). *Harita Dergisi*, 155, 1-11.
- [10] Marangoz, A., & Özen, M. (2020). Tarihi Yerleşim Alanlarının Yersel Fotogrametrik Yöntem ile 3B Modellenmesi: Zeynel Bey Türbesi Örneği. *Türkiye Fotogrametri Dergisi*, 2(1), 1-6.
- [11] Şasi, A. (2020). Kültürel Mirasların İnsansız Hava Aracı ile Fotogrametrik Üç Boyutlu Modelleme Çalışmalarında Karşılaşılan Sıkıntılar ve Öneriler. *Türkiye Fotogrametri Dergisi*, 2(1), 7-13.
- [12] Polat, N., Önal, M., Ernst, F.B., Şenol, H.I., Memduhoğlu, A., Mutlu, S., Mutlu, S.İ., Budan, M.A., Turgut, M., & Kara, H. (2020). Harran Ören Yeri Arkeolojik Kazı Alanınının Çıkarılan Bazı Küçük Arkeolojik Buluntuların Fotogrametrik Olarak 3B Modellenmesi. *Türkiye Fotogrametri Dergisi*, 2(2), 55-59.

- [13] Zeybek, M., & Kaya, A. (2020). Tarihi Yiğma Kiliselerde Hasarların Fotogrametrik Ölçme Tekniğiyle İncelenmesi: Artvin Tbeti Kilisesi Örneği. *Geomatik*, 5(1), 47-57.
- [14] Erdoğan, A., Kabadayı, A., & Akın E.S. (2021). Kültürel Mirasın Fotogrametrik Yöntemle 3B Modellenmesi: Karabıyık Köprüsü Örneği. *Türkiye İnsansız Hava Araçları Dergisi*, 3(1), 23-27.
- [15] Şenol, H.İ., & Orman, E. (2022). Diyarbakır Mardin Kapı'nın Yersel Fotogrametri Yöntemiyle 3B Belgelenmesi. *Türkiye Fotogrametri Dergisi*, 4(1), 01-06.
- [16] Döş, M., & Yiğit, A.Y. (2022). Tarihi minberlerin fotogrametri yöntemi ile belgelenmesi. *Türkiye Fotogrametri Dergisi*, 4(2), 58-65.
- [17] Kabadayı, A., & Erdoğan, A. (2023). İHA Fotogrametrisi Kullanarak Yozgat Çilekçi Türbesi'nin 3 Boyutlu Nokta Bulutu ve Modelinin Üretilmesi. *Türkiye Fotogrametri Dergisi*, 5(1), 29-35.
- [18] Karataş, L. (2023). Yersel lazer tarama yöntemi ve ortofotoların kullanımı ile kültür varlıklarının cephelerindeki malzeme bozulmalarının dokümantasyonu: Mardin Mungan Konağı örneği. *Geomatik*, 8(2), 152-162.
- [19] Yıldırım Demir, P., & Yaman, A. (2024). Hasas Baba Türbesi'nin Fotogrametrik Rölöve Alımı ve Farklı Yazılımlarda Doğruluk Araştırması. *Fırat Üniversitesi Mühendislik Bilimleri Dergisi*, 36(1), 11-23.
- [20] Susam, T. (2019). Topographical Analyses of Unmanned Aerial Vehicle-Based Very High-Resolution Digital Surface Models for Archaeological Sites. *Tehnički vjesnik*, 26(1), 236-242.



## INVESTIGATION OF THE EFFECTS OF SMAW PARAMETERS AND SEAWATER TEMPERATURE ON PROPERTIES OF AH36 JOINTS AND THE CHEMICAL COMPOSITION OF SEAWATER

Emre Görgün\*<sup>1</sup> 

<sup>1</sup>Sivas Cumhuriyet University, Sivas Technical Sciences Vocational School, Railway Systems Department, 58104 Sivas, Turkey

### Abstract

Original scientific paper

Underwater wet welding (UWW) is a critical technique for repairing offshore structures, underwater pipelines, water transport infrastructure, docks, and harbor equipment. In this study, the mechanical and microstructural properties of AH36 low-carbon steel weldments were investigated using metal arc welding (SMAW), an underwater wet welding method, at various welding current strengths and seawater temperatures. The relationship between changes in seawater temperature and welding current parameters and their impact on seasonal variations in welding conditions and seawater composition was examined. In the first stage, the yield strength of AH36 was statistically modeled using a central composite design with input parameters of seawater temperature (ranging from 9.7 °C to 25.3 °C) and weld current value (ranging from 49A to 90A). Optimal conditions were determined, resulting in a yield strength of 270MPa, achieved at a seawater temperature of 17.5 °C and a weld current value of 69.5 A. In the second stage, data from optimization studies were utilized to develop elemental exchange equations for Cr ( $R^2=87.3$ ), Ni ( $R^2=64.45$ ), and Mn ( $R^2=65.74$ ) ions in seawater. The findings reveal that weld current intensity primarily influences changes in Cr content in seawater, seawater temperature is correlated with Ni content, and both current intensity and seawater temperature affect the Mn content. The analytical techniques employed include Inductively Coupled Plasma Mass Spectrometry (ICP-MS) for seawater ion analysis, Energy Dispersive Spectroscopy (EDS) point analysis to determine the chemical composition of AH36, and Scanning Electron Microscopy (SEM) for microstructural analysis.

**Keywords:** Response surface method (RSM), steel plate A36, stick metal arc welding (SMAW), underwater wet welding (UWW), welding current.

## SMAW PARAMETRELERİNİN AH36 BAĞLANTI ÖZELLİKLERİNE VE DENİZ SUYUNUN KİMYASAL BİLEŞİMİNE ETKİSİNİN ARAŞTIRILMASI

### Özet

Orijinal bilimsel makale

Sualtı kaynağı (SMAW) açık deniz yapılarının, sualtı boru hatlarının, su taşımacılığı altyapısının, rıhtımların ve liman ekipmanlarının onarımı için kritik bir tekniktir. Bu çalışmada, bir sualtı kaynak yöntemi olan metal ark kaynağı (SMAW) kullanılarak AH36 düşük karbonlu çelik kaynakların mekanik ve mikroyapısal özellikleri çeşitli kaynak akım şiddetleri ve deniz suyu sıcaklıklarında incelenmiştir. Deniz suyu sıcaklığı ve kaynak akımı parametrelerindeki değişimler arasındaki ilişki ve bunların kaynak koşulları ve deniz suyu bileşimindeki mevsimsel değişimler üzerindeki etkisi incelenmiştir. İlk aşamada, AH36'nın akma dayanımı, deniz suyu sıcaklığı (9,7 °C ila 25,3 °C arasında değişen) ve kaynak akımı değeri (49A ila 90A arasında değişen) girdi parametreleri ile merkezi bir kompozit tasarım kullanılarak istatistiksel olarak modellenmiştir. Optimum koşullar belirlenmiş ve 17,5 °C deniz suyu sıcaklığı ve 69,5 A kaynak akımı değerinde 270 MPa akma dayanımı elde edilmiştir. İkinci aşamada, optimizasyon çalışmalarından elde edilen veriler deniz suyundaki Cr ( $R^2=87,3$ ), Ni ( $R^2=64,45$ ) ve Mn ( $R^2=65,74$ ) iyonları için element değişim denklemleri geliştirmek için kullanılmıştır. Bulgular, kaynak akım yoğunluğunun öncelikle deniz suyundaki Cr içeriğindeki değişiklikleri etkilediğini, deniz suyu sıcaklığının Ni içeriği ile ilişkili olduğunu ve hem akım yoğunluğunun hem de deniz suyu sıcaklığının Mn içeriğini etkilediğini ortaya koymaktadır. Kullanılan analitik teknikler arasında deniz suyu iyon analizi için İndüktif Eşleşmiş Plazma Kütle Spektrometrisi (ICP-MS), AH36'nın kimyasal bileşimini belirlemek için Enerji Dağılımlı Spektroskopisi (EDS) nokta analizi ve mikroyapısal analiz için Taramalı Elektron Mikroskopu (SEM) bulunmaktadır.

**Anahtar Kelimeler:** Yanıt yüzey yöntemi (RSM), A36 çelik levha, çubuk metal ark kaynağı (SMAW), sualtı kaynak (UWW), kaynak akımı.

\*Corresponding author.

E-mail address: emregorgun@cumhuriyet.edu.tr (E. Görgün)

Received 12 January 2024; Received in revised form 15 April 2024; Accepted 19 April 2024

2587-1943 | © 2024 IJIEA. All rights reserved.

Doi: <https://doi.org/10.46460/ijiea.1418641>

## 1 Introduction

Underwater wet welding (UWW) technology has gained widespread recognition owing to its real-time and on-site applications in constructing and maintaining marine structural engineering equipment, including subsea oil pipelines, marine vessel repairs, oil platforms, and offshore turbines [1, 2]. The simplicity of this technology in equipment utilization allows for cost-effective maintenance of complex-shaped structures [3-5]. While shielded metal arc welding (SMAW) remains in use, recent research has shown a growing focus on flux-cored arc welding (FCAW) within the realm of UWW [6-8]. Solid-state friction stir welding has the potential to successfully join steel plates [9-15]. However, it has some shortcomings, such as the requirement of a stirring tool with high-temperature resistance and geometrical limitations. Thus, conventional fusion welding methods, i.e. gas metal arc welding and gas tungsten arc welding, are the most common welding processes used for joining steel parts including stainless steels in various industries [16, 22]. However, these gas shielded arc welding methods cannot be used in under seawater applications. Shielded metal arc welding is particularly valuable for repairing welds that are paramount in deep-water environments [23, 24]. With urbanization and industrialization, industrial chemicals, rare earth elements, platinum group elements (PGE), and radionuclides are increasingly present [25]. This can significantly affect spring water quality, potentially leading to bacterial and pathogenic contamination [26, 27].

Underwater arc welding has been shown in recent studies to be the most suitable method for carrying out repairs and constructing underwater structures. [28]. Nevertheless, several challenges arise when testing welds performed underwater [29]. Among the major difficulties encountered is the rapid contact between the workpiece and water, resulting in a pronounced quenching effect [30]. Hydrogen diffusion occurs due to the dissociation of water, leading to hydrogen-induced cracking, which has been observed to reduce fatigue strength [31]. Arc instability, porosity and loss of alloying elements in welds caused by the presence of infused gases contribute to the deterioration of the mechanical properties and microstructure of the weld metal [32]. In addition, the heat-affected zone (HAZ) is subjected to increased hardness, which can lead to cracking [33]. In order to obtain the required properties in welds, it is recommended to implement control over the input parameters during welding, to include alloying materials in the electrode coating and to use multi-pass welding techniques [34]. There are not many studies in the literature on the environmental effects of weld parameters and their effects on seawater. The main subject of this study is to increase the welding capability and minimise the environmental impact by providing optimum conditions.

This study emphasizes that polluted surface water and groundwater can serve as pathways for various microbiological contaminants, resulting in adverse health effects in humans [35]. Consumption of contaminated drinking water can lead to waterborne diseases, such as diarrhea and gastrointestinal illnesses, responsible for numerous epidemics throughout history [36].

Most studies have discussed the effects of elements on the slag barrier of wet-flux core welding, mainly focusing on molten slag. Welding AH36 presents challenges such as thermal cracking and carbide precipitation, especially in multipass welds, which may lead to alterations in the mechanical strength. Over a century ago, observations were made in the German chrome ore industry, which showed a higher incidence of lung cancer among workers than in the general population. Subsequent investigations revealed that hexavalent chromium (Cr6+) in drinking water was the underlying cause of this elevated risk [37, 39]. Studies underscore the critical significance of Cr content in seawater [40, 41, 42].

This study investigates the environmental impact of welding parameters on seawater during maintenance, repair and manufacturing operations. Thus, it is predicted that the environmental impact of seawater temperature and welding parameters can be minimised.

## 2 Materials and Methods

### 2.1 Materials

AH36 steel emerges as a highly favored material within diverse marine sectors, particularly in shipbuilding and underwater structures. The selection of AH36 steel can be attributed to several key factors. Firstly, its high strength is paramount for underwater structures and vessels, offering resilience against water pressure, waves, and environmental stressors, thereby bolstering overall structural integrity. Secondly, its exceptional resistance to corrosion in environments like seawater and high moisture settings significantly prolongs longevity and reduces maintenance costs for underwater structures. Thirdly, AH36 steel shows remarkable toughness even in low-temperature conditions, ensuring reliability and durability in cold water operations. Lastly, its favorable welding properties make it highly suitable for underwater welding processes, facilitating repair and assembly procedures, thereby providing a crucial advantage in underwater applications.

AH36 steel plates with dimensions of 300 mm × 100 mm × 16 mm cut from rolled sheets were used as the base metals. An E7014 electrode with a diameter of 3.25 mm was used as the filler. Welding was performed in a 2000 ml seawater environment, and the chemical compositions of the base metal, filler metal, and seawater are listed in Table 1.

**Table 1.** Chemical compositions of the base metal, filler metal, and seawater.

Materials	C	Si	Mn	P	S	Al	Ti	Cu	Cr	Ni	Mo	Fe
AH36 (wt%)	0.18	0.50	0.90	0.035	0.035	0.015	0.02	0.35	0.20	0.40	0.08	Bal.
E7014 (wt%)	0.15	0.90	1.25	0.035	0.035	Bal.	Bal.	Bal.	0.20	Bal.	0.30	Bal.
Sea Water (µg/l)	-	200	0.10	40	160	0.7	-	0.5	0.10	0.50	0.10	4

## 2.2 Welding Procedure

A series of welding experiments using different welding current values and seawater temperatures, using Shielded Metal Arc Welding (SMAW) as the welding method, were conducted in this study. To perform these experiments, a welding machine with a maximum operating capacity of 350 A was used, as recommended in the literature [4]. Before commencing the welding process, all specimens were meticulously prepared. This preparation involved mechanical polishing using abrasive paper to ensure a smooth and uniform surface. Furthermore, chemical cleaning with anhydrous ethanol was conducted to eliminate any dust, oil, or other impurities that could interfere with the welding process or compromise the integrity of the resulting weld joints [3].

The sea water temperature parameters were selected according to the annual changes in sea water temperature according to the data obtained from the Turkish State Meteorological Service. Welding parameters were determined according to TS EN ISO 3834-2 Quality Requirements for Melting of Metallic Materials standard according to electrode diameter, material thickness and material type.

Welding experiments were conducted in a water tank with a water depth of 150 mm. A mechanical arm was used to manipulate the welding electrode to ensure the welding quality. The response surface method was employed to examine the influence of welding current on both the weld

and seawater. Optimization experiments using a central composite design (CCD) with the assistance of a Design Expert (13 trial versions) were conducted. Based on the model, the current values tested ranged from 49 to 90 A, and different seawater temperatures ranging from 9.7 °C to 25.3 °C were explored. Subsequently, the multi-response optimization model in MINITAB was used to analyze the concentrations of Cr, Ni, and Mn observed in seawater under optimal experimental conditions [44, 45].

## 2.3 Microstructure Characterization and Mechanical Performance Test Methods

Samples were prepared according to the EN ISO 17637 standard for visual inspection to determine surface defects and EN ISO 17636-1 standard to determine internal defects [46]. After the plates were welded, the tensile, chemical, and SEM analysis specimens were obtained using the wire-cutting manufacturing method, as shown in Fig. 1. 5 tensile specimens, 5 microscopic characterization specimens and 5 seawater specimens were taken from each test group with a total of 360 specimens for experimental studies.

Fig. 1 illustrates the test specimens' cutting plan and the geometry of tensile test specimens. All the sample areas were chosen from the same position as the weld center. To minimize the impact of random errors on experimental precision, three metallographic specimens and five tensile specimens were selected for each weld parameter [47, 48].

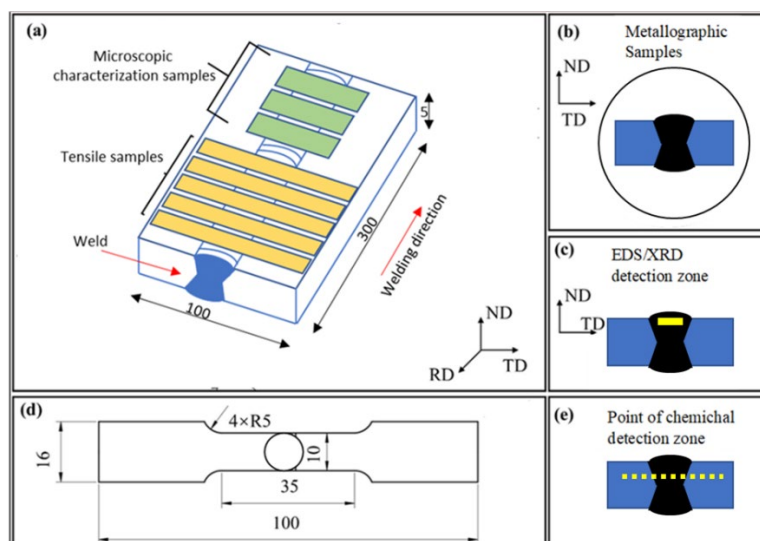


**Figure 1.** Samples of schematic illustrations of the directions and dimensions (a) location of tensile samples and microscopic characterization samples, (b) metallographic samples, (c) orientation and zone of EDS samples, (d) dimensions of tensile samples, and (e) point locations of chemical test.

To examine the microstructure of the weld metal, particularly the distribution and morphology of the austenite and ferrite phases, a metallographic microscope was employed. The microscope allows for detailed observations and analysis of the internal structure of the weld, providing insights into the arrangement and characteristics of the austenite and ferrite phases. The etching solution consisted of a mixture of hydrochloric and nitric acids.

Electron Backscatter Diffraction (EBSD) was used to analyze the grain size, boundaries, and misorientation of the ferrite and austenite phases. EBSD provides valuable information on the crystallographic properties of

materials. Scanning Electron Microscopy (SEM) was used to investigate phase composition and density. The scanning angle ranged from 10° to 80° and the scanning speed was set at 3°/min. The weld joints were characterized in three directions: rolling direction (RD), transverse direction (TD), and average direction (ND). The metallographic, EBSD, and SEM samples were obtained from the surface corresponding to the ND-TD orientation. This allows for consistent analysis and comparison of the weld microstructure and properties in a specific plane [48, 49].

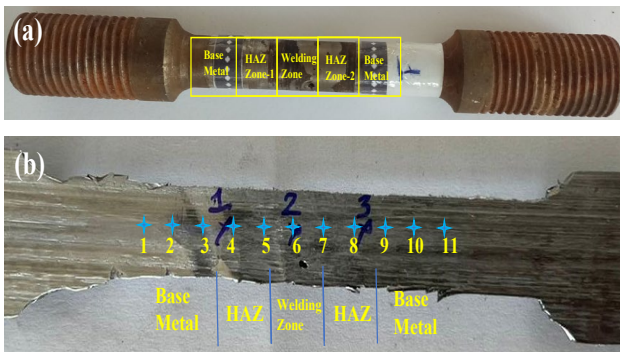


**Figure 2.** Microstructure characterization and mechanical performance samples (a) samples zones, (b) examination points.

Tensile tests were conducted using an electronic universal testing machine with a maximum load of 15 kN and tensile speed of 2 mm/min, adhering to guidelines from reference documents such as AG-50 kN. The samples were obtained from the specimens shown in Fig. 2(a). To examine the morphology of the tensile fractures, a scanning electron microscope equipped with a tungsten filament was used [56]. Detected spots were systematically distributed, starting from the base metal (BM), extending through the heat-affected zone (HAZ), and culminating at the weld metal center (WM). The spots indicated in Fig. 2(b) were used for microstructural characterization, and the interval between each spot was maintained at 2 mm.

The holes visible in Figure 2(b) are worm holes caused by hydrogen diffusion due to water segregation during welding and are considered acceptable under ISO 5817-Welding - Fusion welded joints in steel, nickel, titanium and their alloys (except beam welding) - Quality levels for defects, but the test was carried out in non-porous areas.

## 2.4 ICP-MS Performance Test Methods

The welding process was performed with a volume of 2000 ml. seawater medium and 50 ml. Samples were collected from the seawater after each welding. After opening the lids of the containers cooled at room temperature for ICP-MS analysis, the solutions dissolved in Teflon were taken into 50 ml balloon jugs [50, 51]. Dilution was performed by adding 50 ml of ultra-distilled water to the solution, and the samples were placed in plastic tubes. The samples were filtered through 25/0.45  $\mu\text{m}$  filters and stored in a refrigerator at +4  $^{\circ}\text{C}$  until reading. To prevent metal contamination, all the materials used during the dissolution of the samples were passed through  $\text{HNO}_3$  (1:1) and ultra-distilled water (1/9). An Agilent 7700 series ICP-MS device was used for heavy metal analyses. The study observed the relationship between the variation in Cr and Ni values in seawater and the weld parameters, and meaningful relationships were established [52].

$\text{Cr}^{3+}$  is a micronutrient and an essential nutritional supplement, while  $\text{Cr}^{6+}$  is highly toxic to human health. Chromium is an outstanding element in which different species exhibit contrasting behavioral characteristics towards human health (Fig. 6(b)). Cr exists in various oxidation states, from  $\text{Cr}^0$  to  $\text{Cr}^{6+}$ . While  $\text{Cr}^{6+}$  is often a by-product of industrial contamination, it can also occur

naturally in groundwater, depending on the local aquifer geology and water chemistry. This is also necessary to meet regulations in some instances; for example, the allowable limit for  $\text{Cr}^{6+}$  in drinking water is 100 ng/ml, as stipulated by the US EPA, whereas the recommended target for  $\text{Cr}^{6+}$  by California Public is 0.06 ng/ml [53, 54]. In a recent study conducted by [55], the assessment of environmental risk associated with certain heavy metals, including As, Pb, Cu, Cr, Zn, Mn, Ni, V, Al, and Fe, in the water and sediments of the Bahr El-Baqar drainage was examined. This study emphasized that the ratios of these elements in seawater are essential for evaluating their potential environmental impact.

Among the elements analyzed in this study, Mn, Fe, Cr, Al, and Cu, which have critical importance regarding their effects on the environment and human health, were the focus [56]. To weld in the seawater under different welding conditions, the focus was on establishing a relationship between the presence or absence of elements passing from the welding electrode and the base material into the seawater; thus, trying to find an optimum welding temperature and its effect on seawater was also included in the analysis.

## 2.5 Multi-Response Optimization Methods

The Response Surface Method (RSM) is a computer-aided mathematical modeling approach distinct from classical optimization methods (REF). This study employed it to identify the optimal experimental outcomes, contingent upon varying the experimental input parameters through the optimization of the experimental conditions. To facilitate this process, the Design Expert 13.00 software package was utilized to ascertain the experiments to be conducted, and the obtained results were subsequently integrated into the program.

RSM combines statistical techniques with mathematical expressions to address problems involving multiple variables. This methodology is widely applicable in various domains, including product formulation, design enhancement, and process development. Central Composite Design (CCD) is an experimental technique used to assess the effects of multiple variables and their interactions. It aims to optimize systems by understanding the impact of different factors on system responses, with applications in various fields such as industrial processes and pharmaceuticals. To accommodate this method, independent variables are scaled to vary between -1 and +1, with the smallest value denoted as -1 and the largest as +1, whereas the midpoint is established as 0. A central composite design encompasses cube points at the corners of a cube, star points outside the cube, and center points at the origin, all of which fall within the -1 to +1 range. The following equation can be mathematically expressed:

$$Y = \beta_0 + \sum(\beta_i X_i) + \sum(\beta_{ii} X_{ii}^2) + \sum(\beta_{ij} X_i X_j) \quad (1)$$

(i=1,2,3,...n)

where Y is the estimated response variable, n is the number of observations, i and j are linear and quadratic dependent and independent coefficients, respectively,  $\beta_0$  is the constant coefficient,  $\beta_i$  is the linear coefficient,  $\beta_{ii}$  is the interactive coefficient, and  $\beta_{ij}$  is the quadratic

coefficient. In this study, the response variable Y, Yield strength, X1; seawater temperature X2, and spring flow intensity were applied to the model.

### 3 Results and Discussions

#### 3.1 Microstructure and Elemental Composition

The dynamic nature of seawater composition, the difficulty of analyzing trace element concentrations in seawater with high precision, as well as factors such as environmental conditions, water currents and the general marine ecosystem can change the direct influence of the weld parameters.

Energy-dispersive X-ray spectroscopy (EDS) analysis was used to determine the separation of the Cr-Mn-rich phases. As a result of the EDS analysis, secondary phases rich in Ni, Nb, Cr, and Mo were observed in the Heat Effective Zone (HAZ) region. Fig. 3 (a)-(b).

Subsequently, EDS mapping was employed to determine the elemental distribution along the AH36 weld metal interface. The results obtained are illustrated in Fig. 3(b), (d), and (f). Based on the mapping, it was observed that the elements chromium (Cr) and manganese (Mn) were primarily distributed within the base metal AH36. This suggests that the concentrations of Cr and Mn were relatively higher in the base metal than in the weld metal in this specific analysis.

The EDS mapping analysis revealed that chromium (Cr) was predominantly concentrated within the AH36 base metal. Furthermore, a significant diffusion gradient of Cr was observed across the interface between the base metal and the weld metal. This indicates a notable change in the distribution of Cr as it diffused from the AH36 base metal into the adjacent weld metal. The Cr content of the weld metal was higher than that of the base material. This is consistent with the results of the variation in the line scan analysis. The migration of Al, Si, and S from the base metal to the weld metal affects the properties of the weld metal by changing the composition of the Cr-based filler.

According to the EDS spot analysis results shown in Fig. 3(d), these Nb-rich phases were block-shaped NbC or irregularly shaped Laves phases. The atomic compositions of 2 and 7 are shown in Fig. 3(a), and were found to fulfill the carbide characteristics, proving that carbide formation occurred in the HAZ region.

Phases suitable for A<sub>2</sub>B type (A: Ni, Cr, Fe; B: Nb, Mo, Ti) intermetallic compounds are shown in Fig. 3 (a)-(f) 2. According to Dupont, a high chromium (Cr) content tends to enhance the segregation of the Cr-rich phases. This means that when a higher concentration of Cr is present in a material, the Cr-rich phases are more likely to separate or segregate within the structure.

When the carbon content was relatively high, chromium (III) oxide (Cr<sub>2</sub>O<sub>3</sub>) precipitated. This precipitation occurs when there is an interaction between the high carbon content and the chromium present in the material. The formation of Cr<sub>2</sub>O<sub>3</sub> can affect the properties and behavior of the material. In contrast, the leaf phase was formed at a low carbon concentration. As suggested by Ramkumar, the presence of Si and Fe also contributes to the formation of the laves phase [57]. In addition, as

shown in Fig. 3(b), a block-shaped white phase rich in Cr and Mn was observed in the AH36 base metal. As shown in Fig. 3(b), the EDS spot analysis results confirmed that the 3,4,5-6 blocky phase was Cr<sub>2</sub>O<sub>3</sub>.

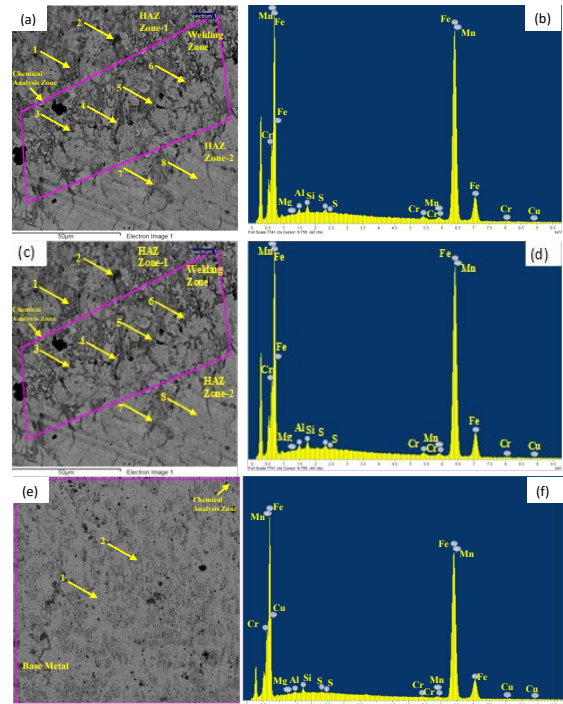


**Figure 3.** (a) The fracture morphologies of the welding zone, (b) EDS point analysis of the welding zone, (c) the fracture morphologies of the HAZ zone, (d) EDS point analysis of HAZ zone, (e) the fracture morphologies of base metal, (f) EDS analysis of base metal.

The phenomenon of chromium (Cr) and manganese (Mn) segregating at grain boundaries, resulting in relatively lower concentrations within the austenite matrix, has been consistently observed in various studies [18]. This behavior aligns with the previously discussed findings. The preferential segregation of Cr and Mn at the grain boundaries is a well-documented characteristic of specific alloy systems. This can affect the mechanical properties, corrosion resistance, and other factors of the material. Multiple investigations have documented such segregation patterns, indicating their significance in the microstructural analysis of materials containing Cr and Mn [58]. The formation of these segregated phases at the grain boundaries of the heat-affected zone can lead to grain-boundary liquefaction and produce cracks that degrade the mechanical properties and corrosion resistance of the material [43]. The same color orientations shown in Fig. 3 represent the phase distributions in the underwater wet weld Fig. 3(b) shows that most of the peaks indicated by 5 and 6 grew along the boundary line. As shown in Fig. 3(a), alloy AH36 consisted of refined grains with random grain orientations in the region indicated by number 1. The formation of twin boundaries was observed in Region 3. The fine-grained part is close to the fusion boundary, as shown in Fig. 3(b) and apparent grain growth was observed in the HAZ, as shown by number 4 in Fig. 3(c). In addition, evidence of type-II grain boundaries parallel to the fusion line is shown in Fig. 3(e). It can be seen that the C-based welds and AH36 base metal have a body centered cubic structure.

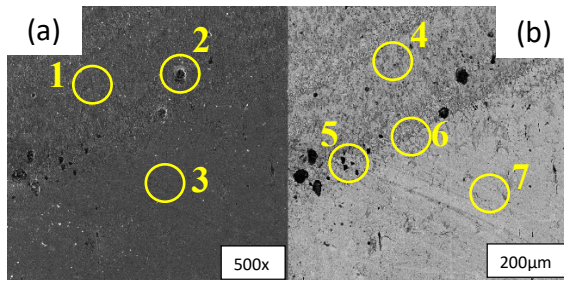


Figure 4. (a)Microstructure of welding zone 500x, (b) Microstructure of welding zone of 200µm.

The grain boundary type is closely related to the stress corrosion resistance of the grain boundaries. Typically, grain boundaries can be classified into low-angle boundaries (LABs, 2-15°) and high-angle grain boundaries (HABs, 15-180°). Fig. 4 shows that the grain boundaries in the base metal were composed of LABs and HABs, whereas very few LABs were observed in the weld zone and HAZ. This showed elemental migration from seawater to the HAZ and weld zone.

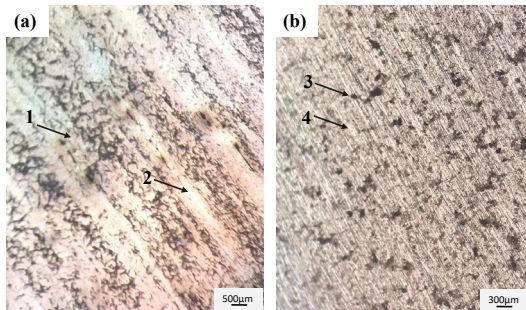


Figure 5. (a) Morphology of the HAZ zone of 500µm, (b) Morphology of the HAZ zone of 300µm.

Fig. 5 shows the microstructural characteristics of wet-welded joints. The weld metal (1) was completely austenite in structure, with equiaxed grains at the top of the welds (2) and columnar grains at the bottom of the welds (3). This phenomenon is closely related to the change in solidification mode from cellular to dendritic morphology. The solidification mode depends on the combined effects of the composition, temperature gradient, and solidification rate. The equiaxed grains in Fig. 5 (a) were observed at the ends of the welds, where the temperature gradient was shallow owing to arc extinction. Fig. 5 (b) shows the columnar grain formation due to the increased solidification rate for high-temperature gradients [32]. The direction of columnar grain growth in the carbon-based weld metal was consistent with the heat transfer direction.

### 3.2 Mechanical Performance

Compared with previous studies, grain size and inclusions were not the determining factors that improved the UTS of the weld metal (the average ultimate tensile strength). The difference solid-solution-forming elements reduce the strength of the solid- solution, primarily by reducing the resistance to the movement of dislocations, as shown in Fig. 6.

According to Roth [53] and Liang [54], the solid-solution strengthening effect owing to multiple alloying elements was determined using Equation 2, where i is the

type of solute,  $k_i$  is the hardening coefficient for solute i, and  $c_i$  is the concentration of solute I (% at.).

$$\Delta\sigma = \sum_i [k_i \sqrt{C_i}] \tag{2}$$

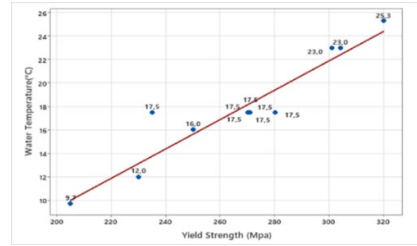


Figure 6. Multi-response optimization of water temperature and yield strength.

### 3.3 Optimisation Results with the Response Vertical Method

The RSM method modeled yield stress values obtained from tensile tests and seawater temperature, and is shown in the following equation:

$$\text{Yield Strength} = 223.164 + 5.118X_1 - 1.017X_2 + 0.053X_1 * X_2 - 0.065X_{22} - 0.034X_{22} \tag{3}$$

For the obtained equation to be compatible with the model, the three regression values expressing the model should be close to each other and have high values. In the model, predictive  $R^2$  (0,7883), adjusted  $R^2$  (0,9489), and total  $R^2$  (0,9702) were found to be high and compatible. This value shows that the yield strength obtained by the model can be predicted with an error of 2.98%, even for experiments not performed at the studied weld current intensity ( $X_1$ ) and seawater temperature ( $X_2$ ). The obtained equation shows that seawater temperature significantly affects yield strength. The presence of the interactive term  $X_1 \times X_2$  in the equation indicates that seawater temperature and weld current intensity jointly affect the yield strength of AH36.  $X_{12}$  and  $X_{22}$  in this equation indicate that a quadratic effect is possible. As a result of the modeling, two-dimensional and three-dimensional graphs were drawn for AH36 (Fig. 7a, b), relating the change in yield strength to the seawater temperature and weld current intensity.

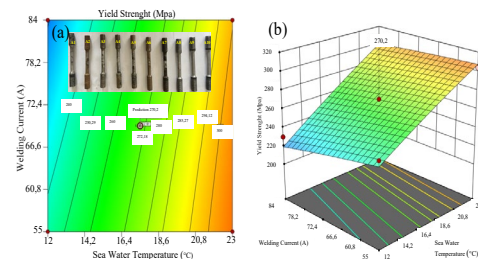
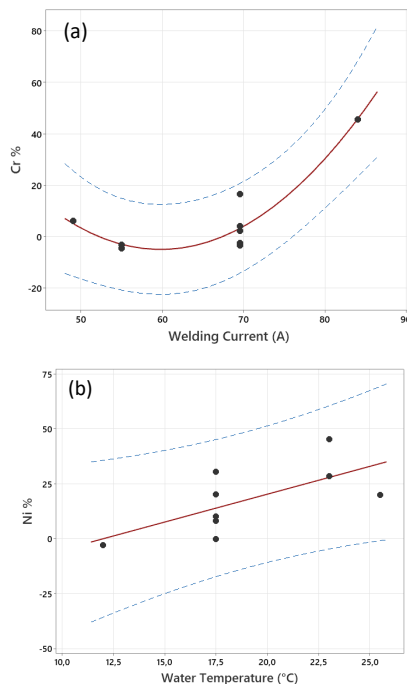


Figure 7. RSM optimization results.

### 3.4 Sea Water Elemental Composition

The P value was not measured in ICP-MS analysis and the results of this analysis are shown in Table 2. It is indicated with a negative sign. The values shown in Table 2 are unitless and represent the ratio (ppm) relative to each other.

After ICP-MS analyses were performed on the seawater samples after the weld, it was found that there was a multi-response optimization relationship with a high rate of 87.3% ( $R^2$ ) between the Cr ratio change between the weld and seawater at different weld current values. This relationship was formulated as  $Cr=304,7-10,36X_2 + 0,0866X_{22}$  multi-response optimization equation. Thus, the difference in the Cr content in seawater can be predicted to a large extent in advance using the weld current values. No relationship was found between seawater temperature and Cr content in seawater.



**Figure 8.** (a) Cr (%Wt)-Welding current relation, (b) Ni (%Wt)-Water temperature relation.

As shown in Fig. 8(a)-(b), ICP-MS analyses showed significant correlation with Cr, Ni and Mn values. ICP-MS analyses significantly correlated the Cr, Ni, and Mn values. It was observed that the changes in the Ni and Mn ratios of the weld parameters in seawater were not as highly correlated as those of Cr. It was observed that the change in the Ni ratio in seawater after welding was not related to the spring flow as in Cr, but to the change in the temperature of the seawater. However, this was a low correlation of 64.45% ( $R^2$ ). This relationship was formulated using the multi-response optimization equation  $Ni=-30.3+2.54X1$ . Unlike Cr and Ni, the change in Mn content in seawater is related to seawater temperature and welding current values, but this relationship is as low as 65.74% ( $R^2$ ). It is formulated with  $Mn=-70753+3990 X1+1095X2-58.9 X1 X2$  ( $X1$ : Welding current,  $X2$ : Water temperature).

#### 4 Conclusion

The main results of this study are as follows:

- (1) The EDS spot analysis revealed predominant distribution of chromium (Cr) and manganese (Mn) within the base metal AH36, indicating higher concentrations compared to the weld metal. A notable gradient in chromium (Cr) diffusion was observed at

the interface between the AH36 base metal and the adjacent weld metal, suggesting significant changes in distribution. Additionally, identification of Nb-rich phases through EDS analysis and the formation of chromium oxide ( $Cr_2O_3$ ) under higher carbon content provided insights into the material's behavior. The presence of a block-shaped white phase rich in Cr and Mn was confirmed in the AH36 base metal, signifying specific elemental behavior and compound formation. These findings collectively contribute to understanding the microstructure and elemental composition intricacies of AH36 material under various conditions.

- (2) A relationship between the changes in the seawater chemistry (i.e. Cr, Ni, and Mn ratios) and welding parameters was observed. The Cr ratio was directly related to the welding current, the Ni ratio was directly related to the seawater temperature, and the Mn ratio was directly associated with both the seawater temperature and welding current.
- (3) It was observed that the HAZ region of the low-carbon alloy AH36 metal had a ferrite and austenite structure and irregular distribution, and the elemental change in this region was high according to EDS point analyses. These results show that the HAZ region had the highest element diffusion into seawater after welding.
- (4) An absolute decrease in the yield strength value of AH36 metal after submarine welding was observed. The optimum yield strength was determined to be 270 MPa using RSM.
- (5) It was determined that 87.3% of the diffusion into seawater during welding depends on the welding current so that the Cr element can be controlled before the target value of 0.06 ng/ml recommended by California Public for Cr6+. Thus, a mathematical model has been developed to mitigate the environmental damage caused by Cr element.
- (6) With the findings obtained in this study, parameters such as determination of welding parameters, control of environmental impact, prediction of mechanical properties and productivity in underwater welding applications are determined. These results play an important role in improving quality, reducing environmental impact and improving efficiency in underwater welding applications.

#### Declaration

An ethics committee approval document is not required for this study.

#### References

- [1] Chen, H., Guo, N., Zhang, X., Cheng, Q., Zhou, L., & Wang, G. (2020). Effect of water flow on the microstructure, mechanical performance, and cracking susceptibility of underwater wet welded Q235 and E40 steel. *Journal of Materials Processing Technology*, 277, 116435.
- [2] Chen, H., Guo, N., Shi, X., Du, Y., Feng, J., & Wang, G. (2018). Effect of water flow on the arc stability and metal transfer in underwater flux-cored wet welding. *Journal of Manufacturing Processes*, 31, 103-115.

- [3] Klett, J., Hecht-Linowitzki, V., Grünzel, O., Schmidt, E., Maier, H. J., & Hassel, T. (2020). Effect of the water depth on the hydrogen content in SMAW wet welded joints. *SN Applied Sciences*, 2, 1-14.
- [4] Santos, V. R., Bracarense, A. Q., Pessoa, E. C. P., Marinho, R. R., Rizzo, F. C., Junior, R. C., & Monteiro, M. J. (2022). Development of oxyrutilite low alloy ferritic electrode for wet welding. *Journal of Materials Research and Technology*, 21, 1223-1247.
- [5] Santos, V. R., Bracarense, A. Q., Pessoa, E. C. P., Marinho, R. R., Rizzo, F. C., Nóbrega, A. F., ... & Rebello, J. M. A. (2021). Prediction of hydrogen cracking in the wet welding of structural steels with ferritic stick electrodes down to 20 m. *Journal of Materials Research and Technology*, 15, 5787-5802.
- [6] Putri, E. D. W. S., Surojo, E., & Budiana, E. P. (2020). Current research and recommended development on fatigue behavior of underwater welded steel. *Procedia Structural Integrity*, 27, 54-61.
- [7] Wang, J., Sun, Q., Hou, S., Zhang, T., Jin, P., & Feng, J. (2019). Dynamic control of current and voltage waveforms and droplet transfer for ultrasonic-wave-assisted underwater wet welding. *Materials & Design*, 181, 108051.
- [8] Luna, L. E. R., Bracarense, A. Q., Pessoa, E. C. P., Costa, P. S., Guerrero, G. A., & Reyes, A. E. S. (2021). Effect of the welding angle on the porosity of underwater wet welds performed in overhead position at different simulated depths. *Journal of Materials Processing Technology*, 294, 117114.
- [9] Wang, J., Sun, Q., Jiang, Y., Zhang, T., Ma, J., & Feng, J. (2018). Analysis and improvement of underwater wet welding process stability with static mechanical constraint support. *Journal of Manufacturing Processes*, 34, 238-250.
- [10] Küçükömeroğlu, T., Aktarer, S. M., & Çam, G. (2019, September). Investigation of mechanical and microstructural properties of friction stir welded dual phase (DP) steel. In IOP Conference Series: *Materials Science and Engineering* (Vol. 629, No. 1, p. 012010). IOP Publishing.
- [11] Küçükömeroğlu, T., Aktarer, S. M., İpekoğlu, G., & Çam, G. (2018). Mechanical properties of friction stir welded St 37 and St 44 steel joints. *Materials Testing*, 60(12), 1163-1170.
- [12] Çam, G. (2005). Friction stir welding (FSW)-A novel welding technology developed for Al-Alloys. *Mühendis ve Makina (Engineer and Machinery)*, 46(541), 30-39.
- [13] Ahmed, M. M., Seleman, M. M. E. S., Fydrych, D., & Gürel, Ç. A. M. (2023). Review on friction stir welding of dissimilar magnesium and aluminum alloys: Scientometric analysis and strategies for achieving high-quality joints. *Journal of Magnesium and Alloys*.
- [14] Khaliq, U. A., Muhamad, M. R., Yusof, F., Ibrahim, S., Isa, M. S. M., Chen, Z., & Çam, G. (2023). A review on friction stir butt welding of aluminum with magnesium: A new insight on joining mechanisms by interfacial enhancement. *Journal of Materials Research and Technology*.
- [15] Küçükömeroğlu, T., Aktarer, S. M., İpekoğlu, G., & Çam, G. (2018). Microstructure and mechanical properties of friction-stir welded St52 steel joints. *International Journal of Minerals, Metallurgy, and Materials*, 25, 1457-1464.
- [16] Şenol, M., & Çam, G. (2023). Investigation into microstructures and properties of AISI 430 ferritic steel butt joints fabricated by GMAW. *International Journal of Pressure Vessels and Piping*, 202, 104926.
- [17] Ezer, M. A., & Çam, G. (2022). A study on microstructure and mechanical performance of gas metal arc welded AISI 304 L joints. *Materialwissenschaft und Werkstofftechnik*, 53(9), 1043-1052.
- [18] Serindağ, H. T., & Çam, G. (2023). Characterizations of microstructure and properties of dissimilar AISI 316L/9Ni low-alloy cryogenic steel joints fabricated by gas tungsten arc welding. *Journal of Materials Engineering and Performance*, 32(15), 7039-7049.
- [19] Serindağ, H. T., Tardu, C., Kirçiçek, İ. Ö., & Çam, G. (2022). A study on microstructural and mechanical properties of gas tungsten arc welded thick cryogenic 9% Ni alloy steel butt joint. *CIRP Journal of Manufacturing Science and Technology*, 37, 1-10.
- [20] Serindağ, H. T., & Çam, G. (2021, February). Microstructure and mechanical properties of gas metal arc welded AISI 430/AISI 304 dissimilar stainless steels butt joints. In *Journal of Physics: Conference Series* (Vol. 1777, No. 1, p. 012047). IOP Publishing.
- [21] Shi, C., Cao, J., Han, S., Hu, K., Bian, L., & Yao, S. (2021). A review of polymetallic mineralization in lower Cambrian black shales in South China: Combined effects of seawater, hydrothermal fluids, and biological activity. *Palaeogeography, Palaeoclimatology, Palaeoecology*, 561, 110073.
- [22] Balaram, V., Cobia, L., Kumar, U. S., Miller, J., & Chidambaram, S. (2023). Pollution of water resources and application of ICP-MS techniques for monitoring and management—A comprehensive review. *Geosystems and Geoenvironment*, 100210.
- [23] Meng, X., Jin, X., Li, X., Chu, F., Zhu, J., Wang, Y., & Zhou, P. (2022). Seafloor mineralization related to the shallow seawater-hydrothermal circulation system in the Longqi hydrothermal field, Southwest Indian Ridge (49.6 E): Evidence from in situ trace element and sulfur isotope compositions of pyrite varieties. *Ore Geology Reviews*, 145, 104914.
- [24] Soriano, E., Pastor, A., & de la Guardia, M. (2020). Multielemental determination of trace mineral elements in seawater by dynamic reaction cell inductively coupled plasma-mass spectrometry after Al (OH) 3 coprecipitation. *Microchemical Journal*, 157, 104864.
- [25] Dey, M., Ghosh, B., & Giri, T. K. (2020). Enhanced destinal stability and pH sensitive release of quercetin in GIT through gellan gum hydrogels. *Colloids and surfaces B: Biointerfaces*, 196, 111341.
- [26] Wei, Y., Yuan, C., Xu, X., Chen, X., Ren, Z., Gui, X., ... & Cao, X. (2022). Colloid formation and facilitated chromium transport in the coastal area soil induced by freshwater and seawater alternating fluctuations. *Water Research*, 218, 118456.
- [27] Li, J., Chen, H., Liu, W., Ding, X., Zhong, R., & Yu, C. (2022). Copper mobilization via seawater-volcanic rock interactions: New experimental constraints for the formation of the iron oxide Cu-Au (IOCG) mineralization. *Geochimica et Cosmochimica Acta*, 330, 209-229.
- [28] Vashishtha, P., Wattal, R., Pandey, S., & Bhadauria, N. (2022). Problems encountered in underwater welding and remedies-a review. *Materials Today: Proceedings*, 64, 1433-1439.
- [29] Tomków, J., Landowski, M., Fydrych, D., & Rogalski, G. (2022). Underwater wet welding of S1300 ultra-high strength steel. *Marine Structures*, 81, 103120.
- [30] Li, H., Liu, S., Sun, F., Ma, Q., Ji, H., Liu, H., & Chen, H. (2022). Improvement of microstructure and mechanical properties for underwater wet 16Mn/304L dissimilar steel welded joints assisted by presetting butter layer. *Materials Today Communications*, 33, 104259.
- [31] Li, H., Liu, S., Sun, F., Yu, L., Wang, J., Wang, Z., ... & Lei, Y. (2022). Preliminary investigation on underwater wet welding of Inconel 625 alloy: microstructure, mechanical properties and corrosion resistance. *Journal of Materials Research and Technology*, 20, 2394-2407.

- [32] Zhang, M., Han, Y., Jia, C., Zheng, Z., Li, H., & Wu, C. (2022). Improving the microstructures and mechanical properties with nano-Al<sub>2</sub>O<sub>3</sub> treated wire in underwater submerged arc welding. *Journal of Manufacturing Processes*, 74, 40-51.
- [33] Amaral, E. C., Moreno-Uribe, A. M., & Bracarense, A. Q. (2021). Effects of PTFE on operational characteristics and diffusible H and O contents of weld metal in underwater wet welding. *Journal of Manufacturing Processes*, 61, 270-279.
- [34] Li, X., Zhang, Z., Peng, Y., Yan, D., Tan, Z., Zhou, Q., ... & Zhou, M. (2022). Microstructure and mechanical properties of underwater friction stir welding of CNT/Al-Cu-Mg composites. *Journal of Materials Research and Technology*, 18, 405-415.
- [35] Philip, A. J. P., Fjellidal, P. G., Remø, S. C., Selvam, C., Hamre, K., Espe, M., ... & Sissener, N. H. (2022). Dietary electrolyte balance of Atlantic salmon (*Salmo salar*) freshwater feeds: Impact on osmoregulation, mineral metabolism and performance in seawater. *Aquaculture*, 546, 737305.
- [36] Bar-Or, D., Rael, L. T., Bar-Or, R., Thomas, G. W., Slone, D. S., Melamed, I., & Craun, M. L. (2006). Severe systemic immune response syndrome, low plasma paraoxonase activity, and a new albumin species in a traumatized patient with Gaucher's disease. *Clinica chimica acta*, 374(1-2), 135-139.
- [37] Wang, Z., Zhang, Y., Wang, T., Hao, L., Lin, E., Chen, Y., ... & Zhang, Z. (2023). Organic flux synthesis of covalent organic frameworks. *Chem*, 9(8), 2178-2193.
- [38] Pereira, P. L., Arnold, D., de Baère, T., Gomez, F., Helmberger, T., Iezzi, R., ... & Taieb, J. (2020). A multicentre, international, observational study on transarterial chemoembolisation in colorectal cancer liver metastases: Design and rationale of CIREL. *Digestive and Liver Disease*, 52(8), 857-861.
- [39] Papageorgiou, N., Falconer, D., Wyeth, N., Lloyd, G., Pellerin, D., Speechly-Dick, E., ... & Bhattacharyya, S. (2020). Effect of tricuspid regurgitation and right ventricular dysfunction on long-term mortality in patients undergoing cardiac devices implantation: > 10-year follow-up study. *International Journal of Cardiology*, 319, 52-56.
- [40] Chan, Q., Wang, F., Shi, L., Ren, X., Ren, T., & Han, Y. (2022). Effects of chronic dietary hexavalent chromium on bioaccumulation and immune responses in the sea cucumber *Apostichopus japonicus*. *Comparative Biochemistry and Physiology Part C: Toxicology & Pharmacology*, 252, 109218.
- [41] Wise Sr, J. P., Wise, S. S., Holmes, A. L., LaCerte, C., Shaffiey, F., & Aboueissa, A. M. (2010). The cytotoxicity and genotoxicity of hexavalent chromium in Stellar sea lion lung fibroblasts compared to human lung fibroblasts. *Comparative Biochemistry and Physiology Part C: Toxicology & Pharmacology*, 152(1), 91-98.
- [42] Li, H., Liu, S., Sun, F., Ma, Q., Ji, H., Liu, H., & Chen, H. (2022). Improvement of microstructure and mechanical properties for underwater wet 16Mn/304L dissimilar steel welded joints assisted by presetting butter layer. *Materials Today Communications*, 33, 104259.
- [43] Zhang, X., Guo, N., Xu, C., Du, Y., Chen, B., & Feng, J. (2019). Influence of CaF<sub>2</sub> on microstructural characteristics and mechanical properties of 304 stainless steel underwater wet welding using flux-cored wire. *Journal of Manufacturing Processes*, 45, 138-146.
- [44] Sultana, M. N., & Dhar, N. R. (2023). RSM design-based hybrid approach to multi-response optimization in milling Ti-6Al-4 V alloy: A comparative study. *Materials Today: Proceedings*.
- [45] Şenol, H., Erşan, M., & Görgün, E. (2020). Optimization of temperature and pretreatments for methane yield of hazelnut shells using the response surface methodology. *Fuel*, 271, 117585.
- [46] Wang, J., Sun, Q., Pan, Z., Yang, J., & Feng, J. (2019). Effects of welding speed on bubble dynamics and process stability in mechanical constraint-assisted underwater wet welding of steel sheets. *Journal of Materials Processing Technology*, 264, 389-401.
- [47] Li, H., Liu, D., Yan, Y., Guo, N., Liu, Y., & Feng, J. (2018). Effects of heat input on arc stability and weld quality in underwater wet flux-cored arc welding of E40 steel. *Journal of Manufacturing Processes*, 31, 833-843.
- [48] Wang, J., Sun, Q., Zhang, S., Wang, C., Wu, L., & Feng, J. (2018). Characterization of the underwater welding arc bubble through a visual sensing method. *Journal of Materials Processing Technology*, 251, 95-108.
- [49] Chen, H., Guo, N., Huang, L., Zhang, X., Feng, J., & Wang, G. (2019). Effects of arc bubble behaviors and characteristics on droplet transfer in underwater wet welding using in-situ imaging method. *Materials & Design*, 170, 107696.
- [50] Pell, A., Kokkinis, G., Malea, P., Pergantis, S. A., Rubio, R., & López-Sánchez, J. F. (2013). LC-ICP-MS analysis of arsenic compounds in dominant seaweeds from the Thermaikos Gulf (Northern Aegean Sea, Greece). *Chemosphere*, 93(9), 2187-2194.
- [51] Rodriguez-Cea, A., Arias, A. L., de la Campa, M. F., Moreira, J. C., & Sanz-Medel, A. (2006). Metal speciation of metallothionein in white sea catfish, *Netuma barba*, and pearl cichlid, *Geophagus brasiliensis*, by orthogonal liquid chromatography coupled to ICP-MS detection. *Talanta*, 69(4), 963-969.
- [52] Erkan, N., & Özden, Ö. (2007). Proximate composition and mineral contents in aqua cultured sea bass (*Dicentrarchus labrax*), sea bream (*Sparus aurata*) analyzed by ICP-MS. *Food chemistry*, 102(3), 721-725.
- [53] Lenz, C., Behrends, T., Jilbert, T., Silveira, M., & Slomp, C. P. (2014). Redox-dependent changes in manganese speciation in Baltic Sea sediments from the Holocene Thermal Maximum: An EXAFS, XANES and LA-ICP-MS study. *Chemical Geology*, 370, 49-57.
- [54] Elseblani, R., Cobo-Golpe, M., Godin, S., Jimenez-Lamana, J., Fakhri, M., Rodríguez, I., & Szpunar, J. (2023). Study of metal and organic contaminants transported by microplastics in the Lebanese coastal environment using ICP MS, GC-MS, and LC-MS. *Science of The Total Environment*, 887, 164111.
- [55] Abdelaal, A., Sarayloo, M., Nims, D. K., Mohammadian, B., Heil, J., & Sojoudi, H. (2022). A flexible surface-mountable sensor for ice detection and non-destructive measurement of liquid water content in snow. *Cold Regions Science and Technology*, 195, 103469.
- [56] Sarkar, C., Spada, N., Xu, S., Shafer, M. M., & Hyslop, N. P. (2023). An inter-laboratory comparison of elemental loadings of PM<sub>2.5</sub> samples using energy-dispersive XRF and magnetic-sector ICP-MS. *Atmospheric Environment*, 293, 119463.
- [57] Ramkumar, D. H. S., & Kudchadker, A. P. (1990). Phase equilibria of water+  $\gamma$ -butyrolactone system. *Fluid phase equilibrium*, 55(1-2), 207-215.
- [58] Terán, G., Cuamatzi-Meléndez, R., Albitar, A., Maldonado, C., & Bracarense, A. Q. (2014). Characterization of the mechanical properties and structural integrity of T-welded connections repaired by grinding and wet welding. *Materials Science and Engineering: A*, 599, 105-115.



## OUTPUT POWER ESTIMATION OF A PHOTOVOLTAIC PANEL BY EXTREME LEARNING MACHINE

Serhat Toprak<sup>1</sup>, Resul Çöteli<sup>2</sup>, Mehmet Üstündağ<sup>3</sup>, Hikmet Esen<sup>2</sup>

<sup>1</sup>Ministry of Education, Elazığ, Turkey

<sup>2</sup>Firat University, Technology Faculty Department of Energy Systems Engineering, Elazığ, Turkey

<sup>3</sup>Malatya Turgut Ozal University, Faculty of Engineering, Department of Electrical-Electronics Engineering, Malatya/Turkey

### Abstract

Original scientific paper

In this study, the output power of a photovoltaic (PV) panel under different operating conditions was estimated with the help of an extreme learning algorithm (ELM). For this purpose, a PV panel with a power of 180W was installed, and the open circuit voltage, short circuit current, panel temperature, and solar radiation of this panel were measured and recorded at regular intervals. A total of 75 measurement data were obtained. The maximum power of the panel was calculated using the open circuit voltage and short circuit current information. While panel temperature and solar radiation were given as inputs to the regression model of the PV panel based on ELM, the output of the regression model was taken as the maximum power of the PV panel. To improve the prediction accuracy of ELM, the number of input neurons of ELM and the type of activation function used in the hidden layer were determined by trial and error method. The generated PV data set is separated into training and testing sets. The performance of the method was examined with the 5-fold cross-validation method. For this purpose, the dataset was divided into 5 equal parts. One of these parts was used for testing the ELM and the remaining four sets were used for training the ELM, and this was done by changing the test set each time. Thus, the network was trained and tested 5 times with different sets, and the test result of the network was obtained by averaging the sum of the performances of all test functions. Regression results obtained from ELM are given for different numbers of hidden layer neurons and different types of activation functions in the hidden layer. The best prediction result of ELM was obtained for the case where the hidden layer activation function was tangent sigmoid and the number of hidden layer neurons was 20. The R-values were found to be 1 when the number of hidden layer neurons was 20 and tangent and radial basis activation functions were used. From the results obtained, it has been seen that ELM predicts the output power of the PV panel with very high accuracy. It is concluded that ELM is a useful tool for estimating the PV panel output power.

**Keywords:** Extreme learning algorithm, regression, PV panel.

## ÇIKIŞ GÜCÜ ÜÇ ÖĞRENME ALGORİTMASI İLE BİR FOTOVOLTAİK PANELİN ÇIKIŞ GÜCÜ TAHMİNİ

### Özet

Orijinal bilimsel makale

Bu çalışmada, farklı çalışma şartları altında bir PV panelin çıkış gücü uç öğrenme algoritması (UÖA) yardımı ile tahmin edilmiştir. Bu amaçla, 180 W gücünde bir PV panel kurulmuş, bu panelin açık devre gerilimi, kısa devre akımı, panel sıcaklığı ve güneş ışınımı belirli aralıklarla ölçülerek kaydedilmiştir. Toplam 75 adet ölçüm verisi elde edilmiştir. Açık devre gerilimi ve kısa devre akımı bilgileri kullanılarak panelin maksimum gücü hesaplanmıştır. UÖA kullanılarak oluşturulan PV panelin regresyon modeline giriş olarak panel sıcaklığı ve güneş ışınımı verilirken, regresyon modelinin çıkışı PV panelin maksimum gücü olarak alınmıştır. UÖA'nın tahmin doğruluğunu iyileştirmek için UÖA'nın giriş nöron sayısı ve ara katmanda kullanılan aktivasyon fonksiyonu tipi deneme yanılma yöntemi belirlenmiştir. Oluşturulan veri kümesi eğitim ve test kümesi olarak ayrılmıştır. Yöntemin başarımı 5-katlamalı çapraz doğrulama yöntemi ile incelenmiştir. Bu amaçla, veri kümesi 5 eşit parçaya bölünmüştür. Bu parçalardan biri test için ayrılıp geri kalan dördü eğitim için kullanılmış ve bu işlem her defasında test kümesi değiştirilerek gerçekleştirilmiştir. Böylece 5 defa ağ farklı kümelerle eğitilip test edilmiş ve ağın test sonucu bütün test fonksiyonlarının performanslarının toplamının ortalaması alınarak elde edilmiştir. UÖA'dan elde edilen regresyon sonuçları farklı ara katman nöron sayısı ve farklı tip aktivasyon fonksiyonları için verilmiştir. UÖA'nın en iyi tahmin sonucu ara katman aktivasyon fonksiyonu tipinin tanjant sigmoid ve ara katman nöron sayısının 20 olduğu durum için elde edilmiştir. Elde edilen sonuçlardan UÖA'nın PV panelin çıkış gücünü çok yüksek doğrulukta tahmin ettiği görülmüş ve UÖA'nın PV panellerin çıkış gücünün tahmininde etkin bir araç olarak kullanılabileceğini göstermiştir.

**Anahtar Kelimeler:** Uç öğrenme algoritması, regresyon, PV Panel.

\*Corresponding author.

E-mail address: mehmet.ustundag@ozal.edu.tr (M. Üstündağ)

Received 18 January 2024; Received in revised form 01 March 2024; Accepted 15 April 2024

2587-1943 | © 2024 IJIEA. All rights reserved.

Doi: <https://doi.org/10.46460/ijiea.1421890>

## 1 Introduction

Solar energy is an environmentally friendly energy source. However, clouds and weather conditions can affect the availability of solar energy. Therefore, the electrical energy produced from solar energy may vary depending on different parameters. For these reasons, responding to load demand with solar power plants is a very difficult task. One way to prevent this situation is to estimate the output power of photovoltaic (PV) systems [1]. Different forecasting methods can be used to estimate solar energy. This forecast will help power plant operators monitor solar conditions and prepare for any rapid fluctuations in power output. Additionally, energy storage systems can be considered as one of the possible solutions that can help in dealing with changes in solar energy. In addition, energy storage systems bring high and maintenance costs to the system.

However, the power obtained from PV systems varies due to reasons such as solar radiation, shading, and panel protection. One approach to changing variability is to estimate PV output power as accurately as possible. Using such visions, the energy storage efficiency capacity of off-grid PV users can be optimized [2]. Similarly, grid-connected distributed PV energy usage schedules can be optimized, and grid-connected PV systems can use these forecasts to develop their strategies using electricity market offers, allowing system operators to better organize their reserves. The output power of a single PV system is highly affected by local weather changes. Photovoltaics has its disadvantages. Unpredictable weather conditions have a major impact on the electricity generation of solar power plant when connected to the electricity supply and distribution grids. For this reason, precise and reliable estimation of solar system output power are crucial for the safe and cost-efficient operation of the PV power system and forecasting [3].

If there are PV electricity generation plants with high power in the interconnected system, serious disruptions may occur in the network in case of cloudiness. In this case, the power at the PV output will show a rather large and sudden change. When this change in irradiance occurs during a sudden change in load, the situation will worsen [4]. Therefore, it is clear that reliable estimation tools are crucial for PV technologies, optimizing the performance of solar power plants in the planning and operating stages, and ultimately accurately assessing the economic return. Accurate estimation of solar power output is crucial to evaluate the actual performance of PV panels.

In literature, some methods have been proposed for the prediction of the solar panel's output power. In [5], an improved feedforward neural network model was proposed for power output prediction of solar panel. The neural network model was optimized using the particle swarm optimization algorithm. Two hidden layers were used in the neural network model and the inputs to this network are day, time, cloudiness index, air temperature, wind speed, air humidity, radiation, precipitation, and air pressure. In [6], a neural fuzzy network is proposed for the prediction of daily energy production. Day, irradiance, air temperature, wind speed, air humidity, and air pressure are given as input to the neuro-fuzzy network. The prediction accuracy of this model was evaluated with data obtained from three PV plants and the average prediction error was

found to be 5%. In [7], a hybrid model was proposed for the output power estimation of a solar power plant. The training set was divided into four groups according to the weather conditions, and each training set was used to train four support vector machine models. According to the weather types of the predicted day, the appropriate support vector machine model is selected. Data taken at 15-minute intervals yielded predictions for one day ahead with a mean square error of 10.5%. The mean square error for each support vector machine was 9.12% for the cloudy model, 12.6% for the foggy model, 12.4% for the rainy model, and 7.85% for the sunny model. In [8], a hybrid model combining a power support vector machine and a similar day method was used to predict power output for 50 days. In [9], a new method for PV power estimation based on machine learning, image processing, and acoustic classification techniques is proposed. In [10], a deep learning-based neural network is proposed to estimate solar irradiance. The results of the proposed method are compared with the results obtained from support vector machines and feedforward neural network methods. In [11], a residential distribution network is proposed for output power estimation of PV. In [12], compared the performance of four artificial neural networks (ANNs) models for predicting the PV solar power. They utilized four PV data sets and online weather data. The obtained results provide high accuracy in analysing weather data, which is suitable and useful for planning the PV plant. In Ref. [13], authors investigated the performance of deep learning methods and created models ANNs and recurrent neural networks to forecast solar radiation. Both hidden layers were included in the ANN model. In Ref. [14], to determine the PV modules' performance, an ANN model was developed. They used temperature and irradiance parameters as inputs and current and voltage parameters as outputs for their feed-forward artificial neural network model. Levenberg-Marquardt and robust back propagation are the two training algorithms the authors experimented with throughout training. An ANN technique was developed by Ref. [15] to investigate and model the fouling effect on solar PV glass. The network input variables were six meteorological data sets. There are 35 neurons in the single layer of this artificial neural network design. In order to forecast PV power output, Ref. [16] developed a model based on ANN and an adaptive neuro-fuzzy inference system. Horizontal and global diffused irradiances, air pressure and temperature outside, precipitation, wind speed, length of daylight, relative humidity, and panel surface temperature were chosen as network input parameters. This study's training algorithm was Levenberg-Marquardt. ANN-based artificial intelligence methods have widely used in estimating PV panel output power. However, ANN has some disadvantages such as low learning speed and local minima. There are two primary causes for this behavior. One of them is the use of slow gradient-based learning algorithms in neural network training, and the other is the learning algorithms iteratively adjustment of the networks' parameters [17]. Recently, a new learning algorithm called extreme learning machine (ELM) has been proposed to eliminate the drawbacks of the ANN. The studies on ELM showed that ELM is feasible and promising in real-time applications [18].

In this study, the output power of a PV panel under different operating conditions was tried to be estimated with the help of an Extreme Learning Machine (ELM). For this purpose, a PV panel with a power of 180 W was installed and the open circuit voltage and short circuit current of this panel, panel temperature, and solar radiation were measured and recorded at regular intervals. A total of 75 measurement data were obtained. The maximum power of the panel was calculated from the open circuit voltage and short circuit current. While panel temperature and solar radiation were given as inputs to the regression model of the PV panel based on ELM, the output of this regression model was taken as the maximum power of the PV panel. Some parameters of ELM (number of input neurons, type of activation function) were adjusted to give the best results by trial and error method. The dataset is separated into training and test sets. The performance of the proposed method was examined with the 5-fold cross-validation method. For this purpose, the dataset was divided into 5 equal parts. One of these parts is reserved for testing the network whereas the remaining four sets are used for training the network, and this is done by changing the test set each time. The network is trained and tested 5 times in total with different sets. The test result of the network is the average of the sum of the performances of all test functions. The ELM was implemented using MATLAB software. From the regression results obtained, it was seen that ELM predicted the output power of the PV panel with very high accuracy. In addition, results show that ELM can be a reliable tool for estimating the output power of solar panels.

## 2 The Mathematical Model of Photovoltaic

It is essential for a PV model to make precise predictions of dependable current-voltage (I-V) and power-voltage (P-V) curves in actual operating situations. The most common equivalent circuit that describes well the electrical behaviour of a PV system is the five-parameter circuit model, shown in Figure 1 [19]. This equivalent circuit model shown consists of the photo-current source  $I_L$ , the shunt resistor  $R_{sh}$ , a diode parallel to this resistor, and the series resistor  $R_s$ . When the amount of radiation falling on the cell increases, the electric current produced also increases. The voltage obtained from the solar cell is shown as  $V$ . The resistance value  $R_s$  shown in the series connection to the output end is equal to the semiconductor material's total resistance forming the cell and the contact resistances formed at the connection points of the cells. Parallel (shunt) resistance  $R_{sh}$  is taken as the sum of the resistances occurring between the layers and around the cell in materials with a thin film structure consisting of very thin layers. It is determined that the series resistance value is very small compared to the parallel resistance and could be neglected [19], [20], [21]. The actual resistance of the circuit can be considered as series resistance. In the ideal case,  $R_s$  is zero and  $R_{sh}$  is infinite. Although the perfect conditions are unattainable, manufacturers work towards minimizing the influence of both resistances to enhance their products [20].

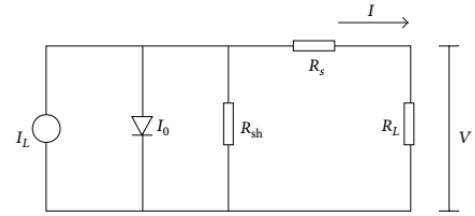


Figure 1. Single diode equivalent circuit for a solar cell.

From Figure 1, the output current of the cell is  $I_L$  can be written by using Kirchhoff's law as follows:

$$I = I_L - I_D - I_{sh}, \quad (1)$$

Diode current  $I_D$  can be written as follows:

$$I_D = I_o \left[ \exp\left(\frac{q(V + R_s I)}{nkT}\right) - 1 \right], \quad (2)$$

In Eq. 2,  $k$ ; Boltzmann constant,  $q$ ; unit electron charge amount,  $T$ ; It shows the absolute temperature of the cell in Kelvin. If Eq.1 is substituted into Eq.2, Eq.3 is obtained as follows:

$$I = I_L - I_o \left[ \exp\left(\frac{q(V + R_s I)}{nkT}\right) - 1 \right] - \frac{V + IR_s}{R_{sh}}, \quad (3)$$

## 3 Extreme Learning Machine

The fact that the learning rate of feedforward neural networks is generally much slower than necessary is a major problem in practice. There are two reasons:

- 1) These networks are typically trained using slow gradient-based learning algorithms.
- 2) The network's parameters are iteratively adjusted by this learning algorithm.

G. B. Huang suggested a unique learning strategy for the single hidden layer neural network (SLFN) that differs from these conventional training procedures. The extreme learning machine (ELM) is the name given to this learning method. In this learning algorithm, the input weights are selected randomly and the single hidden layer neural network's (SLFN) output weights are computed analytically. Theoretically, this learning method offers a fast learning rate with strong generalization performance. [22], [17].

Figure 2 shows the structure of a SLFN. In this figure,  $l$ ,  $w$ ,  $f$  present input weights, output weights, and activation function (AF) in the hidden layer, respectively [22].

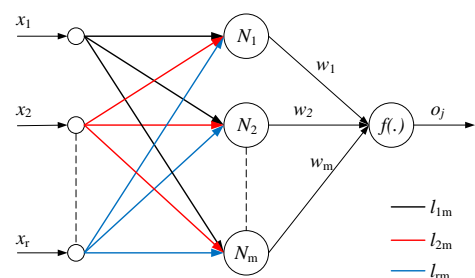


Figure 2. The architecture of a SLFN.

The SLFN's output can be obtained as follows:

$$o_j = \sum_{i=1}^m w_i f(l_i x_r + b_i) \tag{4}$$

In Eq.4;  $x$  is inputs;  $b$  is bias value. The standard SLFN can approximate the samples without error and there are values of  $w$ ,  $l$  and  $b$  that will make the error zero [11], [20]. The following equation shows one way to write the  $m$  set of equations.

$$H \times w = T \tag{5}$$

In Eq. 5;  $H$  is known as output matrix of the hidden layer and it can be obtained as follows:

$$H(l_1, \dots, l_m, b_1, \dots, b_m, x_1, \dots, x_m) = \begin{bmatrix} f(l_1 x_1 + b_1) & \dots & f(l_m x_1 + b_m) \\ \vdots & \dots & \vdots \\ f(l_1 x_m + b_1) & \dots & f(l_m x_m + b_m) \end{bmatrix}$$

A quick explanation of ELM for SLFNs are given as follows:

- a) Random assignments are made for the input weight and bias.
- b) For the hidden layer, the output matrix  $H$  is acquired.
- c) The output weight  $w$  is calculated [22].

Although ELM has many advantages, it may not be effective in estimating the output power of solar power plants where big data is available. In the current big data age, it is essential for creating an ELM algorithm that can train massive data sets. But when it comes to training massive data, the ELM has several drawbacks such as memory residency, difficulty with solving the matrix and online training [23].

#### 4 Simulations and Results

In this study, the power of a 180 W PV panel was tried to be estimated using ELM. For this purpose, solar radiation, panel temperature, open circuit voltage, and short circuit current of the PV panel were measured at 15-minute intervals. The maximum power of the panel was calculated using the open circuit voltage and short circuit current of the PV panel. The inputs of ELM are selected as panel temperature and solar radiation, and the output of ELM is the power of the panel. Additionally, input and output values to ELM were normalized and the results were given using 5-cross validation. The most important parameters affecting the performance of ELM are the number of hidden layer neurons and the type of  $AF$  in this layer. The regression performance of the ELM is given for different numbers of the hidden layer neurons and different types of  $AF$ .

Figure 3 shows the prediction results of ELM and actual results. The results are presented for tangent sigmoid activation function (TSAF) and hidden layer neurons (NHLN) with 10 and 20.

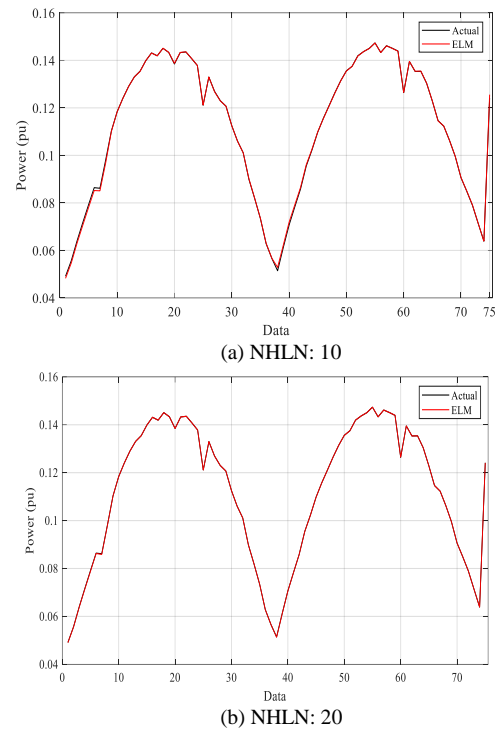


Figure 3. The actual results and prediction results of ELM for TSAF.

The regression results are given in Figure 4. When the number of hidden layer neurons is increased from 10 to 20, the R-value increases from 0.99998 to 1. When Figure 4(a) and (b) are examined, it is seen that the prediction performance of ELM increases as the number of hidden layer neurons increases.

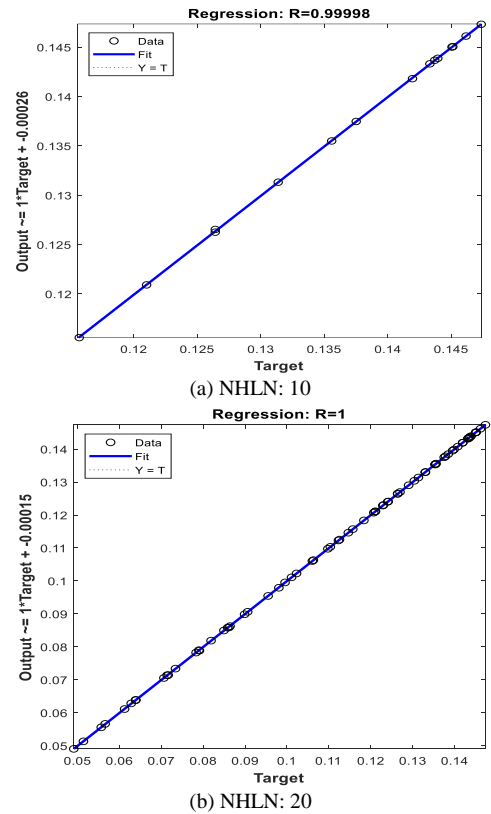
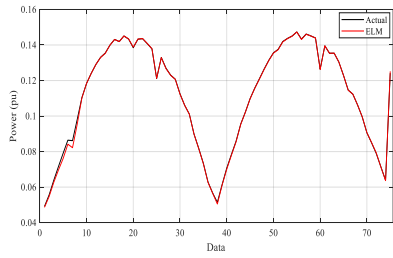
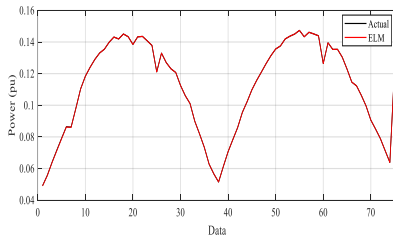


Figure 4. Regression curves for TSAF.

The prediction results of ELM, which uses a radial basis activation function (RBAF), and actual results are given in Figure 5 for the number of hidden layer cells, 10 and 20, respectively.



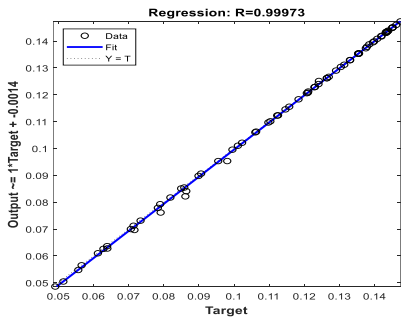
(a) The number of hidden neurons: 10



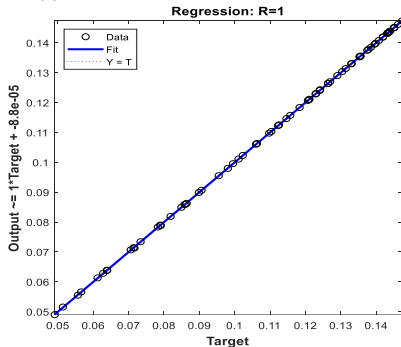
(b) The number of hidden neurons: 20

Figure 5. The actual results and prediction results of ELM for RBAF.

The regression results are given in Figure 6. When the number of hidden layer neurons is increased from 10 to 20, the R value increases from 0.99973 to 1. When Figure 6(a) and (b) are examined, it is seen that the prediction performance of ELM increases as the number of hidden layer neurons increases.



(a) The number of hidden neurons: 10.



(b) The number of hidden neurons: 20.

Figure 6. Regression curves for RBAF.

The regression performance of the ELM for different types of activation functions and different numbers of hidden layer neurons is shown in Table 1. As can be seen from the table, the lowest root mean square error (RMSE) was obtained by using TSAF and 20 hidden layer neurons.

Table 1. The regression performance of the ELM for different types of activation functions and different numbers of hidden layer neurons.

AF	NHLN	RMSE	Training time (s)
TSAF	10	$3.9646 \times 10^{-4}$	0.0136
	20	$4.5486 \times 10^{-5}$	0.0156
RBAF	10	$5.2283 \times 10^{-4}$	0.0156
	20	$4.8058 \times 10^{-5}$	0.0156

To better validate the performance of the proposed method, the comparison studies were conducted. In the comparison studies, neural network, linear regression and quadratic Gauss regression models were used. The regression result obtained from neural network is given in Figure 7. Tangent activation function and the number of hidden layer neurons are used in the neural network structure. R-value was obtained the 0.91598.

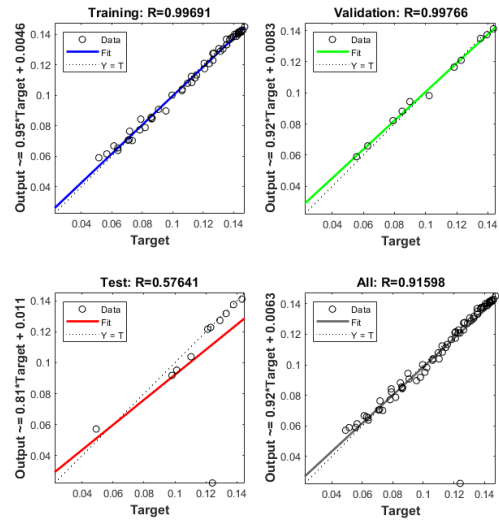


Figure 7. Regression curves for neural network.

Figure 8 and 9 show estimation results of linear regression and quadratic Gauss regression models. It is seen from these figures that linear regression model has better estimation performance than quadratic regression model.

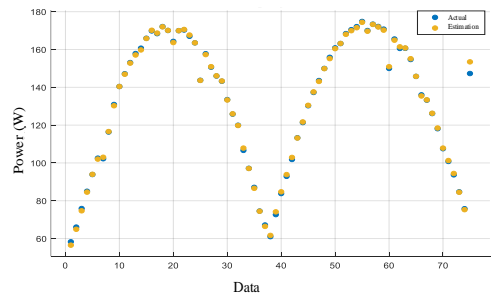


Figure 8. Estimation results of linear regression model.

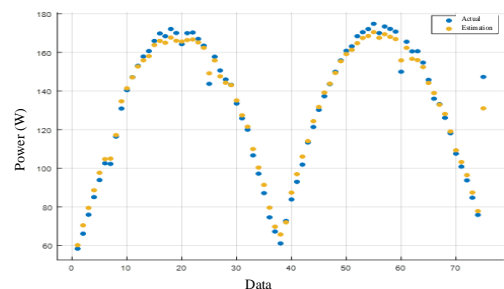


Figure 9. Estimation results of linear regression model.

## 5 Conclusion

This study presents an ELM based regression model for the estimation of PV panel output power. Training and test data for ELM was obtained from an experimentally established PV panel. PV panel has a power of 180 W. The irradiation on the panel, panel temperature, open-circuit voltage of the PV panel and short-circuit current of the PV panel, were recorded at 15-minute intervals. A total of 75 measurement data were obtained by measurements. Panel temperature and irradiation were applied to inputs of ELM whereas panel output power to output of the ELM. The ELM algorithm was carried out using MATLAB software. The optimal values of some parameters of the ELM such as input neurons, activation function are found by trial and error method to improve its regression performance. The regression performance of the ELM was evaluated by a 5-k fold. The ELM gives the best regression result for the case where the hidden layer activation function was tangent sigmoid and the number of hidden layer neurons was 20. The comparison studies were given to validate the regression performance of the ELM. The regression results show that the ELM predicts the output power of the PV panel with very high sensitivity.

Some factors such as the type of PV material, cloud and other shading effects, dust, module orientation and different weather conditions.

### Declaration

The authors declare that the ethics committee approval is not required for this study.

### References

- [1] Ela, E., Diakov, V., Ibanez, E., & Heaney, M. (2013). *Impacts of variability and uncertainty in solar photovoltaic generation at multiple timescales* (No. NREL/TP-5500-58274). National Renewable Energy Lab.(NREL), Golden, CO (United States).
- [2] Tian, J., Zhu, Y. Q., & Tang, J. N. (2010, September). Photovoltaic array power forecasting model based on energy storage. In *2010 5th International Conference on Critical Infrastructure (CRIS)* (pp. 1-4). IEEE.
- [3] Kumar, A. K., & Demir, F. (2022). Solar photovoltaic power estimation using meta-optimized neural networks. *Energies*, 15(22), 8669.
- [4] Tan, Y. T., & Kirschen, D. S. (2007, June). Impact on the power system of a large penetration of photovoltaic generation. In *2007 IEEE power engineering society general meeting* (pp. 1-8). IEEE.
- [5] Caputo, D., Grimaccia, F., Mussetta, M., & Zich, R. E. (2010, July). Photovoltaic plants predictive model by means of ANN trained by a hybrid evolutionary algorithm. In *The 2010 international joint conference on neural networks (IJCNN)* (pp. 1-6). IEEE.
- [6] Grimaccia, F., Mussetta, M., & Zich, R. (2011, June). Neuro-fuzzy predictive model for PV energy production based on weather forecast. In *2011 IEEE International Conference on Fuzzy Systems (FUZZ-IEEE 2011)* (pp. 2454-2457). IEEE.
- [7] Shi, J., Lee, W. J., Liu, Y., Yang, Y., & Wang, P. (2012). Forecasting power output of photovoltaic systems based on weather classification and support vector machines. *IEEE Transactions on Industry Applications*, 48(3), 1064-1069.
- [8] Xu, R., Chen, H., & Sun, X. (2012, August). Short-term photovoltaic power forecasting with weighted support vector machine. In *2012 IEEE International Conference on Automation and Logistics* (pp. 248-253). IEEE.
- [9] O'Leary, D., & Kubby, J. (2017). Feature selection and ANN solar power prediction. *Journal of Renewable Energy*, 2017(1), 2437387.
- [10] Alzahrani, A., Shamsi, P., Dagli, C., & Ferdowsi, M. (2017). Solar irradiance forecasting using deep neural networks. *Procedia computer science*, 114, 304-313.
- [11] Geetha, A., Santhakumar, J., Sundaram, K. M., Usha, S., Thentral, T. T., Boopathi, C. S., ... & Sathyamurthy, R. (2022). Prediction of hourly solar radiation in Tamil Nadu using ANN model with different learning algorithms. *Energy Reports*, 8, 664-671.
- [12] Lopes, S. M., Cari, E. P., & Hajimirza, S. (2022). A comparative analysis of artificial neural networks for photovoltaic power forecast using remotes and local measurements. *Journal of Solar Energy Engineering*, 144(2), 021007.
- [13] Pang, Z., Niu, F., & O'Neill, Z. (2020). Solar radiation prediction using recurrent neural network and artificial neural network: A case study with comparisons. *Renewable Energy*, 156, 279-289.
- [14] Halabi, L. M., Mekhilef, S., & Hossain, M. (2018). Performance evaluation of hybrid adaptive neuro-fuzzy inference system models for predicting monthly global solar radiation. *Applied energy*, 213, 247-261.
- [15] Laarabi, B., Tzuc, O. M., Dahlioui, D., Bassam, A., Flota-Bañuelos, M., & Barhdadi, A. (2019). Artificial neural network modeling and sensitivity analysis for soiling effects on photovoltaic panels in Morocco. *Superlattices and Microstructures*, 127, 139-150.
- [16] Kumar, K. R., & Kalavathi, M. S. (2018). Artificial intelligence based forecast models for predicting solar power generation. *Materials today: proceedings*, 5(1), 796-802.
- [17] Huang, G. B., Zhu, Q. Y., & Siew, C. K. (2004, July). Extreme learning machine: a new learning scheme of feedforward neural networks. In *2004 IEEE international joint conference on neural networks* (IEEE Cat. No. 04CH37541) (Vol. 2, pp. 985-990). Ieee.
- [18] Ahila, R., & Sadasivam, V. (2013). S Transform based extreme learning machine for power system disturbances classification. *Journal of The Institution of Engineers (India): Series B*, 94, 179-191.
- [19] Nguyen-Duc, T., Nguyen-Duc, H., Le-Viet, T., & Takano, H. (2020). Single-diode models of PV modules: A comparison of conventional approaches and proposal of a novel model. *Energies*, 13(6), 1296.
- [20] Premkumar, M., Chandrasekaran, K., & Sowmya, R. (2020). Mathematical modelling of solar photovoltaic cell/panel/array based on the physical parameters from the manufacturer's datasheet. *International Journal of Renewable energy development*, 9(1), 7.
- [21] Senthilkumar, S., Mohan, V., Mangaiyarkarasi, S. P., & Karthikeyan, M. (2022). Analysis of Single-Diode PV Model and Optimized MPPT Model for Different Environmental Conditions. *International Transactions on Electrical Energy Systems*, 2022(1), 4980843.
- [22] Huang, G. B., Zhu, Q. Y., & Siew, C. K. (2006). Extreme learning machine: theory and applications. *Neurocomputing*, 70(1-3), 489-501.
- [23] Chen, C., Li, K., Duan, M., & Li, K. (2017). Extreme learning machine and its applications in big data processing. In *Big data analytics for sensor-network collected intelligence* (pp. 117-150). Academic Press.



## NUMERICAL SOLUTIONS TO THE STOCHASTIC SYSTEMS WITH FRACTIONAL OPERATORS

Mehmet Ali Akinlar<sup>\*1</sup> 

<sup>1</sup>Bandırma Onyedi Eylül University, Faculty of Engineering and Natural Science, Engineering Sciences Department, 10200, Bandırma, Balıkesir, Turkey

### Abstract

Original scientific paper

Fractional-stochastic differential equations are widely used tools to simulate a wide - range of engineering and scientific phenomena. In this paper, the applicability of the approach of indeterminate coefficients to various fractional-stochastic models is examined. These models have a fractional white noise term and are mostly produced by fractional-order derivative operators. We also investigate applications of a polynomial chaos algorithm to stochastic Lotka-Volterra and Benney systems. Fractional-stochastic equations are entirely novel systems that have the potential to function as models for a wide range of scientific and engineering phenomena. It is noted that fractional-order systems with uncertainty or a noise term can benefit from the effective use of Galerkin-type approaches in this article.

**Keywords:** Galerkin methods, numerical solutions, stochastic systems with fractional operators.

## KESİRLİ MERTEBELİ DİFERANSİYEL DENKLEMLERİN YENİ SAYISAL ÇÖZÜMLERİ

### Özet

Orijinal bilimsel makale

Kesirli stokastik diferansiyel denklemler, çok çeşitli mühendislik ve bilimsel olguları simüle etmek için yaygın olarak kullanılan araçlardır. Bu makalede, belirsiz katsayılar yaklaşımının çeşitli kesirli stokastik modellere uygulanabilirliği incelenmiştir. Bu modeller kesirli beyaz gürültü terimine sahiptir ve çoğunlukla kesirli dereceli türev operatörleri tarafından üretilir. Ayrıca polinom kaos algoritmasının stokastik Lotka-Volterra ve Benney sistemlerine uygulamalarını da araştırıyoruz. Kesirli stokastik denklemler, çok çeşitli bilimsel ve mühendislik problemleri için model olarak işlev görme potansiyeline sahip tamamen yeni sistemlerdir. Bu makalede Galerkin tipi yaklaşımların etkin kullanımından ve belirsizlik veya gürültü terimi içeren kesirli dereceli sistemlere uygulanabilirliği araştırılmıştır.

**Anahtar Kelimeler:** Galerkin yöntemleri, sayısal çözümler, stokastik sistemler, kesirli operatörler.

### 1 Introduction

Stochastic differential equations and fractional order derivative operators,  $\{2,4,5,11,12,13,14,15\}$  are invaluable tools for applications in many different areas of science and engineering. For example, they are used in monitoring chemical processes operating under uncertainty, in image processing such as feature extraction and image segmentation, in analyzing, designing, and testing electronic systems, and in many other engineering applications such as big data analysis, robotics, machine learning, and artificial intelligence.

A fractional-stochastic differential equation has some terms of fractional-order derivative/integral operators, certain deterministic operators, noise (expressed as a derivative of the Wiener process), and fractional-Brownian motion. There may be more terms in these kinds of equations, including Levy-type noise or jump. Some of

the well-known  $\{1,3\}$  fractional-order operators with nonsingular kernels and integral properties, such as Riemann-Liouville, Caputo, Grünwald-Letnikov, and Atangana-Baleanu, are more efficient than deterministic maps. Ito's formula is primarily used to obtain exact solutions of fractional-stochastic differential equations, but these solutions are only obtained in a few specific instances. Thus, among the most important and helpful numerical solution methods in computational mathematics are those using Euler's type, finite differences, and indeterminate coefficients (Galerkin, Least-square, Collocation, Wavelets, and Finite Elements).

The primary goal of the current research work is to examine how some finite-element, polynomial chaos and Galerkin methods can be applied to specific and original differential equations. Deterministic derivative operators, fractional-order derivative operators in the Caputo and

\*Corresponding author.

E-mail address: mehmetaliakinlar@gmail.com (M. A. Akinlar)

Received 27 March 2024; Received in revised form 18 May 2024; Accepted 20 May 2024

2587-1943 | © 2024 IJIEA. All rights reserved.

Doi: <https://doi.org/10.46460/ijiea.1459659>

Riemann-Liouville (RL) sense, fractional-Brownian motion, standard Brownian motion, and fractional white noise are the fractional-stochastic systems of equations that are examined in this work. Not a single equation or system taken into consideration in this study has ever been researched in the past. According to this perspective, the current work represents a fresh and innovative addition to science. Investigating the suitability of various indeterminate coefficient approaches for fractional-stochastic models renders this work novel and highly valuable for computer science researchers.

The novelty of this research study can be presented as follows: First of all, both research topics and tools, fractional-order stochastic differential equations and fractional Brownian motion are the tools that can be used in the modeling of many different engineering and scientific phenomena in physics and biology in a highly efficient manner. In this paper, we employ both tools and apply them to the models not considered in the literature in the way we study. Fractional Brownian motion is a very helpful tool for researchers because of its long-range dependence, correlated time increments, and Hurst parameter features. We address the conjunction of fractional operators with white noise and fractional Brownian motion; these tools' combination and application to scientific and engineering problems are still in their infancy. From these points of view, the present study is going to be useful for the researchers in these areas.

## 2 Fundamentals of Fractional Operators

In recent years, fractional-order calculus, often known as differential equations, has become increasingly important in applied and computational mathematics. These equations are produced by fractional-order operators, such as derivative and integral operators. They worked in various scientific fields, including engineering, physics, economics, and mathematics. Because fractional-order operators may compute non-locally and account for historical impacts, they are more effective and preferred in applications.

Suppose that  $g: (0, \infty) \mapsto \mathbb{R}$  is a function and fractional-order operator with the order  $\beta$  for  $g$  is defined as

$$J^\beta g(s) = \frac{1}{\Gamma(\beta)} \int_0^t (s - \sigma)^{\beta-1} g(\sigma) d\sigma,$$

inhere  $\Gamma(\cdot)$  denotes Gamma function.

For  $(m \in \mathbb{N})$ , Caputo-type derivative operator of order  $\beta$ ,  $m - 1 < \beta < m$ , of  $g(s)$  is given by

$$D^\beta g(s) = J^{m-\beta} \frac{d^m}{dt^m} g(s).$$

The Riemann-Liouville (RL) type integral,  $I_x^\alpha f(x)$  and derivatives  $R_x^\alpha f(x)$  of a function, say  $f(x)$ , of order  $\alpha$  is:

$$I_x^\alpha f(x) = \frac{1}{\Gamma(\alpha)} \int_a^x (x - \rho)^{\alpha-1} f(\rho) d\rho, \quad x \in [a, b].$$

It is obvious that:

$$I_x^\beta (I_x^\alpha f(x)) = I_x^{\beta+\alpha} f(x) \text{ and } \frac{d}{dx} I_x^{1+\alpha} = I_x^\alpha f(x).$$

$$R_x^\alpha f(x) = \frac{1}{\Gamma(n - \alpha)} \frac{\partial^n}{\partial x^n} \int_a^x \frac{f(\rho) d\rho}{(x - \rho)^{\alpha+1-n}} \quad \text{for } n - 1 < \alpha \leq n.$$

For  $n = 2$ , i.e. for  $1 < \alpha \leq 2$ , one has

$$R_x^\alpha f(x) = \frac{1}{\Gamma(2 - \alpha)} \frac{\partial^2}{\partial x^2} \int_a^x \frac{f(\rho) d\rho}{(x - \rho)^{\alpha-1}}.$$

## 3 The Galerkin Method

One of the unique varieties of procedures for unknown coefficients is the Galerkin approach. Next, we go over the basic concepts of the Galerkin technique in brief.

Let us consider the differential equation (which can be hybrid, fractional, deterministic, or stochastic).

$$Fu(x) = k(x)$$

where  $F$  is a derivative operator, functions  $u(x)$  and  $k(x)$  are given functions. Write  $u(x)$  as

$$u(x) = \sum_{i=1}^n d_i \varphi_i(x)$$

in which  $\varphi_i(x)$  is known as the coordinate function and the coefficients,  $d_i$  are constants or functions to be determined. Let us define the so-called residual term  $R(x)$  as

$$R(x) := Fu(x) - k(x)$$

and define the following operator

$$I_j(d_1, d_2, \dots, d_n) := \int_a^b W_j(x) R(x) dx = 0.$$

Choosing weight function  $W_j(x)$  in this equation as  $W_j(x) := \varphi_i(x)$ , the Galerkin method (one of the undetermined coefficients methods) becomes the name of the resulting technique.

## 4 Brownian Motion

Brownian motion (or Wiener process) is a stochastic process  $(W_x)_{x \geq 0}$  defined on a probability space  $(\mathcal{X}, \mathcal{F}, \mathcal{P})$  with:

- $W_0 = 0$ ,
- the function  $x \mapsto W_x$  is a continuous function with probability 1,
- the increments  $W_{x+n} - W_x$  have a normal distribution,  $\mathcal{N}(0, n)$ .

Independent increments mean  $W_x - W_l$  and  $W_k - W_m$  are independent random variables for  $0 \leq l \leq x \leq m \leq k$ .  $W(x)$  satisfies that:

$$\frac{dW(x)}{dx} \approx \frac{d\widehat{W}(x)}{dx} = \sum_{k=1}^n \rho_k \delta_k(x),$$

$$\rho_k = \frac{1}{\sigma} \int_{I_k} \delta_k(x) dW(x) \in \mathcal{N}\left(0, \frac{1}{\sigma}\right),$$

that is a standard normal random variable

$$dW(x) := dW(x_{i+1}) - dW(x_i), \text{ where } I = \{I_k | I_k := [x_{k-1}, x_k], x_k - x_{k-1} = \sigma, x_0 = 0, x_n = 1\}$$

If  $f$  is a bounded function, it is not hard to see that

$$E\left(\int_I f(dW(x) - d\widehat{W}(x))\right) = 0.$$

Another important and highly helpful method in science, engineering, and finance modeling a wide range of events is fractional-Brownian motion or fBm. It is a very useful tool for scientists because of its long-range dependence, correlated time increments, and Hurst parameter features. The definition and intriguing characteristics of fBm, for instance, can be found in [10] for interested readers. The literature has a wide variety of fBm kinds. We think about

$$B^H(s, x) = \sum_{k=1}^{\infty} \sqrt{\mu_k} e_k(x) \alpha_k(s), \quad \sum_i \mu_i < \infty,$$

$$e_k(x) = \sqrt{2} \sin(k\pi x), \quad k = 1, 2, \dots,$$

$$B^H(s_n, x) - B^H(s_{n-1}, x) = \sum_{k=1}^{\infty} \sqrt{\mu_k} e_k(x) (\alpha_k(s_n) - \alpha_k(s_{n-1})),$$

$$\alpha_k(s_n) - \alpha_k(s_{n-1}) = \sqrt{\Delta t} \zeta_{k,n}, \quad \zeta \in \mathcal{N}(0, 1).$$

In the following part, we present and analyze the first fractional-stochastic differential model. We deal with numerical solutions of a partial differential equation (PDE) that is fractionally stochastic and contains various derivatives of an unknown function of  $s$  and  $x$ , as well as a Levy noise term, fractional white noise, and a second-order time derivative. We examine a unique differential problem that has not been approached using finite element methods in previous research. The goal of analyzing such an equation is to demonstrate how original the equation is, as well as how helpful these kinds of equations are in representing a wide range of phenomena in science and engineering. Numerical solutions of the following equation are of interest to us:

$$u_{ss}(s, x) - u_{xx}(s, x) - u(s, x) + dB^H(s) - \frac{\partial}{\partial x} \left[ f(u(s, x)) \frac{\partial u(s, x)}{\partial x} \right] = g(s, x) \quad (1)$$

where  $(s, x) \in \Omega := [0, 1] \times [0, 1]$  and  $u(s, x) = 0$  in  $\partial\Omega$ . Weak form of ([maineq2]):

$$\langle u_{ss}(s, x), w \rangle - \langle u_{xx}(s, x), w \rangle - \langle u(s, x), w \rangle + \langle dB^H(s, x), w \rangle \left\langle -\frac{\partial}{\partial x} \left[ f(u(s, x)) \frac{\partial u(s, x)}{\partial x} \right], w \right\rangle = \langle g(s, x), w \rangle \quad (2)$$

After using a finite element approach to solve (1), we finally arrive at an element matrix equation that can be solved using both an implicit numerical method and a finite difference. Let us now write (2) in variational form first. To begin doing this, let's first express the unknown function  $u(s, x)$  as

$$u(s, x) := \sum_{i=1}^M a_i(s) \varphi_i(x)$$

where  $\varphi_i(x)$  is a coordinate function. We write  $u(s, x)$  in the equation (2) using the variational formulation technique. We then multiply each term in (2) by  $\varphi_j(x)$ , and integrate the resulting function on the boundaries of  $x$ . Consequently, we get that

$$\sum_{i=1}^M \ddot{a}_i(s) \int_0^1 \varphi_i(x) \varphi_j(x) dx - \sum_{i=1}^M a_i(s) \int_0^1 \frac{d^2 \varphi_i(x)}{dx^2} \varphi_j(x) dx - \sum_{i=1}^M a_i(s) \int_0^1 \varphi_i(x) \varphi_j(x) dx + \int_0^1 \varphi_j(x) dB^H(s, x) dx = \int_0^1 \frac{\partial}{\partial x} \left[ f \left( \sum_{i=1}^M a_i(s) \varphi_i(x) \right) \sum_{i=1}^M a_i(s) \frac{d\varphi_i(x)}{dx} \right] \varphi_j(x) dx = \int_0^1 g(s, x) \varphi_j(x) dx \quad (3)$$

Our objective is to formulate the equation (3) using a few matrices. To that end, allow us to define the following matrices:

Define  $K_{M \times M}$  with entries  $K_{ij}$  as

$$K_{ij} = \int_0^1 \varphi_i(x) \varphi_j(x) dx.$$

Hence, the first integral in (3) can be written

$$K^T \ddot{a}$$

where  $a$  is a  $M \times 1$  vector with entries  $a_i, i = 1, 2, \dots, M$ . Using the boundary conditions and integration by parts method, the second integral is written as

$$N^T a$$

where  $N_{M \times M}$  is a matrix.

Now, let us write the last two terms in (3) as follows:

$$\sum_{i=1}^M a_i(s) \int_0^1 f \left( \sum_{i=1}^M a_i(s) \varphi_i(x) \right) \frac{d\varphi_i(x)}{dx} \frac{d\varphi_j(x)}{dx} dx \quad (4)$$

$$= \langle g(s, x), w \rangle$$

Concerning the unknown  $a_i(s)$  in equation ([togethers]), it is evident that we have a nonlinear system of equations. Consequently, (4) can be expressed in terms of a few matrices as

$$L(a)a = c$$

where  $L_{M \times M}$  is a matrix with:

$$L_{ij} = \int_0^1 \left[ f \left( \sum_{i=1}^M a_i(s) \varphi_i(x) \right) \frac{d\varphi_i(x)}{dx} \frac{d\varphi_j(x)}{dx} \right] dx$$

and  $c$  is a  $M \times 1$  matrix with entries  $c_i = \int_0^1 g(s, x) \varphi_j(x) dx$ .

We express the fourth term, using the fBm notations that were discussed in the preceding section. The equality

$$\int_0^1 d B^H(s, x) \varphi_j(x) dx = \sum_{k=1}^M \sqrt{\mu_k} \alpha_k(s) \int_0^1 e_k(x) \varphi_j(x) dx,$$

can be written as a vector, say  $d$ , with the size of  $M \times 1$ . As a result, after correctly organizing these matrices in the equation (4), we get the matrix equation:

$$K^T \ddot{a} - (N^T + K^T)a - L(a)a = c - d \quad (5)$$

Now, we may express the temporal derivative using the finite difference approximation. Therefore, we write

$$K^T \left[ \frac{a_{k+1} - 2a_k + a_{k-1}}{\Delta t^2} \right] - N^T a_k - K^T a_k - L(a_k)a_k = c - d$$

from which we obtain that

$$a_{k+1} = [(K^T)^{-1}(N^T a_k + K^T a_k + L(a_k)a_k + c - d)] \Delta t^2 + 2a_k - a_{k-1}$$

In the following section, we investigate numerical solutions to fractional-stochastic differential equations using the Riemann-Liouville interpretation of the fractional derivative operator.

### 5 Fractional-Stochastic Equation

Consider

$$R_x^{1+\alpha} u(x) - u_{xxx}(x) + dW(x) = g(x), \quad x \in [0,1] \quad (6)$$

with  $u(0) := 0$ , and  $u(1) := k \in \mathbf{R} - 0$ , where  $R_x^{1+\alpha} u(x)$  is the Riemann-Liouville type derivative of  $u(x)$ . Let's use the above-described Galerkin technique methodology to apply the Galerkin method to Eq. (6):

$$\int_0^1 R_x^{1+\alpha} u(x) \varphi_j(x) dx - \int_0^1 u_{xxx}(x) \varphi_j(x) dx + \int_0^1 dW(x) \varphi_j(x) dx = \int_0^1 g(x) \varphi_j(x) dx \quad (7)$$

where  $\varphi_j(x)$  is nodal based function defined on  $\Omega$ .

Defining

$$u = \sum_{k=0}^M c_k \varphi_k(x)$$

Let

$$\Delta := \frac{1}{n}$$

$\varphi_j(x)$  is an appropriate base function. Using integration by part in the second term in (7), we get:

$$\sum_{k=0}^M c_k \int_0^1 R_x^\alpha \varphi_k(x) \varphi_j(x) dx + \sum_{k=0}^M c_k \int_0^1 \frac{d^2 \varphi_k(x)}{dx^2} \frac{d\varphi_j(x)}{dx} dx + \sum_{k=0}^M \int_0^1 \rho_k \delta_k(x) \varphi_k(x) dx = \int_0^1 g(x) \varphi_j(x) dx$$

This equation's discretization is provided as follows:

$$\frac{1}{\Delta} \left[ \sum_{k=0}^M c_k \int_{x_{l-1}}^{x_l} R_x^\alpha \varphi_k(x) dx - \sum_{k=0}^M c_k \int_{x_l}^{x_{l+1}} R_x^\alpha \varphi_j(x) dx \right] + \sum_{k=0}^M c_k \int_0^1 \frac{d^2 \varphi_k(x)}{dx^2} \frac{d\varphi_j(x)}{dx} dx + \sum_{k=1}^M \int_0^1 \rho_k \delta_k(x) \varphi_k(x) dx + \sum_{k=0}^M \int_0^1 \rho_k \delta_k(x) \varphi_k(x) dx = \int_0^1 g(x) \varphi_j(x) dx$$

This equation can be expressed as a matrix equation or in terms of matrices as follows:

$$(F^T - L^T)c + M - G = 0,$$

in which,

$$M = \sum_{k=1}^M \int_0^1 \rho_k \delta_k(x) \varphi_k(x) dx$$

$$L_{ij} = \int_0^1 \frac{d^2 \varphi_k(x)}{dx^2} \frac{d\varphi_j(x)}{dx} dx$$

$$G_j = \int_0^1 g(x) \varphi_j(x) dx$$

The application of the Galerkin method to a system of fractional-order differential equations will be examined in the following section. Since we had investigated how noise behaves in fractional-order differential equations in the earlier instances, we do not add a noise term, therefore these equations are somewhat deterministic fractional differential equations.

### 6 A Fractional-Stochastic System of PDEs

Consider

$$D_s^\alpha u(s, x) = \beta u_{xx}(s, x) + v_x(s, x) + h(s, x)$$

$$D_s^\alpha v(s, x) = v_{xx}(s, x) + \tau u_x(s, x)$$

where  $\alpha, \beta, \tau$  are positive parameters,  $x \in [0, A]$ ,  $A > 0$ ,  $0 \leq t$ , with

$$u(0, x) = u(s, 0) = v(s, 0)$$

$$v(0, x) = u(s, A) = v(s, A) = 0, \quad x \in [0, A]$$

$$\frac{\partial u(s, x)}{\partial x} = \frac{\partial v(s, x)}{\partial x} = 0, \quad \text{at } x = 0,$$

and  $x = A, t \geq 0$ .

These kinds of systems of partial differential equations can simulate a variety of physics, chemical, and engineering problems. We chose to explore this system of equations since it is an original differential equation, and systems of differential equations are used to model many scientific phenomena.

The system is transformed into a linear system of finite element matrix equations using the FEM, a kind of weighted residual approach. The solutions to these matrix equations are found by highly efficient computing methods.

This system of fractional order differential equations is solved using a Galerkin type method as follows:

$$u(s, x) \approx \hat{u}(s, x) = N(x)U^e(s)$$

$$v(s, x) \approx \hat{v}(s, x) = N(x)V^e(s)$$

where  $N(x)$  is a row vector made up of what are known as basis functions on a  $L$ -length space element. Note that in the weighted residual method, the basis functions we use in this study serve as the weight functions. As a result, we employ a finite element method—a kind of weighted residual technique—in the following section.

Taking note of them, we can see that the approximate system of equations (8) can be expressed as follows:

$$D_s^\alpha \hat{u}(s, x) = \beta \hat{u}_{xx}(s, x) + \hat{v}_x(s, x) + h(s, x)$$

$$D_t s^\alpha \hat{v}(s, x) = \hat{v}_{xx}(s, x) + \tau \hat{u}_x(s, x)$$

We investigate the one-space element  $\Gamma_e$ , which is an interval since we study on an interval, which is a one-dimensional space. Considering this, the first equation in the system (9) can be written as

$$D_s^\alpha \hat{u}(s, x) = \beta \hat{u}_{xx}(s, x) + \hat{v}_x(s, x) + h(s, x)$$

Thus, we have

$$\int_{\Gamma_e} N^T(x) \begin{bmatrix} N(x) D_s^\alpha U^e(s) \\ -\beta \frac{d}{dx} \left( \frac{dN(x)}{dx} U^e(s) \right) \\ + \frac{dN(x)}{dx} V^e(s) \\ + h(s, x) \end{bmatrix} d\Gamma_e = \{0\},$$

Using the integration-by-parts method, we have

$$\int_{\Gamma_e} [N^T(x) N(x) D_s^\alpha U^e(s) - \beta \frac{dN(x)}{dx} \frac{dN^T(x)}{dx} U^e(s) N^T(x) \frac{dN(x)}{dx} V^e(s) + N^T(x) h(s, x)] d\Gamma_e - \left[ \beta N^T(x) \frac{dN(x)}{dx} U^e(s) \right]_{\partial\Gamma} = \{0\},$$

by  $N(x) \equiv 0$  on  $\partial\Gamma$ , we get

$$\int_{\Gamma_e} \begin{bmatrix} N^T(x) N(x) D_s^\alpha U^e(s) \\ -\beta \frac{dN(x)}{dx} \frac{dN^T(x)}{dx} U^e(s) \\ + N^T(x) \frac{dN(x)}{dx} V^e(s) - N^T(x) h(s, x) \end{bmatrix} d\Gamma_e = \{0\},$$

(10)

We write the equation (10) via matrices as

$${}^e D_s^\alpha U^e(s) + ([B(x)]^e) U^e(s) + ([C(x)]^e) V^e(s) = H^e(s, x)$$

(11)

where

$$[A(x)]^e = \int_{\Gamma_e} N^T(x) N(x) d\Gamma_e$$

$$[B(x)]^e = - \int_{\Gamma_e} \beta \frac{dN^T(x)}{dx} \frac{dN(x)}{dx} d\Gamma_e$$

$$[C(x)]^e = \int_{\Gamma_e} N^T(x) \frac{dN(x)}{dx} d\Gamma_e$$

$$H^e(s, x) = N^T(x) h(s, x)$$

Now, we express the second equation in the system (9)

$$D_s^\alpha v(s, x) = v_{xx}(s, x) + \tau u_x(s, x)$$

as:

$$\int_{\Gamma_e} N^T(x) \left[ \begin{array}{c} N(x)D_s^\alpha V^e(s) \\ -\frac{d}{dx} \left( \frac{dN(x)}{dx} V^e(s) \right) \\ +\tau \frac{dN(x)}{dx} U^e(s) \end{array} \right] d\Gamma_e = \{0\} \quad (12)$$

The equation (12) can be restated as

$$\int_{\Gamma_e} \left[ N^T(x)N(x)D_s^\alpha V^e(s) - \frac{dN^T(x)}{dx} \frac{dN(x)}{dx} V^e(s) + \tau N^T(x) \frac{dN(x)}{dx} U^e(s) \right] d\Gamma_e - \left[ N^T(x) \frac{dN(x)}{dx} V^e(s) \right]_{\partial\Gamma_e} = \{0\}$$

by the boundary conditions, we get

$$\int_{\Gamma_e} \left[ N^T(x)N(x)D_s^\alpha V^e(s) - \frac{dN^T(x)}{dx} \frac{dN(x)}{dx} V^e(s) + \tau N^T(x) \frac{dN(x)}{dx} U^e(s) \right] d\Gamma_e = \{0\}$$

Likewise, we have:

$${}^e D_s^\alpha V^e(s) + \left( \frac{1}{\beta} [B(x)]^e V^e(s) = [C(x)]^e U^e(s) \right) \quad (13)$$

Now, we can rewrite the equations (11) and (13) by localizing the element matrices as:

$${}^e D_s^\alpha U^e(s) + ([B(x)]^e)U^e(s) + ([C(x)]^e)V^e(s) = H^e(s, x)$$

$${}^e D_s^\alpha V^e(s) + \left( \frac{1}{\beta} [B(x)]^e V^e(s) = [C(x)]^e U^e(s) \right)$$

In the following part, we apply the polynomial chaos method to two nonlinear systems of stochastic ordinary differential equations: the Lotka-Volterra system and the Banney equation, a nonlinear stochastic differential equation.

### 7 Polynomial Chaos Method

Because they can accurately simulate systems with uncertainty, randomness, and noise, stochastic differential equations are important in both engineering and economics. This section examines the suitability of the polynomial chaos (PC) approach for several partial differential equations and stochastic nonlinear predator-prey scenarios. Specifically, we are interested in the approximate solutions of the Benney and stochastic Lotka-Volterra equations. A particular instance of indeterminate coefficients or the Galerkin method is the polynomial chaos approach. We provide approximate solutions for stochastic systems and show simulations to illustrate the impact of uncertainties on the systems. This is the first study in the history of research to demonstrate how the polynomial chaos approach may be used to the Lotka-Volterra system and the Benney equation.

The Lotka-Volterra (LV) equations are a couple of first-order, non-linear differential equation systems that

are mostly used in mathematical biology, namely in the modeling of predator-prey model dynamics (see, for example, 6,7,8,9). The Lotka-Volterra equations are regarded as random or stochastic processes. We present a novel method for numerical solutions of Lotka-Volterra (LV) equations with some uncertainty present in the system, based on polynomial chaos (PC) expansions. One of the most effective methods for perturbing a stochastic differential equation into a deterministic system of equations is the PC technique.

Numerous methods have been proposed in the literature to solve stochastic linear partial differential equations. As an example, consider the stochastic LV model employing the semi-martingale technique at Klebaner et al. They establish a huge deviation principle and derive a bound for the asymptotic time to the prey population's extinction.

The polynomial chaos expansion approach is then briefly reviewed, and stochastic Lotka-Volterra models and Benney equations are introduced. We then address the numerical solutions of these systems by using the PC method on them.

### 8 Stochastic Galerkin Method

Given a probability space denoted by  $(\Omega, \mathcal{A}, \mathcal{P})$ , we can investigate the following general time-dependent stochastic partial differential equation with random coefficients:

$$\begin{aligned} \frac{\partial u}{\partial s} + \Gamma(s, x, v; u) &= f, (s, x) \in \mathcal{D} \times [0, T_f] \\ \mathcal{C}(s, x, v; u) &= g, (s, x) \in \partial\mathcal{D} \times [0, T_f] \\ \mathcal{K}(0, x, v; u) &= h, x \in \mathcal{D}, \end{aligned}$$

where the coordinates are  $v$  –random or uncertain,  $s$  –time, and  $x$  –space. This system's solution could be expressed as

$$u(s, x, v): \mathcal{D} \times [0, T_f] \times \Omega \rightarrow \mathbb{R}$$

$$\mathcal{D} \subset \mathbb{R}^D, D = 1,2,3.$$

We need to compute  $u(s, x, v)$  to solve this system. First, let's presume that:

$$a(x, y) \equiv a(x, y_1(v), \dots, y_d(v)).$$

Then,

$$u(s, x, y_1(v), \dots, y_d(v)): \mathcal{D} \times [0, T] \times \prod_{i=1}^d \Gamma_i \rightarrow \mathbb{R}$$

$$y_i: \Omega \rightarrow \Gamma_i$$

Some common techniques in the literature to calculate  $u(s, x, v)$  include the Galerkin, finite elements, wavelets, collocation, and least-squares approaches for indeterminate coefficients. We employ the stochastic Galerkin approach, which is best explained as follows: Given the random space

$$\mathcal{S} \equiv L_2(\mathcal{L}, \mathcal{P}_y),$$

i. Construct an approximate space.

$$\mathcal{S}_p \equiv \text{Span}\{\psi_0(y), \psi_1(y), \dots, \psi_p(y)\} \subset \mathcal{S}$$

ii. Show the ambiguities as

$$\hat{a}(x, y) = \sum_i a_i(x) \psi_i(y)$$

iii. Approximate the solution

$$\hat{u}(x, t, y) = \sum_i u_i(x, t) \psi_i(y)$$

- Calculate the coefficients,  $u_i(x, t)$ , by Galerkin projection.

It is possible to describe any random variable  $u(v) \in L_2(\Omega, \mathcal{P})$  as

$$\begin{aligned} u(v) &= u_0 H_0 \\ &+ \sum_{i=1}^{\infty} u_i H_1(y_i(v)) \\ &+ \sum_{i=1}^{\infty} \sum_{k=1}^i u_{ik} H_2(y_i(v), y_k(v)) \\ &+ \sum_{i=1}^{\infty} \sum_{k=1}^i \sum_{j=1}^k u_{ikj} H_3(y_i(v), y_k(v), y_j(v)) + \dots \end{aligned}$$

The multi-dimensional Hermite polynomial is denoted by  $H_n$ . Alternatively expressed as

$$u(y) \equiv u(y_1(v), \dots, y_d(v)),$$

the approximation can alternatively be expressed as finite-dimensional uncertainty. In plainer language, we say that

$$u(y(v)) = \sum_{i=0}^{\infty} u_i \psi_i(y(v)) = \sum_{i=0}^{\infty} u_i \psi_i(y)$$

where  $\psi_i(y)$  is a multi-dimensional Hermite polynomial. The basis  $\{\psi_i(y)\}_{i=0}^{\infty}$  is a complete basis in  $L_2(\mathbb{R}^d, \mathcal{P}_y)$ , i.e.,

$$\mathcal{S} = \text{Span}\{\psi_0(y), \psi_1(y), \dots\} = L_2(\mathbb{R}^d, \mathcal{P}_y)$$

A finite order approximation

$$\hat{u}(y) = \sum_{i=0}^P u_i \psi_i(y)$$

corresponds to a  $p$ -th (total) order approximation of  $u(y)$  in

$$\mathcal{S}_p = \text{Span}\{\psi_0(y), \psi_1(y), \dots, \psi_p(y)\} \subset \mathcal{S}$$

where the generalized Fourier coefficients  $u_i$  are obtained by

$$u_i = \langle u \psi_i \rangle / \langle \psi_i^2 \rangle$$

The expansion converges in a mean-square sense

$$\lim_{p \rightarrow \infty} \langle (u - \hat{u})^2 \rangle = 0$$

In terms of computation, the representation

$$\langle f \rangle = \frac{1}{(2\pi)^{\frac{n}{2}}} \int_{-\infty}^{\infty} f(\xi) e^{-\frac{|\xi|^2}{2}} d\xi,$$

By illustrating the resolution  $u(s, x, w)$  as

$$u(s, x, v) = \sum_{i=0}^P u_i(s, x) \psi_i(\xi)$$

Extension of the solution

$$\tilde{u}(x, t, y) = \sum_{j=0}^P u_j(x, t) \psi_j(y)$$

Galerkin projection on  $\mathcal{S}_p$ :

$$\begin{aligned} \left\langle \frac{\partial \tilde{u}}{\partial s} + \Gamma(x, t, \cdot; \tilde{u}) - f, \psi_i \right\rangle &= 0 \quad i = 0, 1, \dots, P \\ \langle \mathcal{C}(x, t, \cdot; \hat{u}) - g, \psi_i \rangle &= 0 \quad i = 0, 1, \dots, P \\ \langle \mathcal{K}(x, 0, \cdot; \hat{u}) - h, \psi_i \rangle &= 0 \quad i = 0, 1, \dots, P. \end{aligned}$$

### 9 Solutions of stochastic Lotka-Volterra system

The Lotka-Volterra system:

$$\begin{aligned} u'(s, x, v) &= u(s, x, v)(a - bv(s, x, v)) \\ &= u(s, x, v)a - bu(s, x, v)v(s, x, v), \end{aligned}$$

$$\begin{aligned} v'(s, x, v) &= v(s, x, v)(-c + du(s, x, v)) \\ &= -cv(s, x, v) + du(s, x, v)v(s, x, v), \quad (14) \end{aligned}$$

where  $a, b, c, d$  are constants.

We have that:

$$\begin{aligned} u(s, x, v) &= \sum_{i=0}^M u_i(s, x) \psi_i(\xi(v)), v(s, x, v) \\ &= \sum_{j=0}^M v_j(s, x) \psi_j(\xi(v)) \end{aligned}$$

$$a(v) = \sum_{i=0}^M a_i \psi_i(\xi(v)), \quad b(v) = \sum_{i=0}^M b_i \psi_i(\xi(v)),$$

$$c(v) = \sum_{i=0}^M c_i \psi_i(\xi(v)), \quad d(v) = \sum_{i=0}^M d_i \psi_i(\xi(v))$$

Writing these in (14), we obtain the following system:

$$\begin{aligned} & \sum_{i=0}^M \frac{\partial u_i}{\partial s} \psi_i \\ &= \sum_{i=0}^M \sum_{j=0}^M u_i(s, x) \psi_i a_j \psi_j \\ & - \sum_{j=0}^M \sum_{i=0}^M \sum_{k=0}^M b_j \psi_j u_i(s, x) \psi_i v_k(s, x) \psi_k \\ & \sum_{j=0}^M \frac{\partial v_j}{\partial s} \psi_j \\ &= - \sum_{i=0}^M \sum_{j=0}^M c_i \psi_i v_j(s, x) \psi_j \\ & + \sum_{j=0}^M \sum_{i=0}^M \sum_{k=0}^M d_j \psi_j u_i(s, x) \psi_i v_k(s, x) \psi_k \end{aligned}$$

$$\begin{aligned} & \frac{\partial u_m}{\partial s} \\ &= \sum_{i=0}^M \sum_{j=0}^M \frac{\langle \psi_m \psi_i \psi_j \rangle}{\langle \psi_m^2 \rangle} u_i(s, x) a_j \\ & - \sum_{j=0}^M \sum_{i=0}^M \sum_{k=0}^M \frac{\langle \psi_m \psi_j \psi_i \psi_k \rangle}{\langle \psi_m^2 \rangle} b_j u_i(s, x) v_k(s, x) \end{aligned}$$

$$\begin{aligned} & \frac{\partial v_m}{\partial s} \\ &= - \sum_{i=0}^M \sum_{j=0}^M \frac{\langle \psi_m \psi_i \psi_j \rangle}{\langle \psi_m^2 \rangle} c_i v_j(s, x) \\ & + \sum_{j=0}^M \sum_{i=0}^M \sum_{k=0}^M \frac{\langle \psi_m \psi_j \psi_i \psi_k \rangle}{\langle \psi_m^2 \rangle} d_j u_i(s, x) v_k(s, x) \end{aligned}$$

$$\begin{aligned} & \frac{\partial u_m}{\partial s} \\ &= \frac{1}{\langle \psi_m^2 \rangle} \sum_{i=0}^M \sum_{j=0}^M u_i(s, x) a_j e_{mij} \\ & - \frac{1}{\langle \psi_m^2 \rangle} \sum_{j=0}^M \sum_{i=0}^M \sum_{k=0}^M b_j u_i(s, x) v_k(s, x) e_{mjik} \end{aligned}$$

$$\begin{aligned} & \frac{\partial v_m}{\partial s} \\ &= - \frac{1}{\langle \psi_m^2 \rangle} \sum_{i=0}^M \sum_{j=0}^M c_i v_j(s, x) e_{mij} \\ & + \frac{1}{\langle \psi_m^2 \rangle} \sum_{j=0}^M \sum_{i=0}^M \sum_{k=0}^M d_j u_i(s, x) v_k(s, x) e_{mjik} \end{aligned}$$

where  $m = 0, 1, 2, \dots, N$ ,  $e_{mij} = \langle \psi_m \psi_i \psi_j \rangle$ ,  $e_{mjik} = \langle \psi_m \psi_j \psi_i \psi_k \rangle$ .

### 10 Numerical Solution of Stochastic Benney Equation

The Benney equation is defined as follows:

$$u_s(s, x) + (u^n)_x(s, x) + u_{xx}(s, x) + \mu u_{xxx}(s, x) + u_{xxxx}(s, x) = 0, \quad (15)$$

where  $\mu$  is a constant term. We will take  $n = 2$  and consider the stochastic Benney equation. Stochastic Benney equation (15) can be expressed as:

$$u_s(s, x, v) + 2u(s, x, v)u_x(s, x, v) + u_{xx}(s, x, v) + \mu(s, v)u_{xxx}(s, x, v) + u_{xxxx}(s, x, v) = 0,$$

with  $u(0, x, v) = u^0(x, v)$ . By writing

$$\begin{aligned} u(s, x, v) &= \sum_{i=0}^M u_i(s, x) \psi_i(\xi(v)), \mu(v) \\ &= \sum_{i=0}^M \mu_i \psi_i(\xi(v)), \\ u(s, x, v) &= \sum_{i=0}^M u_i(s, x) \psi_i(\xi(v)), \\ u^0(x, v) &= \sum_{i=0}^M u_i^0(x) \psi_i(\xi(v)). \end{aligned}$$

Thus, we write the equation (15)

$$\begin{aligned} & \sum_{i=0}^M \frac{\partial u_i}{\partial s} \psi_i + 2 \sum_{i=0}^M \sum_{j=0}^M u_j \psi_j \frac{\partial u_i}{\partial x} \psi_i + \sum_{i=0}^M \frac{\partial^2 u_i}{\partial x^2} \psi_i \\ & + \sum_{i=0}^M \sum_{j=0}^M \mu_j \psi_j \frac{\partial^3 u_i}{\partial x^3} \psi_i \\ & + \sum_{i=0}^M \frac{\partial^4 u_i}{\partial x^4} \psi_i = 0 \end{aligned}$$

with the initial condition

$$\sum_{i=0}^M u_i(0, x) \psi_i = \sum_{i=0}^M u_i^0(x) \psi_i.$$

Therefore,

$$\begin{aligned} & \frac{\partial u_k}{\partial s} + 2 \sum_{i=0}^M \sum_{j=0}^M \frac{\langle \psi_k \psi_j \psi_i \rangle}{\langle \psi_k^2 \rangle} u_j \frac{\partial u_i}{\partial x} + \frac{\partial^2 u_k}{\partial x^2} \\ & + \sum_{i=0}^M \sum_{j=0}^M \frac{\langle \psi_k \psi_j \psi_i \rangle}{\langle \psi_k^2 \rangle} \mu_j \frac{\partial^3 u_i}{\partial x^3} \\ & + \frac{\partial^4 u_k}{\partial x^4} = 0. \end{aligned}$$

$$\begin{aligned} & \frac{\partial u_k}{\partial s} + \frac{2}{\psi_k^2} \sum_{i=0}^M \sum_{j=0}^M u_j \frac{\partial u_i}{\partial x} e_{kji} + \frac{\partial^2 u_k}{\partial x^2} \\ & + \frac{1}{\langle \psi_k^2 \rangle} \sum_{i=0}^M \sum_{j=0}^M \mu_j \frac{\partial^3 u_i}{\partial x^3} e_{kji} \\ & + \frac{\partial^4 u_k}{\partial x^4} = 0. \end{aligned}$$

### 11 Numerical Simulations

We have demonstrated the suitability of the polynomial chaos approach for both Benney equations and Lotka-Volterra systems.

Figures 1a-1b show numerical simulations for Eq. (14).  
 Figures 2a-2d show numerical simulations for Eq. (15).

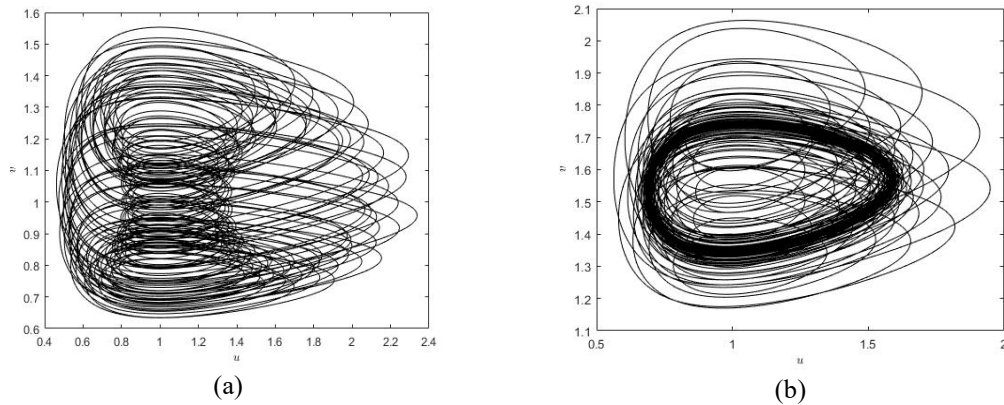


Figure 1. Numerical simulation for Eq. (14).

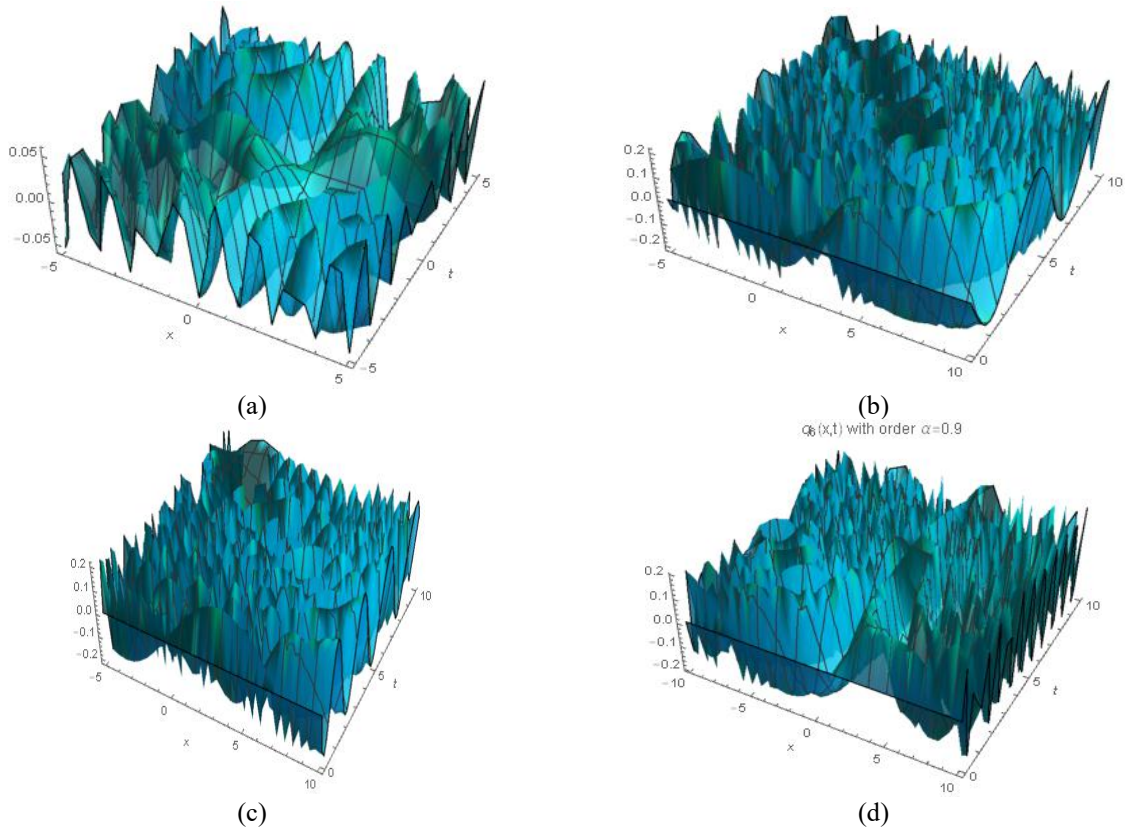


Figure 2. Numerical simulation for Eq. (15).

### 12 Conclusion and Outlook

The stochastic Galerkin and polynomial chaos methods are the type of computational techniques that can be considered as some of the types of undetermined coefficients methods. The underlying and main idea of these methods is to express the unknown function as a series including some unknown coefficients format and determine those coefficients eventually. In the stochastic Galerkin methods, the resulting system is transformed into a linear system of finite element matrix equations, a kind of weighted residual approach. The solutions to these matrix equations are found by highly efficient computing

methods. These matrix equations consist of a row vector made up of what are known as basis functions on a  $L^2$ -length space element (interval). Note that in the weighted residual method, the basis functions we use in this study serve as the weight functions. Polynomial chaos methods work at some probability spaces and are quite like Galerkin methods and can be considered as special cases of Galerkin methods. Polynomial chaos expansions, the series is written in terms of some special series such as the Hermitian series as a different case from the Galerkin method.

In this paper, we investigated if numerical solution techniques of the Galerkin type could be used for the

approximations of fractional-stochastic models. One of the main advantages of the Galerkin-type undetermined coefficients method is that this method is a highly efficient numerical method besides its ease of use. The downside of using these methods is that these methods require working in probability space, and in high-dimensional spaces, this can be a bit of a problem in terms of CPU costs.

The effects of fractional-order operators, fractional Brownian motion, and Gaussian white noise were studied. We also investigated how well the Polynomial Chaos approach worked for approximating solutions for the Benney and stochastic LV systems. Based on computational studies, it is possible to develop a strong and highly efficient use of Galerkin-type approaches. We will be dealing with fractional-stochastic equations involving Levy and Poisson jumps uncertainty in the future development of our study endeavor. We will look into the use of numerical techniques based on random walks in conjunction with Galerkin methods in future studies as an extension of the present work.

### Declaration

Ethics committee approval is not required.

### References

- [1] Baleanu, D., Diethelm, K., Scalas, E., & Trujillo, J.J. (2012). *Fractional Calculus: Models and Numerical Methods*, World Scientific Publishing.
- [2] Özüpak, Y. (2023). Design and Analysis of Permanent Magnet DC Machines with FEM Based ANSYS-Maxwell, *International Journal of Innovative Engineering Applications*, 7(1), 7-12.
- [3] Cavlak Aslan, E., & Gürgöze, L. (2022). Soliton and Other Function Solutions of The Potential KdV Equation with Jacobi Elliptic Function Method, *International Journal of Innovative Engineering Applications*, 6(2), 183-188.
- [4] Dung, N.T. (2013). Fractional Stochastic Differential Equations with Applications to Finance, *Journal of Mathematical Analysis and Applications*, 397(1), 334-348.
- [5] Rihan, A.F., Rajivganthi, C., & Muthukumar, P. (2017). Fractional Stochastic Differential Equations with Hilfer Fractional Derivative: Poisson Jumps and Optimal Control, *Discrete Dynamics in Nature and Society*, Article ID 5394528.
- [6] Klebaner, F. C., & Liptser, R. (2001). Asymptotic analysis and extinction in a stochastic Lotka-Volterra model, *The Annals of Applied Probability*, 11(4), 1263-1291.
- [7] Kinoshita, S. (2013). 1-Introduction to Nonequilibrium Phenomena *Pattern Formations and Oscillatory Phenomena*, 1-59.
- [8] Zakharov, V. E. (1981). On the Benney equations, *Physica D: Nonlinear Phenomena*, 3(1-2), 193-202.
- [9] Pellegrini, G. (2014). *Polynomial Chaos Expansion with applications to PDEs* (Master dissertation, University of Verona).
- [10] Nualart, D. (2006). Fractional Brownian motion. The Malliavin Calculus and Related Topics. Probability, its applications. *Springer*, Berlin, Heidelberg.
- [11] Mahmud, A.A., Muhamad, K.A., Tanriverdi, T., & Baskonus, H.M. (2024). An investigation of Fokas system using two new modifications for the trigonometric and hyperbolic trigonometric function methods, *Optical and Quantum Electronics*, 56:717.
- [12] Mahmud, A. A., Tanriverdi, T., Muhamad, K. A., & Baskonus, H. M. (2023). Characteristic of ion-acoustic waves described in the solutions of the (3+1)-dimensional generalized Korteweg-de Vries-Zakharov-Kuznetsov equation, *Journal of Applied Mathematics and Computational Mechanics*, 22, 2, 36-48.
- [13] Mahmud, A. A., Baskonus, H. M., Tanriverdi, T., & Muhamad, K. A. (2023). Optical Solitary Waves and Soliton Solutions of the (3+1)-Dimensional Generalized Kadomtsev–Petviashvili–Benjamin–Bona–Mahony Equation, *Partial Differential Equations*, 63, 1085-1102.
- [14] Baskonus, H. M., Mahmud, A. A., Muhamad, K. A., & Tanriverdi, T. (2022). A study on Caudrey–Dodd–Gibbon–Sawada–Kotera partial differential equation, *Mathematical Methods in the Applied Sciences*.
- [15] Tanriverdi, T., Baskonus, H. M., Mahmud, A. A., & Muhamad, K. A. (2021). Explicit solution of fractional order atmosphere-soil-land plant carbon cycle system, *Ecological Complexity*, 48, 100966.



## INVESTIGATION OF FLEXURAL BEHAVIOR OF CARBON FIBER BEAMS

Mustafa Albayrak<sup>\*1</sup> 

<sup>1</sup>Inönü University, Malatya OSB Vocational School, Department of Machinery and Metal Technologies, Malatya, Turkey

### Abstract

Original scientific paper

In this study, beams with hat profiles were produced. For this purpose, carbon fiber woven fabrics were preferred as reinforcement elements. Afterwards, bending test was applied to these composite beams. As a result of the experiments, displacement-force graphs were obtained on the moving cylinder. In the numerical analysis section, Hashin damage criterion was preferred for damage initiation. "Continuous Damage Mechanics (CDM)" and "Material Property Degradation (MPDG)" methods are defined in the program for damage progression. In the bending test, crushing damage was observed as the dominant damage on the surface of the specimen in contact with the moving cylinder under load. Fiber breakage along with fiber tensile damage was observed on the surfaces in contact with the fixed support rollers. It was observed that the experimental results were closer to each other with the MPDG method. The convergence rate of experimental and numerical data was determined as 89.55%.

**Keywords:** Carbon fiber, continuum damage mechanics, hat-shape profile, material property degradation.

### 1 Introduction

Composite structures; It has the advantages of high specific strength, high specific stiffness and good designability. Recently, they have been widely preferred in the structural design of civil and military aircraft. Composite beams with hat-shaped profiles are one of the important structural elements that make up the main body of aircraft in the aviation industry (Figure 1). These beams have a significant impact on the strength and post-buckling bearing capacity of the hull. During use, these beams carry radial forces as well as lateral forces that cause the wing or fuselage to bend. Conducting a sound damage analysis of reinforced panels can help experts in this field design wing and fuselage integrity.

When the tests and analyzes performed on composite structures in general are examined: Li et al. (2022) experimentally performed a four-point bending test on flat profiles for numerical verification in Abaqus. Afterwards, they developed a user-defined subroutine and proposed a theoretical model. [1]. Bai et al. (2018) examined the buckling behavior and damage situations of hardened carbon fiber reinforced composite panels with I-profile under compressive load [2]. Alkhatib et al. (2020) experimentally and numerically examined the energy absorption capacity and crushing behavior of composite corrugated pipes under quasi-static axial shear crushing loading. Corrugated pipes were manufactured by wet filament winding process using Kevlar (KFRP) and carbon (CFRP) fiber reinforced composites. They carried out experimental and numerical crush tests on corrugated pipes [3]. Cherniaev et al. (2018) used the LS-DYNA

program for crush simulations of CFRPs. They performed comprehensive calibration of all material models for correlation with experiments. Three material models for this; They used MAT-54, MAT-58 and MAT-262. They reported that MAT-54 provided reasonable agreement with experimental data. They estimated the non-physical damage modes and maximum force values of MAT-58 [4]. Candido et al. (2022) established a connection between longitudinal T-profile reinforced composites and flat panels using an adhesive film layer and performed an experimental fracture analysis on the reinforced structure they obtained [5]. Dogan and Arıkan (2017) produced sandwich composites by placing PVC foam between the shell surfaces they produced from epoxy (thermosetting) and polypropylene (thermoplastic) polymer composites reinforced with E-glass. They examined the behavior of the sandwich composite panels they obtained under different impact energies [6]. Kosztowny et al. (2021) produced one-piece textile composite panels using two-dimensional and triaxial braided composites. Afterwards, they examined the buckling behavior by applying axial compression tests on the panels [7]. Kurşun et al. (2016) experimentally and numerically investigated the effect of impactor geometry on impact performance by performing low-speed impact tests on aluminum sandwich composite plates, which they produced by using a low-density polyethylene core between two aluminum plates [8]. Natarajan et al. (2023) investigated the suitability of S-Glass/carbon fiber reinforced polymer composite for submarine hull exposed to hydrostatic pressure. For this purpose, they experimentally determined the mechanical properties of S Glass/carbon fiber reinforced polymer

\*Corresponding author.

E-mail address: [mustafaalbayrak@inonu.edu.tr](mailto:mustafaalbayrak@inonu.edu.tr) (M. Albayrak)

Received 28 March 2024; Received in revised form 30 May 2024; Accepted 07 June 2024

2587-1943 | © 2024 IJIEA. All rights reserved.

Doi: <https://doi.org/10.46460/ijiea.1460748>

composite and compared the composite with many metallic materials used in submarine hulls [9]

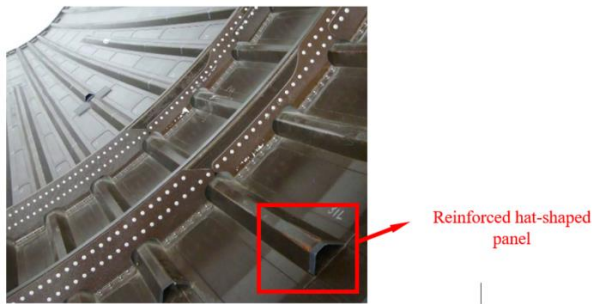


Figure 1. Reinforced hat-shaped panel in aircraft structures (Fasulo vd., 2022) [10].

When the studies in the literature are examined; When mechanical tests performed on composites with curved or flat surfaces are examined, it is seen that the focus is generally on dynamic impact tests [6,8], static pressure [3] and buckling [7] tests. A clear understanding of the damage mechanisms of structures is important in the design of flexural resistant structures.

In this study, unlike the literature, for the first time. Hat profile beams were produced by applying resin to layered carbon fiber woven fabrics under vacuum, and the mechanical behavior of the obtained specimens under bending load was examined experimentally and numerically. In the numerical part, the problem was

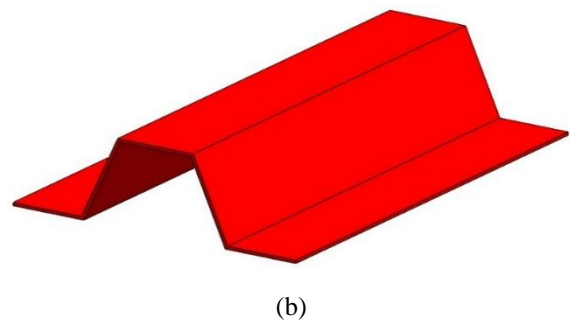
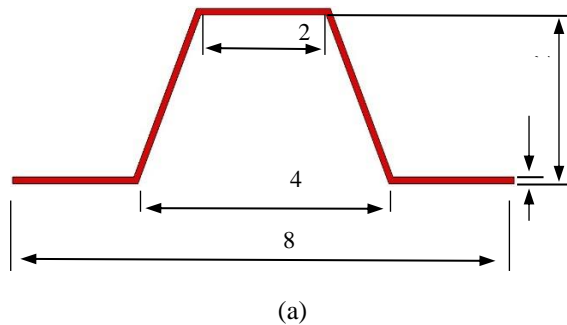


Figure 2. Hat-shaped beam a) dimensions b) solid model.

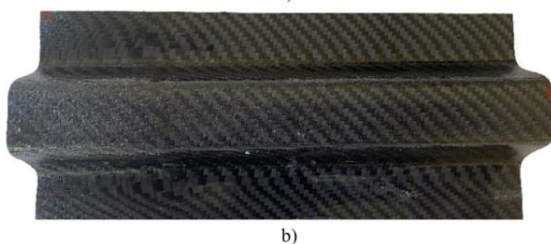
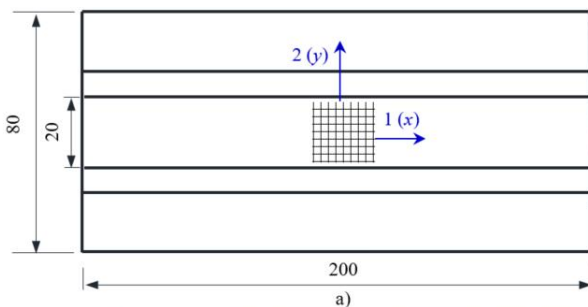


Figure 3. a) geometry dimensions of the hat-shaped profile beam. b) specimen obtained after production.

solved according to MPDG and CDM methods and the convergence to the experimental results was shown. As a result, experimental and numerical maximum contact forces are compared and presented along with force-displacement graphs.

## 2 Material Method

To perform bending tests on carbon fiber composite beams with a hat-shaped profile, carbon fiber composite specimens consisting of 4 layers with a thickness of 1 mm were manufactured. The profile beam dimensions are given in Figure 2. Afterwards, the beams obtained were cut in a 200 mm long wet marble cutting machine and made ready for testing. Details of the design are given in Figure 3. In this method, the mold release agent was first applied to the molds and allowed to dry. Subsequently, 245 grams per square meter of twill 2x2 woven type carbon fiber woven fabric were laid on the steel mold. Peel-ply was laid on the fabrics and adhesion was prevented with the infusion mesh that was added later. Finally, vacuum nylon was laid and the necessary tightness control was carried out. Subsequently, a mixture of MGS L160 epoxy and H160 hardener, with a weight ratio of 100:20, was impregnated on the fabrics via the vacuum infusion method. Following a 24-hour curing period, the test specimens were prepared by removing the material from the mold and cutting it into 200 mm lengths.

### 2.1 Three-Point Bending Test Method

Details of the ASTM D790 [11] standards test method are given in Figure 4. Here the distance between fixed supports is 180 mm

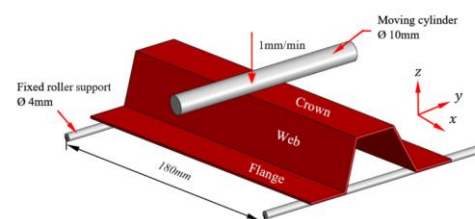
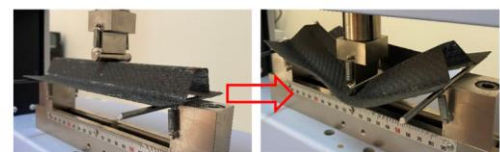


Figure 4. Test dimensions.

### 2.2 Numerical Analysis

In the numerical part, the analyzes were performed in Ansys Workbench 2020R1. Composite beam, moving and fixed cylinders were modeled in Solidworks program and transferred to Workbench program. 8-node element type was preferred and Multizone mesh type was used for finite element separation. Figure 5 shows the number of elements obtained after separation into finite elements of different sizes and the change in the maximum contact force accordingly. As seen in the graph, the maximum contact force remained constant after the number of elements reached 5820. Therefore, it was determined that the optimum number of elements was 5820 and the number of nodes was 33175.

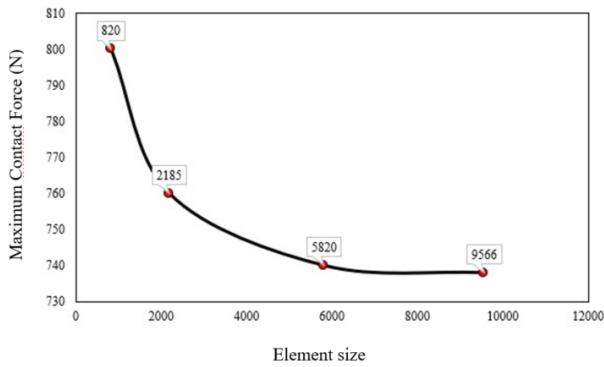


Figure 5. Mesh optimization.

#### 2.2.1 Damage Model

In progressive damage analysis, the linear elastic orthotropic material properties of the material, the damage initiation criterion, the damage progression method, and the strength limits of the material must be defined in the program, respectively. Orthotropic material properties of carbon fiber are presented in Table 1.

Table 1. Mechanical properties of carbon fiber reinforced composite [12].

Symbol	Properties	Value	Unit
$\rho$	Density	1500	kg/m <sup>3</sup>
$E_x, E_y$	Elasticity modulus $x$ and $y$ direction	43.7	GPa
$E_z$	Elasticity modulus $z$ direction	14.57	GPa
$\nu$	Poisson's ratio	0.21	-
$G_{xy}$	Shear modulus in $xy$ plane	14.18	GPa
$G_{yz}$	Shear modulus in $yz$ plane	14.65	GPa
$G_{zx}$	Shear modulus in $zx$ plane	14.65	GPa

In order to define the beginning of damage in progressive damage analysis, Hashin damage initiation criteria must be entered into the program. The hash initiation criteria include the following four damage initiation modes. Here the damage initiation indices are  $I_f^t$ ;  $I_f^c$ ;  $I_m^t$  and  $I_m^c$  represent fiber tensile, fiber compression, matrix tensile and matrix compression damage, respectively. When any of these indices exceeds 1, damage onset occurs. Four different damage cases belonging to the Hashin criteria are evaluated according to the following formulas in Equations (1)-(4).

Fiber failure for tension ( $\sigma_{xx} \geq 0$ ):

$$I_f^t = \left(\frac{\sigma_{xx}}{F_{xt}}\right)^2 + \alpha \left(\frac{\sigma_{xy}}{F_6}\right)^2 \tag{1}$$

Fiber failure for compression ( $\sigma_{xx} < 0$ ):

$$I_f^c = \left(\frac{\sigma_{xx}}{F_{xc}}\right)^2 \tag{2}$$

Matrix failure for tension ( $\sigma_{yy} \geq 0$ ):

$$I_m^t = \left(\frac{\sigma_{yy}}{F_{yt}}\right)^2 + \left(\frac{\sigma_{xy}}{F_6}\right)^2 \tag{3}$$

Matrix failure for compression ( $\sigma_{yy} < 0$ ):

$$I_m^c = \left(\frac{\sigma_{yy}}{2F_4}\right)^2 + \left[\left(\frac{F_{yc}}{2F_4}\right)^2 - 1\right] \frac{\sigma_{yy}}{F_{yc}} + \left(\frac{\sigma_{xy}}{F_6}\right)^2 \tag{4}$$

Here  $\sigma_{ij}$  are the components of the stress tensor;  $F_{xt}$  and  $F_{xc}$  are the tensile and compressive strengths of a sheet in the longitudinal (fiber) direction;  $F_{yt}$  and  $F_{yc}$  are the tensile and compressive strengths in the transverse direction;  $F_6$  and  $F_4$  are in-plane and inter-layer shear strengths.  $\alpha$  is the contribution of the in-plane shear stress according to this criterion and is taken as 0 in this study. In order to evaluate the damage initiation criteria in the composite structure, it is necessary to define the maximum stresses or strains that the material can tolerate before damage occurs. Stress limit values are presented in Table 2.

Table 2. Orthotropic stress limit values of carbon fiber composite [12].

Symbol	Properties	Value	Unit
$X_T$	Tensile strength in $X$ direction	859	MPa
$Y_T$	Tensile strength in $Y$ direction	859	MPa
$Z_T$	Tensile strength in $Z$ direction	859	MPa
$X_C$	Compression strength in $X$ direction	109.6	MPa
$Y_C$	Compression strength in $Y$ direction	109.6	MPa
$Z_C$	Compression strength in $Z$ direction	373.5	MPa
$S_{XY}$	Shear strength in plane $X - Y$	108.2	MPa
$S_{YZ}$	Shear strength in plane $Y - Z$	105.5	MPa
$S_{XZ}$	Shear strength in plane $X - Z$	105.5	MPa

#### 2.2.2 Damage Evolution

MPDG and CDM methods were used for damage progression. In the MPDG method, when the breaking stress and strain are reached for the fiber and matrix components, the rate of decrease in hardness is determined separately for both components. In the CDM method, the material stiffness is gradually reduced. The stiffness reductions used for the four damage cases in the study are given in Table 3.

**Table 3.** Stiffness reduction coefficients for the MPDG method.

Properties	Value
Tensile fiber stiffness reduction	0.46
Compressive fiber stiffness reduction	0.46
Tensile Matrix Stiffness Reduction	0.4
Compressive Matrix Stiffness Reduction	0.4

### 3 Results and Discussion

Three-point bending tests were performed on specimens with hat-shaped profiles made of carbon fiber reinforced composites. In the numerical analysis section, the problem was solved and evaluated according to both Continuous Damage Mechanics (CDM) and Material Property Degradation (MPDG) methods. In both methods, the proximity of the composite structure to the damage behavior and its effect on the damage load were determined. Figure 6 shows the load-displacement curve of the specimen. The test process consists of five stages: In the first stage, the moving cylinder contacted the specimen and accordingly the reaction force values increased. At this point, elastic deformation occurred in the specimen. It was observed that the load did not increase linearly at this stage. This situation is caused by production errors and geometric discontinuities on the upper surface of the hat-shaped profile. II. With the small deformation that occurred in the specimen at this stage, the slope of the graph started to decrease further and reached the maximum damage force. Afterwards, it was observed that as the load was increased, matrix cracks spread in the structure and as a result, delamination damage occurred.

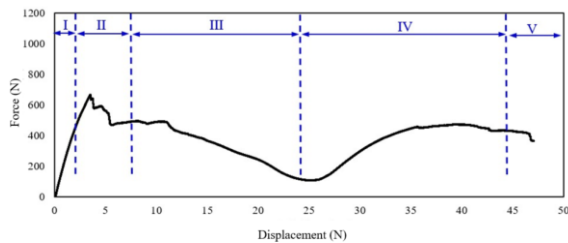


**Figure 6.** Force-displacement graph.

The reflection of this situation on the graph is that there are sudden and gradual decreases in load after the maximum load. III. At this stage, it was observed that the connection plates of the specimen started to open by moving in the "y" direction. Therefore, the angles made with the top surface of the connection plates that will resist the load have increased and their resistance has decreased. As a result, the load continued to decrease in an inclined manner. IV. In this stage, the moving cylinder is surrounded by the top surface of the beam with partially collapsed connecting plates. By compressing these surfaces with the cylinder that continued to move, the load-displacement curve increased slightly and then made it move horizontally. In the last stage, the moving cylinder reached its maximum displacement value. Large tensile damages were observed on the surface of the specimen below the top area, and with the progression of the damage, they turned into permanent fiber breaks. Figure 7 shows the force-displacement graph of the specimen. When the experimental graph is examined, it is evaluated that the carbon fiber beam exhibits non-linear material

behavior. However, it was observed that the slope of the force-displacement curve decreased after the experimental yield point. In the analysis section, MPDG and CDM methods were preferred for Hashin damage initiation criterion and subsequent damage progression. Obtained experimental results were compared with analysis solutions.

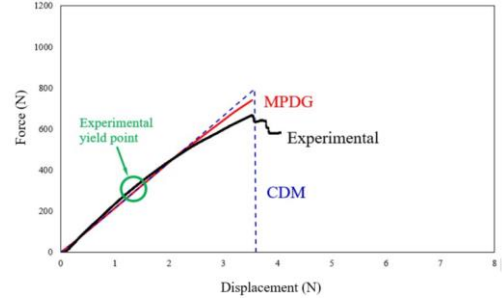


**Figure 7.** Experimental and numerical comparison of load-displacement graph.

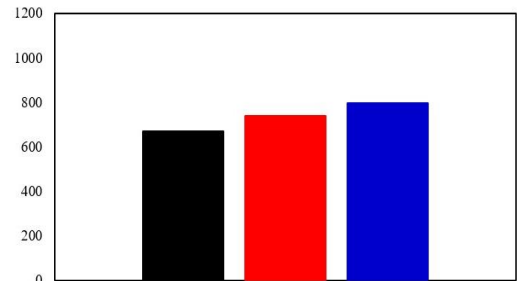


**Figure 8.** Experimental and numerical comparison of maximum load values.

According to the CDM method, material stiffness is gradually reduced and progress ends when catastrophic damage is reached [13]. According to the graph, it can be seen that the numerical data and experimental results are close in the elastic region. According to the CDM method, the sample suffered ultimate damage at a load of 790 N and was displaced by approximately 3.55 mm in case of ultimate damage. When the solution made with the MPDG method was examined, it was seen that the material hardness was gradually reduced. It has been observed that as the amount of displacement increases, especially in the plastic region after the yield limit, the slope begins to decrease and exhibits a behavior closer to the experimental graph. Therefore, this method comes to the fore in finite element analyzes. Zachariah.S.A., et al. They carried out experimental testing and numerical verification to investigate the in-plane tensile properties of carbon/aramid hybrid polymer composite. In their analysis with the MPDG method, they found that the composite material showed binaristic behavior and provided a slope closer to the experimental results [14]. Maximum contact forces are evaluated in Figure 8. The maximum contact force value obtained experimentally was determined as 670 N. In the MPDG and CDM methods, these values are 740N and 794N, respectively. When the convergence rates of experimental and numerical data are compared, a convergence rate of 89.55% was obtained in the solution with the MPDG method and approximately 81.49% in the solution with the CDM method.

## 4 Conclusion

Carbon fiber composite beams with hat-shaped profiles were produced. Three-point bending was performed on the obtained specimens. The results were compared and summarized as follows.

- The convergence rate of the MPDG method selected for damage progression to experimental results was determined to be approximately 89.55%. In the CDM method, this rate was determined as 81.49%.
- It has been determined that the MPDG method is much better than CDM. It was observed that the force-displacement graphs exhibited close behavior, especially when compared to the experimental results.
- Compression and crushing damage were seen more clearly, especially on the crown surface of the specimens. On the lower surface, mainly fiber shrinkage and fiber breakage damages were observed.
- It has been concluded that numerical modeling of composites with hat-shaped profiles, which are relatively difficult to produce experimentally, without the need for production, and solving them with the MPDG method by selecting the Hashin initial damage criterion, can give designers an idea about the mechanical behavior of composites under bending load.

## Declaration

Ethics committee approval is not required.

## References

- [1] Li, B., Gong, Y., Gao, Y., Hou, M., & Li, L. (2022). Failure analysis of hat-stringer-stiffened aircraft composite panels under four-point bending loading. *Materials*, 15(7), 2430.
- [2] Bai, R., Bao, S., Lei, Z., Liu, C., Chen, Y., Liu, D., & Yan, C. (2018). Experimental study on compressive behavior of I-stiffened CFRP panel using fringe projection profilometry. *Ocean Engineering*, 160, 382-388.
- [3] Alkhatib, F., Mahdi, E., & Dean, A. (2020). Crushing response of CFRP and KFRP composite corrugated tubes to quasi-static slipping axial loading: experimental investigation and numerical simulation. *Composite Structures*, 246, 112370.
- [4] Cherniaev, A., Butcher, C., & Montesano, J. (2018). Predicting the axial crush response of CFRP tubes using three damage-based constitutive models. *Thin-Walled Structures*, 129, 349-364.
- [5] Candido, G. M., Sales, R. D. C. M., Arbelo, M. A., & Donadon, M. V. (2022). Failure analysis in secondary bonded T-stiffened composite panels subject to cyclic and quasi-static compression loading. *International Journal of Adhesion and Adhesives*, 118, 103199.
- [6] Dogan, A., & Arikan, V. (2017). Low-velocity impact response of E-glass reinforced thermoset and thermoplastic based sandwich composites. *Composites Part B: Engineering*, 127, 63-69.
- [7] Kosztowny, C. J., & Waas, A. M. (2021). Postbuckling response of unitized stiffened textile composite panels: Experiments. *International Journal of Non-Linear Mechanics*, 137, 103814.
- [8] Kurşun, A., Şenel, M., Enginsoy, H. M., & Bayraktar, E. (2016). Effect of impactor shapes on the low velocity impact damage of sandwich composite plate: Experimental study and modelling. *Composites Part B: Engineering*, 86, 143-151.
- [9] Natarajan, E., Freitas, L. I., Santhosh, M. S., Markandan, K., Al-Talib, A. A. M., & Hassan, C. S. (2023). Experimental and numerical analysis on suitability of S-Glass-Carbon fiber reinforced polymer composites for submarine hull. *Defence Technology*, 19, 1-11.
- [10] Fasulo, G., Vitiello, P., Federico, L., & Citarella, R. (2022). Vibro-Acoustic Modelling of Aeronautical Panels Reinforced by Unconventional Stiffeners. *Aerospace*, 9(6), 327.
- [11] A. E883-02 (2003). Standard Guide for iTeh Standards iTeh Standards Document Preview, vol. 03, pp. 1-6.
- [12] Albayrak, M., Kaman, M. O., & Bozkurt, I. (2023). Experimental and numerical investigation of the geometrical effect on low velocity impact behavior for curved composites with a rubber interlayer. *Applied Composite Materials*, 30(2), 507-538.
- [13] Apruzzese, P., & Falzon, B. G. (2007, July). Numerical analysis of complex failure mechanisms in composite panels. In *16th international conference on composite materials, Kyoto, Japan* (pp. 234-246).
- [14] Zachariah, S. A., Shenoy, B. S., & Pai, K. D. (2021). Comprehensive analysis of in-plane tensile characteristics of thin carbon/aramid hybrid composites using experimental and RVE-based numerical study. *Composite Structures*, 271, 114160.



## MOBILE MICRORNAS (MIRNAS) RESPONSIVE TO EXCESS NICKEL IN PUMPKIN (*CUCURBITA MAXIMA L.*)

Guzin Tombuloglu\*<sup>1</sup> 

<sup>1</sup>Department of Biophysics, Institute for Research and Medical Consultations (IRMC), Imam Abdulrahman Bin Faisal University, P.O. Box 1982, Dammam 31441, Saudi Arabia

### Abstract

Original scientific paper

Nickel (Ni) is a toxic heavy metal that inhibits plant growth, development, and reproduction. MicroRNAs (miRNAs) travel from cell to cell or organ to carry messages to regulate gene expression. This study aims to find mobile miRNAs that are Ni-responsive and are present in pumpkin (*Cucurbita maxima* L.) phloem sap. For this purpose, pumpkin seedlings were exposed to Ni (100  $\mu$ M, NiCl<sub>2</sub>), and root, shoot, and phloem-sap specimens were collected at 0 (control), 24, and 48 hours of the treatment. The stem-loop RT-qPCR and stem-loop semi-quantitative RT-PCR methods were used to determine the abundance of 14 miRNAs in the phloem sap. Compared to the control, the abundance of miR160, miR167, miR393, miR397, and miR398 was suppressed in Ni-treated seedlings. The reduction was verified by grafting experiments, revealing that miR167 and miR393 are Ni-responsive and move/travel from the leaf-to-root direction. Those phloem-residential miRNAs potentially play a role in the Ni-response mechanism. This study can help to understand the early response mechanism of plants against excess Ni and lead to identifying miRNA-mediated long-distance communication of plants.

**Keywords:** miRNA, phloem, long-distance communication, nickel, pumpkin.

## BALKABAĞINDA (*CUCURBITA MAXIMA L.*) FAZLA NİKELE YANIT VEREN MOBİL MİKORNA'LAR (MİRNA'LAR)

### Özet

Orijinal bilimsel makale

Nikel (Ni) fazlalığı durumunda, bitki büyümesini, gelişimini ve üremesini engelleyen toksik bir ağır metaldir. MikroRNA'lar (miRNA), gen ekspresyonunu düzenlemek için mesajlar taşımak üzere hücreden hücreye veya organa seyahat eder. Bu çalışma balkabağı (*Cucurbita maxima* L.) floem öz suyunda dolaşan Ni'ye duyarlı mobil miRNA'ları tanımlamayı amaçlamaktadır. Bu amaçla, Ni (100  $\mu$ M, NiCl<sub>2</sub>) uygulanan balkabağı fidelerine ait kök, sürgün ve floem öz suyu örnekleri toplanmıştır. Floem öz suyundaki 14 miRNA'nın ekspresyonunu belirlemek için gövde-ilmek RT-qPCR ve gövde-ilmek yarı-kantitatif RT-PCR yöntemleri kullanıldı. Kontrol ile karşılaştırıldığında, Ni ile muamele edilmiş fidelerde miR160, miR167, miR393, miR397 ve miR398'in miktarının azaldığı tespit edildi. Bu azalma, aşılama deneyleriyle de doğrulanarak, miR167 ve miR393'ün Ni'ye duyarlı olduğu ve yapraktan köke doğru hareket ettiğini ortaya çıkardı. Floemde bulunan bu miRNA'lar, Ni-yanıt mekanizmasında potansiyel olarak rol oynamaktadır. Bu çalışma, bitkilerin fazla Ni'ye karşı erken tepki mekanizmasının anlaşılmasına yardımcı olarak, bitkilerin miRNA aracılı kök-yaprak iletişiminin belirlenmesine yol gösterebilir.

**Anahtar Kelimeler:** miRNA, floem, uzak organ iletimi, nikel, balkabağı.

### 1 Introduction

An RNA-based communication network through phloem has been discovered between plants' distant organs (root-leaf). So far, different RNA types have been found as mobile RNAs, such as viral RNAs, cellular mRNAs, tRNAs, and microRNAs (miRNAs) [1-4]. The existence of mobile miRNAs has been revealed in different plants, such as gourd, lupine, beans, yucca [5], rapeseed [6], apple [3, 7], and pumpkin [8]. They can move along the phloem and reach distant organs/tissues of plants through the mass flow

of water [1-4, 9]. Some mobile RNAs are essential in transcriptional response mechanisms such as nutrient (phosphate, sulfur, and copper) deficiencies. For instance, miR399 was found to be translocated from leaf to root through the phloem upon phosphate deficiency [10-12]. It was also found that phosphate deficiency induces miR169, miR827, and miR2111 in rapeseed (*Brassica napus*) phloem sap [13]. In addition, miR399 has been proven to be a signaling molecule that communicates between leaves and roots via phloem in *Arabidopsis*, pumpkin (*Cucurbita maxima*), and tobacco (*Nicotiana tabacum*) plants [6, 10,

\*Corresponding author.

E-mail address: [guzinkekec@gmail.com](mailto:guzinkekec@gmail.com) (G. Tombuloğlu)

Received 28 May 2023; Received in revised form 07 February 2024; Accepted 13 February 2024

2587-1943 | © 2024 IJIEA. All rights reserved.

Doi: <https://doi.org/10.46460/ijiea.1304404>

14-15]. miR395 and miR398 abundances in phloem sap have increased due to sulfur and copper deficiency, respectively [6, 12, 16-17]. Besides, the expressions of miR397, miR408, and miR857 were found to be increased against copper deficiency [18]. Moreover, grafting experiments showed that miR172, abundantly found in the phloem sap, is associated with plant growth and affects tuber formation in potatoes [19-20].

Nickel (Ni) is the seventeenth essential element for the development and growth of plants. It is involved in the biosynthesis of some bacterial taxa' hydrogenase, carbon monoxide dehydrogenase, and factor F 430 [21]. Another Ni-containing protein is urease, found in jack beans and several plant species. However, it is a potentially hazardous metal, with an average concentration of 20 to 30 mg/kg in soils and occasionally surpassing 10,000 mg/kg (e.g., ultramafic soils) [22-23]. The concentration of Ni in agricultural soils is generally deficient. However, the nickel content of soils composed of ultra-basic igneous rocks such as serpentine varies between 100-5,000 mg Ni/kg [24]. Excess Ni in the plant harms chlorophyll synthesis and lipid metabolism, preventing plant roots from taking other nutrients and causing nutrient deficiencies [25].

This study aims to identify Ni-responsive mobile miRNAs. For this purpose, 14 miRNAs detected in pumpkin's phloem sap were chosen. Their expression at 12 and 24 hours was compared with those of untreated (control) one using stem-loop RT-qPCR and semi-quantitative RT-PCR assays. The mobility of selected miRNAs was verified by grafting assay. This study reveals Ni-responsive mobile miRNAs potentially involved in the long-distance communication of tissues.

## 2 Material and Methods

### 2.1 Plant Growth and Nickel Treatment

The seeds of a pumpkin (*Cucurbita maxima* L., Dill's Atlantic Giant) were surface sterilized by submerging them in a 5% sodium hypochlorite (NaClO) solution for 10 minutes before being washed three times with distilled water (dH<sub>2</sub>O). The filter paper was adjusted into a Petri dish, adding 5 mL of dH<sub>2</sub>O. The seeds were placed between sterile filter papers in the Petri dish (10 cm x 1.5 cm) and kept at room temperature. After seven days, about 80% of the seeds germinated, and root lengths were at least 15 mm long. The seedlings were placed in a hydroponics medium that contained macronutrient solution in mM: 1 NH<sub>4</sub>H<sub>2</sub>PO<sub>4</sub>, 4 Ca(NO<sub>3</sub>)<sub>2</sub>, 2 MgSO<sub>4</sub>, 6 KNO<sub>3</sub>, and micronutrient solution in  $\mu$ M: 0.8 ZnSO<sub>4</sub>, 9 MnCl<sub>2</sub>, 0.3 CuSO<sub>4</sub>, 50 H<sub>3</sub>BO<sub>3</sub>, 25 Fe-EDTA, and 0.02 g MoO<sub>3</sub> (85%) [26]. The plants were grown in a temperature (20-24 °C), humidity (40-60%), and light (6,000 Lux)-controlled growth chamber (WiseCube, Korea). The nutrient solution was kept at a constant pH (5.5) and renewed weekly.

Three-week-old pumpkin seedlings were exposed to 100  $\mu$ M Nickel (NiCl<sub>2</sub>) solution at two different time intervals, 24 h and 48 h. Leaf, root, and phloem sap (PS) samples were harvested from the seedlings (n = 3) exposed to Ni (control (0), 24 h, and 48 h). The tissue samples (root and leaf) were flash-frozen by liquid nitrogen and stored at

-80 °C. The PS samples collected from each plant were kept in ice until RNA isolation.

### 2.2 RNA Isolation from Phloem Sap (PS) and Tissues

The PS exudates were collected using Buhtz et al. [6]'s outlined procedure. For this purpose, the stem of each seedling (n = 3) was cut with a sterile razor blade. To avoid tissue contamination, the first droplets of PS were removed with sterile filter paper from the cut surface. The exudates are then gathered in a pre-chilled tube with 10  $\mu$ l pipette tips every 10 minutes until the PS exudates reach about 25  $\mu$ l.

The RNA was extracted according to Zhang et al. [30] and Chomczynski and Sacchi [27]. Accordingly, the PS and Trizol® LS reagent (Invitrogen) were mixed (1:3) and vortexed thoroughly. The mixture was incubated for five minutes at room temperature. After adding 25  $\mu$ l of chloroform (Merck, Germany), the mixture underwent a 15-sec handshake, incubated for 15 min at room temperature, and cold centrifuged (4 °C) at 12,000 x g for 15 min. The supernatant was mixed with absolute ethanol (Millipore) (1:2) and incubated at -20 °C overnight. After 30 min centrifugation (16,000 x g, 4 °C), the pellet was rinsed with DEPC-treated 70% ethanol (Millipore), dried, and re-suspended with ddH<sub>2</sub>O. The RNA samples were quantified by NanoDrop 2000c UV-Vis spectrophotometer (Thermo Scientific), and kept at -80 °C.

### 2.3 Stem-Loop 1st-Strand cDNA Synthesis

The stem-loop 1<sup>st</sup>-strand cDNA synthesis method was conducted to determine the miRNAs in the PS. For this purpose, 1  $\mu$ l of RT primer (1  $\mu$ M) (Table S1), 30 ng of RNA, 0.5  $\mu$ l of dNTP (10 mM) (Bio-Basic) and DEPC-treated water was mixed to make a total volume of 14  $\mu$ l. The mixture was kept at 65 °C for 5 min and immediately placed on ice. Afterward, 4  $\mu$ l of Buffer (5x), 2  $\mu$ l RiboLock RNase Inhibitor (10 U/ $\mu$ l), 1  $\mu$ l of RevertAid M-MuLV Reverse Transcriptase (200 U/ $\mu$ l), and DEPC-treated water (up to 20  $\mu$ l) were added. The mixture was kept at 16 °C for 30 minutes, and the following reaction conditions were applied: 30 °C 30 sec, 42 °C 45 sec, and 48 °C 1 sec (60 cycles). The enzyme inactivation was performed at 70 °C (5 min), and then the tubes were kept at -20 °C.

### 2.4 Stem-loop Quantitative Reverse Transcription PCR

The stem-loop quantitative RT-PCR method was used to determine the expression level of miRNAs under control and Ni-treated specimens [28-29]. miRNA amplification was performed using SYBR®Premix Ex Taq™ (2 $\times$ ) (Tli RNaseH Plus) kit (Takara, Japan). Accordingly, 1  $\mu$ l (10  $\mu$ M) of miRNA-specific forward and universal primers (Table S1), 2  $\mu$ l of cDNA, 8  $\mu$ l of sterile water, and 10  $\mu$ l of SYBR®Premix Ex Taq™ (2 $\times$ ) mixture were collected in a 0.2 ml PCR tube. A real-time PCR device (Rotor-Gene® PCR, Corbett Research-Qiagen) was used for the reaction settled at 95 °C (2 min), 40 cycles of 95 °C (5 sec), 56 °C (15 sec), and 72 °C (20 sec). Subsequently, the primer specificity was tested by performing a melting

curve analysis (MCA) between 52 and 95 °C (0.5 °C increments/sec).

## 2.5 Semi-quantitative RT-PCR

The expression levels of miRNAs in control and Ni-applied specimens were determined using the semi-quantitative RT-PCR technique. For this purpose, 2 µl cDNA, 2.5 µl 10X buffer, 0.5 µl 10mM dNTP, 1.5 µl 2 mM MgCl<sub>2</sub>, 0.75 µl (10 µM) miRNA specific "forward" and "universal" primers (Table S1), 0.25 µl Taq Polymerase (Fermentas, Thermo Scientific), and 17.75 µl sterile water were mixed. PCR conditions were adjusted as follows: 95 °C (2 min), 30 cycles of 95 °C (5 sec), 56 °C (15 sec), and 72 °C (20 sec). Finally, the polymerization temperature was set at 72°C (7 min) (TECHNE, TC-512 thermal cycler). After the reaction, the PCR products were loaded in a 3% agarose gel using 1x TBE buffer. The gel was visualized under ultraviolet light.

## 2.6 Contamination Analysis

To check for any contamination that might have occurred during the isolation and/or exudation of phloem sap, the existence of *CmPP16* (AF079170) and *RuBisCo* were tested. The *CmPP16* gene, a phloem-specific transcript found in the PS of *Cucurbitaceae* species [30-31], is used as a positive control. In addition, *RuBisCo*, a transcript exclusive to green tissues, was chosen as a negative control to examine any contamination that might have occurred during PS sampling. The leaf and PS RNAs from all tested plants were used for the analyses. First-strand cDNA synthesis was carried out according to Tombuloglu et al. [26]. The transcripts were amplified in a thermal cycler (Techne TC-512, UK) using standard protocols detailed in the previous section. The PCR products were loaded in 2% agarose gel by labeling SafeView® stain and visualized under UV light.

## 2.7 Grafting Experiments

Grafting experiments were conducted to demonstrate and verify the translocation of mobile miRNAs between root and leaf in pumpkin seedlings. First, the unstressed (control) root and the unstressed stem are grafted (self-grafting) to detect possible miRNA differences that may occur due to tissue injury. In another set, the unstressed root (rootstock) was grafted with the stressed stem (scion) treated with Ni for 48 h. After grafting, the seedlings were placed in dark and humid conditions (>90%) for overnight. The PS, root, and leaf tissues were collected for RNA isolation. The protocols for RNA isolation, stem-loop cDNA synthesis, and stem-loop RT-PCR were carried out to determine the expression level of selected miRNAs.

## 3 Results

### 3.1 Contamination Test

RNA contamination from the neighboring tissues during the collection of phloem sap (PS) is one of the

challenges. *CmPP16*, a transcript specific to PS, was used as a positive control to elucidate possible RNA contamination. In addition, *RuBisCo*, a tissue-specific transcript that does not exist in the PS, was used as a negative control to test any possible RNA contamination during PS collection. Results showed that *RuBisCo* transcript was absent in the PS of the control and Ni-treated samples (24h and 48h) (Figure 1a). Conversely, the *CmPP16* transcript was evident in the PS specimens of the same seedlings (Figure 1a). Moreover, *RuBisCo* transcripts were detected in all tested leaves, including control, 24h, and 48h specimens (Figure 1b). These results showed that PS specimens collected from control and Ni-treated seedlings are exempt from RNA contamination that may be derived from neighboring tissues.

### 3.2 Stem-loop Quantitative RT-PCR Analysis of miRNAs

Expressions of 14 miRNAs in the PS of control, 24h, and 48h Ni-applied seedlings were determined. Among tested miRNAs, the abundance of five miRNAs (miR160, miR167, miR393, miR397, and miR398) was found to be altered at 24h and 48h of Ni treatment (Figure 2). Compared to the control, those miRNAs were down-regulated in Ni-treated seedlings.

### 3.3 Confirmation of Results with Semi-quantitative RT-PCR

To validate the RT-qPCR findings, a semi-quantitative RT-PCR technique was used to determine the expression level of five down-regulated miRNAs. As depicted in Figure 3, the intensity of miR167 and miR393 bands gradually decreased in 24h and 48h of Ni-treated samples compared to that of the control. These results aligned with the quantitative RT-qPCR results depicted in Figure 2. However, no significant change in band intensities was observed in miR160, miR397, and miR398 samples. These results confirm the existence and down-regulation of miR167 and miR393 in the phloem sap of pumpkin seedlings as responsive to nickel application.

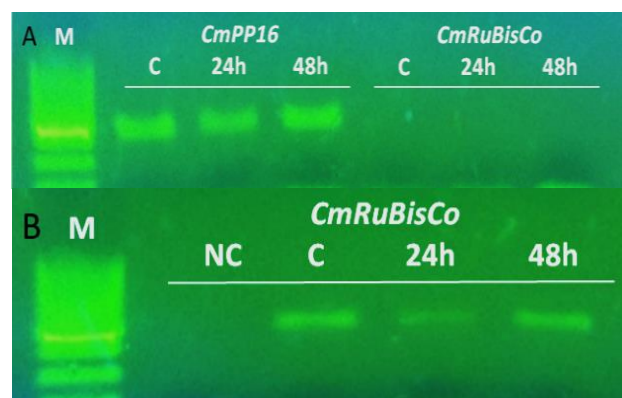


**Figure 1.** Agarose gel image showing contamination test results upon nickel (Ni) application. M = Marker (100 bp). (a) *CmPP16* transcripts were determined in the phloem sap of control (C), and Ni-treated seedlings (24h and 48h). However, *CmRuBisCo* transcripts were not detected in the identical specimens (b) The tissue-specific transcript, *CmRuBisCo*, was determined in the leaf tissues of control (C) and Ni-treated seedlings (24h and 48h). NC = negative (no template) control.

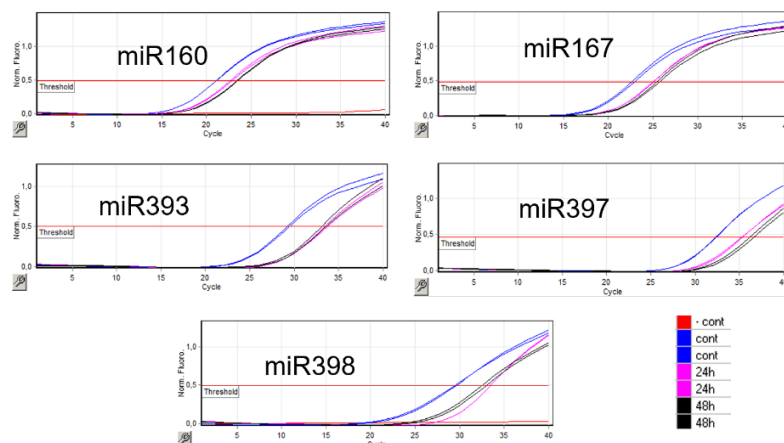


**Figure 2.** Stem-loop RT-qPCR analysis of miRNAs (miR160, miR167, miR393, miR397, and miR398) in the phloem sap (PS) of Ni-treated and untreated (control) seedlings. The color legend was shown on the right-hand side.

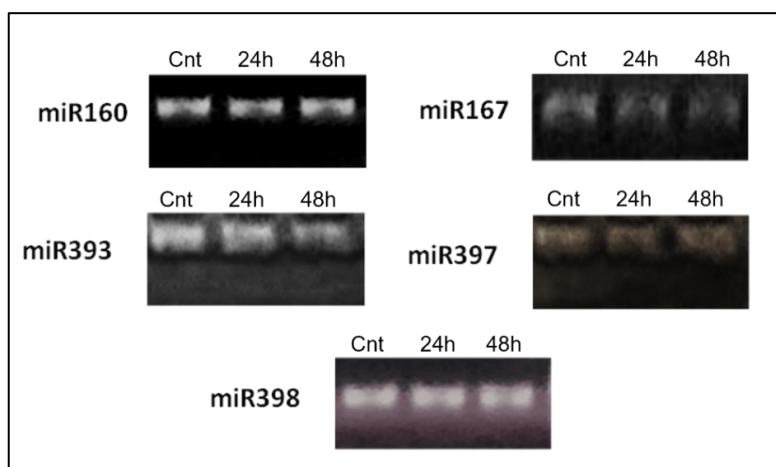


**Figure 3.** Semi-quantitative RT-PCR analysis of Ni-responsive miRNAs in control (Cnt) and Ni-treated (24h and 48h) plants.

### 3.4 Expression of miR167 and miR393 in Grafted Seedlings

Grafting experiments were carried out to verify the expression of Ni-responsive miRNAs found in the quantitative RT-qPCR and semi-quantitative RT-PCR analyses. For this purpose, the excess Ni-responsive miRNAs were determined in the PS of control (untreated), self-grafted (control rootstock + control scion), rootstock-grafted (control rootstock + Ni-treated scion), and scion-grafted (Ni-treated rootstock + control scion) seedlings (Figure 4a, b). Self-grafting was applied to elucidate a possible miRNA expression change that could be caused by tissue injury during the grafting process. Besides, Ni-treated scion was grafted on the control rootstock to determine the direction of miRNA movement (*i.e.*, from scion to rootstock or *vice versa*). Self-grafting results showed no difference in miR167 expression. However, the self-grafting process increased miR393 expression, which can be attributed to tissue injury/repair during the grafting (Figure 4c). This result revealed that miR393 could be responsive to tissue injury as well. Once Ni-treated scion is grafted on the control rootstock, the expression of miR167 and miR393 were suppressed, as expected. On the other hand, the grafting of Ni-treated rootstock with control scion increased the abundance of miR167 and miR393 compared to those of untreated (control) and self-grafting seedlings. These results show that miR167 and miR393 are Ni-responsive and move/travel from leaves to the roots.

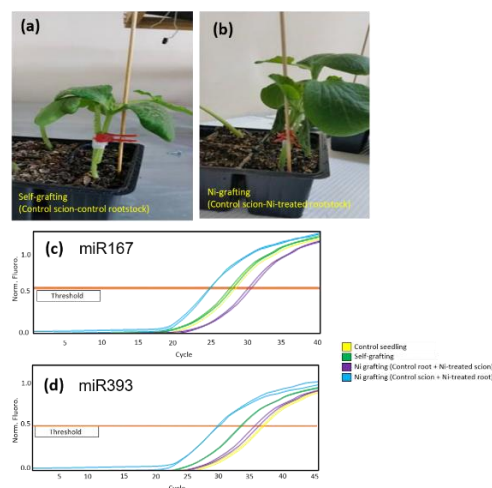


**Figure 4.** Grafting experiments. (a) The control seedlings were self-grafted. (b) The control scion has grafted on the Ni-treated (48h) rootstock—the stem-loop quantitative RT-PCR analysis of (c) miR167 and (d) miR393.

## 4 Discussion

Nickel (Ni) is an essential micronutrient for the growth and development of plants. It involves biochemical reactions and takes place in integral components of various biomolecules such as metalloenzymes and enzymes [32]. Besides, it is a heavy metal that limits crop growth and development and eventually yields when its concentration in the soil reaches an excess level [33]. Due to increasing

anthropogenic, technogenic, and geogenic activities, Ni pollution in agricultural soils has become widespread worldwide [34]. Burning fossil fuels, industries using Ni, and mining activities release it into the atmosphere. These releasing substances readily dissolve in water and then build up in the soil and sediments [35-38]. According to the World Health Organization (WHO), Ni concentration in soils is 15-30 mg/kg. Its concentration in most plant parts is between 0.05–10 mg/kg dry weight and is considered toxic above this amount [39]. Although plants' resistance mechanism and homeostasis against Ni stress have been studied [40-43], there is still a lack of information about Ni-induced miRNA mobilization. The information on this mechanism is crucial to understanding tissue or organ-level communication of plants to improve heavy metal resistance.

Small regulatory RNAs known as miRNAs are a diverse class that controls post-transcriptional gene expression. They also play a critical role in gene regulatory networks [44]. "Mobile" RNAs have been found in the phloem fluid/sap, which is functional in root-to-leaf communication [6, 45]. Moreover, they are known as naturally occurring species-to-species signaling molecules, such as between the parasitic plant *Cuscuta* and its hosts like *Arabidopsis* and tobacco [46]. Recent studies documented the first case of plant-to-plant miRNA communication. They provided experimental support for the idea that plants might uptake miRNAs produced by their neighbors, causing post-transcriptional gene silencing (PTGS) in the cells receiving them [47-48].

In this study, pumpkin seedlings were exposed to excess Ni, and stem-loop RT-PCR analysis was conducted for 14 miRNAs (miR156, miR168, miR398, miR166, miR397, miR167, miR164, miR169, miR390, miR172, miR393, miR159, and miR162), which were verified as PS residential. Among those miRNAs, miR160, miR167, miR393, miR397, and miR398 were responsive to Ni treatment, evidenced by stem-loop RT-qPCR (Figure 2). Besides, semi-quantitative RT-PCR analyses confirmed that those of two miRNAs (miR167 and miR393) are Ni-responsive (Figure 3), which were further tested by grafting experiments to find their transport direction (Figure 4). The grafting experiments revealed that miR167 and miR393 migrate from leaf to root. On the other hand, the abundance of other miRNAs (miR156, miR168, miR398, miR166, miR397, miR164, miR169, miR390, miR172, miR159, and miR162) in phloem sap did not change against Ni stress. Instead, they may play a role in systemic long-distance signaling during development or different types of stress.

miR398 is known to be a master regulator of plant development and stress responses [49]. A recent study found that miR398 is downregulated upon NiCl<sub>2</sub> treatments (50, 100, and 200  $\mu$ M) over control seedlings of castor bean (*R. communis L.*) [50]. The same study showed up-regulation of a miR398-target gene, *copper-zinc/superoxide dismutase (Cu-Zn/SOD or CSD)*, in both root and leaf tissues upon Ni treatments. Cu-Zn/SOD is an antioxidant protein involved in scavenging superoxide anions. Our findings indicate that miR398 is involved in the long-distance communication of pumpkin seedlings against Ni-stress. Reduced miR398 expression in the PS could release *Cu-Zn/SOD* transcripts in the target tissue.

Thus, the antioxidant defense system is promoted as an early stress response. In addition to miR398, miR171, miR395, miR396, and miR838 have been determined as Ni-responsive in the leaves of castor beans [50]. This study focused on identifying miRNAs in the PS of pumpkin. However, except for miR398, those miRNAs were not determined to be Ni-responsive. This can be attributed to the difference in plant type and the tissue studied, which is the PS of pumpkin in this study.

miR167 and miR393 were other Ni-responsive miRNAs found in the PS of pumpkin. Previous studies revealed their functions in different plants under nutrient deficiency. For instance, miR167 and miR160 were nitrate (N)-starvation responsive in *Arabidopsis* [51]. The potential functionality of miR160 in nitrogen (N) deficiency has been demonstrated in *Arabidopsis*. Its expression is upregulated in roots during transient low nitrate treatment [51]. In addition, several studies have revealed the functionality of miR167 in the developmental stages of tissues/organs (*i.e.*, root, leaf, flower, seed, embryo) and biotic and abiotic stress adaptation (reviewed by [52]). For instance, miR167 expression is induced in *Arabidopsis* under salinity, drought, and cold stresses [53-54]. Although miR167 is stress-responsive, its function against Ni-stress is yet to be identified. This study, for the first time, revealed its possible function during the regulation of Ni stress. In addition, the grafting experiments showed the direction of long-distance movement, which was from the leaf to the root.

Additionally, miR393 was found to be phloem-resided and responsive to Ni. The grafting studies revealed its leaf-to-root movement. The roots are the primary tissue exposed to Ni stress. In line with these findings, miR393 was found in the phloem sap of *Brassica napus* under nutrient deficiency [12]. Transgenic rice and *Arabidopsis* are more sensitive to salt stress when OsmiR393 is overexpressed [55]. This study verified miR167 and miR393 as responsive to excess Ni. Their leaf-to-root movement in the plant body through the phloem may regulate the Ni homeostasis in plants. The transcriptional regulation of these miRNAs in the target tissues (*i.e.*, roots or leaves) upon the miRNA translocation should be studied.

## 5 Conclusion

Several phloem-mobile miRNAs have been identified as messenger molecules, which play a molecular switch in target cells/organs and regulate early stress responses. For the first time, this study showed the phloem sap resident miRNAs in pumpkins and their response against excess nickel. Grafting experiments also showed the direction of miRNA movements. Among 14 selected miRNAs, miR167 and miR393 were nickel-responsive, moving from leaves to roots. Functional studies are necessary to clarify their role in the transcriptional regulation of nickel stress at their target tissue.

## Acknowledgments

The author states that the study does not require an ethics committee's approval. The author has no conflict of interest.

## Declaration

Ethics committee approval is not required.

## References

- [1] Kehr, J., & Buhtz, A. (2008). Long distance transport and movement of RNA through the phloem. *Journal of Experimental Botany*, 59, 85-92.
- [2] Kragler, F. (2010). RNA in the phloem: A crisis or a return on investment. *Plant Science*, 178, 99-104
- [3] Kehr, J. (2013). Systemic regulation of mineral homeostasis by micro RNAs. *Frontiers in Plant Science*, 4, 145.
- [4] Ruf, A., Oberkofler, L., Robatzke, S., & Weiberg, A. (2022). Spotlight on plant RNA-containing extracellular vesicles. *Current Opinion in Plant Biology*, 69, 102272.
- [5] Yoo, B. C., Kragler, F., Varkonyi-Gasic, E., Haywood, V., Evans, S. A., Lee, Y. M., Lough, T. J., & Lucas, W. J. (2004). A systemic small RNA signaling system in plants. *Plant Cell*, 16, 1979-2000.
- [6] Buhtz, A., Springer, F., Chappell, L., Baulcombe, D. C., & Kehr, J. (2008). Identification and characterization of small RNAs from the phloem of *Brassica napus*. *Plant Journal*, 53, 739-749.
- [7] Varkonyi-Gasic, E., Gould, N., Sandanayaka, M., Sutherland, P., & MacDiarmid, R. M. (2010). Characterisation of microRNAs from apple (*Malus domestica* 'Royal Gala') vascular tissue and phloem sap. *BMC Plant Biology*, 10, 159.
- [8] Tolstyko, E., Lezzhov, A., & Solovyev, A. (2019). Identification of miRNA precursors in the phloem of *Cucurbita maxima*. *PeerJ*, 7, e8269.
- [9] Kehr, J., & Kragler, F. (2018). Long distance RNA movement. *New Phytologist*, 218(1), 29-40.
- [10] Pant, B. D., Buhtz, A., Kehr, J., & Scheible, W. R. (2008). MicroRNA399 is a long-distance signal for the regulation of plant phosphate homeostasis. *Plant Journal*, 53, 731-738.
- [11] Lin, S. I., Chiang, S. F., Lin, W. Y., Chen, J. W., Tseng, C. Y., Wu, P. C., & Chiou, T. J. (2008). Regulatory network of microRNA399 and PHO<sub>2</sub> by systemic signaling. *Plant Physiology*, 147, 732-746.
- [12] Buhtz, A., Pieritz, J., Springer, F., & Kehr, J. (2010). Phloem small RNAs, nutrient stress responses, and systemic mobility. *BMC Plant Biology*, 10(64).
- [13] Pant, B. D., Musialak-Lange, M., Nuc, P., May, P., Buhtz, A., Kehr, J., ... & Scheible, W. R. (2009). Identification of nutrient-responsive Arabidopsis and rapeseed microRNAs by comprehensive real-time polymerase chain reaction profiling and small RNA sequencing. *Plant Physiology*, 150(3), 1541-1555.
- [14] Kuo, H. F., & Chiou, T. J. (2011). The role of microRNAs in phosphorus deficiency signaling. *Plant Physiology*, 156, 1016-1024.
- [15] Calderwood, A., Kopriva, S., & Morris, R. J. (2016). Transcript abundance explains mRNA mobility data in *Arabidopsis thaliana*. *Plant Cell*, 28, 610-615.
- [16] Yamasaki, H., Abdel-Ghany, S. E., Cohu, C. M., Kobayashi, Y., Shikanai, T., & Pilon, M. (2007). Regulation of copper homeostasis by micro-RNA in *Arabidopsis*. *Journal of Biological Chemistry*, 282(22), 16369-16378.
- [17] Ham, B. K., & Lucas, W. J. (2017). Phloem-mobile RNAs as systemic signaling agents. *Annual Review of Plant Biology*, 68, 173-195.
- [18] Fahlgren, N., Howell, M. D., Kascchau, K. D., Chapman, E. J., Sullivan, C. M., Cumbie, J. S., Givan, S. A., Law, T. F., Grant, S. R., Dangl, J. L., & Carrington, J. C. (2007). High-throughput sequencing of *Arabidopsis* microRNAs: Evidence for frequent birth and death of MIRNA genes. *PLoS ONE*, 2.
- [19] Martin, A., Adam, H., Diaz-Mendoza, M., Zurczak, M., Gonzalez-Schain, N. D., & Suarez-Lopez, P. (2009). Graft-transmissible induction of potato tuberization by the microRNA miR172. *Development*, 136, 2873-2881.
- [20] Kasai, A., Kanehira, A., & Harada, T. (2010). miR172 can move long distance in *Nicotiana benthamiana*. *The Open Plant Science Journal*, 4, 1-6.
- [21] Alfano, M., & Cavazza, C. (2020). Structure, function, and biosynthesis of nickel-dependent enzymes. *Protein Science*, 29(5), 1071-1089.
- [22] Iyaka, Y. A. (2011). Nickel in soils: A review of its distribution and impacts. *Scientific Research and Essays*, 6(33), 6774-6777.
- [23] El-Naggar, A., Ahmed, N., Mosa, A., Niazi, N. K., Yousaf, B., Sharma, A., ... & Chang, S. X. (2021). Nickel in soil and water: Sources, biogeochemistry, and remediation using biochar. *Journal of Hazardous Materials*, 419, 126421.
- [24] Kacar, B., Katkat, V., & Öztürk, Ş. (2009). *Bitki Fizyolojisi (3. Baskı)*. Nobel Yayınları No: 848.
- [25] Zengin, F. K., & Munzuroglu, O. (2005). Effects of some heavy metals on content of chlorophyll, proline and some antioxidant chemicals in bean (*Phaseolus vulgaris* L.) seedlings. *Acta Biologica Cracoviensia Series Botanica*, 47(2), 157-164.
- [26] Tombuloglu, G., Tombuloglu, H., Sakcali, M. S., & Unver, T. (2015). High-throughput transcriptome analysis of barley (*Hordeum vulgare*) exposed to excessive boron. *Gene*, 557(1), 71-81.
- [27] Chomczynski, P., & Sacchi, N. (1987). Single-step method of RNA isolation by acid guanidinium thiocyanate-phenol-chloroform extraction. *Analytical Biochemistry*, 162, 156-159.
- [28] Varkonyi-Gasic, E., Wu, R., Wood, M., Walton, E. F., & Hellens, R. P. (2007). Protocol: A highly sensitive RT-PCR method for detection and quantification of microRNAs. *Plant Methods*, 3, 12.
- [29] Yanik, H., Turktas, M., Dundar, E., Hernandez, P., Dorado, G., & Unver, T. (2013). Genome-wide identification of alternate bearing-associated microRNAs (miRNAs) in olive (*Olea europaea* L.). *BMC Plant Biology*, 13, 10-31.
- [30] Ruiz-Medrano, R., Xocosnostle-Cazares, B., & Lucas, W. J. (1999). Phloem long-distance transport of CmNACP mRNA: implications for supracellular regulation in plants. *Development*, 126, 4405-4419.
- [31] Zhang, S., Sun, L., & Karger, F. (2009). The phloem-delivered RNA pool contains small noncoding RNAs and interferes with translation. *Plant Physiology*, 150(1), 378-387.
- [32] Saleh, S. R., Kandeel, M. M., Ghareeb, D., Ghoneim, T. M., Talha, N. I., Alaoui-Sossé, B., & Abdel-Daim, M. M. (2020). Wheat biological responses to stress caused by cadmium, nickel and lead. *Science of The Total Environment*, 706, 136013.
- [33] Bhalerao, S. A., Sharma, A. S., & Poojari, A. C. (2015). Toxicity of nickel in plants. *International Journal of Pure and Applied Bioscience*, 3(2), 345-355.
- [34] Rizwan, M., Imtiaz, M., Dai, Z., Mehmood, S., Adeel, M., Liu, J., & Tu, S. (2017). Nickel stressed responses of rice in Ni subcellular distribution, antioxidant production, and osmolyte accumulation. *Environmental Science and Pollution Research*, 24(20), 20587-20598.
- [35] Mousavi, H. Z., & Seyedi, S. R. (2011). Nettle ash as a low cost adsorbent for the removal of nickel and cadmium from wastewater. *International Journal of Environmental Science & Technology*, 8(1), 195-202.
- [36] Harasim, P., & Filipek, T. (2015). Nickel in the environment. *Journal of Elementology*, 20(2).

- [37] Shahbaz, A. K., Iqbal, M., Jabbar, A., Hussain, S., & Ibrahim, M. (2018). Assessment of nickel bioavailability through chemical extractants and red clover (*Trifolium pratense* L.) in an amended soil: Related changes in various parameters of red clover. *Ecotoxicology and Environmental Safety*, 149, 116-127.
- [38] AlMisned, G., Al-Abdullah, T., Liadi, F. A., & Hawsawi, A. (2022). Comparison between NIS and TNC channels for the detection of nickel in soil samples. *Applied Radiation and Isotopes*, 186, 110303.
- [39] Kozlov, M. V. (2005). Sources of variation in concentrations of nickel and copper in mountain birch foliage near a nickel-copper smelter at Monchegorsk, north-western Russia: results of long-term monitoring. *Environmental Pollution*, 135(1), 91-99.
- [40] He, S., He, Z., Yang, X., & Baligar, V. C. (2012). Mechanisms of nickel uptake and hyperaccumulation by plants and implications for soil remediation. *Advances in Agronomy*, 117, 117-189.
- [41] Theriault, G., Michael, P., & Nkongolo, K. (2016). Comprehensive transcriptome analysis of response to nickel stress in white birch (*Betula papyrifera*). *PLOS ONE*, 11(4).
- Hassan, M. U., Chattha, M. U., Khan, I., Chattha, M. B., Aamer, M., Nawaz, M., & Khan, T. A. (2019). Nickel toxicity in plants: reasons, toxic effects, tolerance mechanisms, and remediation possibilities—a review. *Environmental Science and Pollution Research*, 26(12), 12673-12688.
- [42] Warren, A., Michael, P., & Nkongolo, K. (2022). Nickel translocation, toxicity, and its effect on the expression of genes associated with nickel resistance in red pine (*Pinus resinosa*). *Ecological Genetics and Genomics*, 25, 100148.
- [43] Tombuloglu, G. (2022). Drought-responsive miRNAs in plants: A review. *International Journal of Innovative Engineering Applications*, 6(1), 150-157.
- [44] Loreti, E., & Perata, P. (2022). Mobile plant microRNAs allow communication within and between organisms. *New Phytologist*, 235(6), 2176-2182.
- [45] Shahid, S., Kim, G., Johnson, N. R., Wafula, E., Wang, F., Coruh, C., Bernal-Galeano, V., Phifer, T., Depamphilis, C. W., & Westwood, J. H. (2018). MicroRNAs from the parasitic plant *Cuscuta campestris* target host messenger RNAs. *Nature*, 553(7686), 82-85.
- [46] Betti, F., Ladera-Carmona, M. J., Weits, D. A., Ferri, G., Iacopino, S., Novi, G., Svezia, B., Kunkowska, A. B., Santaniello, A., & Piaggese, A. (2021). Exogenous miRNAs induce post-transcriptional gene silencing in plants. *Nature Plants*, 7(12), 1379-1388.
- [47] Marzec, M. (2022). MicroRNA: a new signal in plant-to-plant communication. *Trends in Plant Science*, 27(5), 418-419.
- [48] Li, J., Song, Q., Zuo, Z. F., & Liu, L. (2022). MicroRNA398: A master regulator of plant development and stress responses. *International Journal of Molecular Sciences*, 23(18), 10803.
- [49] Çelik, Ö., & Akdaş, E. Y. (2019). Tissue-specific transcriptional regulation of seven heavy metal stress-responsive miRNAs and their putative targets in nickel indicator castor bean (*R. communis* L.) plants. *Ecotoxicology and Environmental Safety*, 170, 682-690.
- [50] Gifford, M. L., Dean, A., Gutierrez, R. A., Coruzzi, G. M., & Birnbaum, K. D. (2008). Cell-specific nitrogen responses mediate developmental plasticity. *Proceedings of the National Academy of Sciences*, 105(2), 803-808.
- [51] Liu, X., Huang, S., & Xie, H. (2021). Advances in the regulation of plant development and stress response by miR167. *Frontiers in Bioscience-Landmark*, 26(9), 655-665.
- [52] Liu, H. H., Tian, X., Li, Y. J., Wu, C. A., & Zheng, C. C. (2008). Microarray-based analysis of stress-regulated microRNAs in *Arabidopsis thaliana*. *RNA*, 14(5), 836-843.
- [53] Wang, L. L., Zhao, T. L., Ge, J. T., et al. (2017). Application prospects of miRNAs in response to plant cold stress in the research of plant cold resistance. *Shanghai Journal of Agricultural Sciences*, 33(2), 129-134.
- [54] Gao, P., Bai, X., Yang, L., Lv, D., Pan, X., Li, Y., Cai, H., Ji, W., Chen, Q., & Zhu, Y. (2011). Osa-MIR393: A salinity- and alkaline stress-related microRNA gene. *Molecular Biology Reports*, 38(4), 237-242.